Atomic Layer Deposited Thin Films for Dielectrics, Semiconductor Passivation, and Solid Oxide Fuel Cells

BY

Runshen Xu
Bachelor of Science, Dalian University of Technology, Dalian, China, 2008

THESIS

Submitted as partial fulfillment of the requirements
for the degree of Doctor of Philosophy in Chemical Engineering
in the Graduate College of the
University of Illinois at Chicago, 2013

Chicago, Illinois

Defense Committee:

Christos Takoudis, Chair and Advisor
Gregory Jursich, Department of Bioengineering
Robert Klie, Department of Physics
Alan Feinerman, Department of Electrical and Computer Engineering
Ke-Bin Low, UIC Research Resources Center

ACKNOWLEDGEMENTS

First and foremost, I would like to express my sincere gratitude to my advisor, Prof. Christos Takoudis, for accepting me as his PhD student, for offering me his insightful suggestions and contributions in my PhD research and for having faith in me during the times when I was struggling. I would also like to thank my committee members, Dr. Robert Klie, Dr. Alan Feinerman, Dr. Gregory Jursich and Dr. Kebin Low for taking time out of their busy schedules to serve on my graduate committee.

I am grateful to Dr. Gregory Jursich for his helpful discussions and support while working on the ALD project. I am also thankful to Dr. Robert Klie, Dr. Gregory Jursich, Dr. Alan Feinerman, Dr. Jeffery Miller, and Dr. Alan Zdunek for their insightful suggestions within the solid oxide fuel cell project.

I want to sincerely thank Dr. Kebin Low for the XPS training at the Research Resource Center, UIC East campus; Dr. Mauro Sardelar for the GIXRD trainings at the Frederick Seitz Materials Research Laboratory, Urbana; Dr. Se-Young An for the trainings at the Nanotechnology Core Facility at UIC East campus.

Especially thanks to Dr. Alan Feinerman from Electrical and Computer Engineering department of UIC for assisting me with the resistivity measurement; Dr. Robert Klie from Physics department of UIC for assisting me with the TEM studies; Dr. Honghui Zhou from the Frederick Seitz Materials Research Laboratory for assisting me with the SEM analyses and; Dr. Bart Gordon from Materials Development Corporation for helping the C-V/I-V measurement.

I would like to thank to Dr. Christian Dussarrat and Dr. Katamreddy Rajesh (also a group alumnus) from Air Liquide for providing Hafnium, Titanium, Erbium, and Zirconium precursors. Also, I would like to thank to Dr. Sid Ghosh and Mr. Jun Huang, from the Department of Electrical and Computer Engineering at UIC for providing GaSb and InAs/GaSb substrates. The financial support from the National Science Foundation (NSF GOALI 0329195, EEC 1062943 and CBET 1067424) and the University of Illinois at Chicago is gratefully acknowledged.

Last but not the least, I would like to thank my group alumni Dr. Manish Singh and Dr. Qian Tao for their patience and technical help when I was at a research plateau, and all AMReL lab members for their help and support during my PhD course of studies. Most grateful thanks to my parents and other family members for their encouragement and unconditional support.

TABLE OF CONTENTS

TABLE OF CONTENTS (Continued)

LIST OF TABLES

LIST OF FIGURES

FIGURE PAGE

LIST OF FIGURES (Continued)

FIGURE PAGE

LIST OF FIGURES (Continued)

FIGURE PAGE

SUMMARY

Atomic layer deposition (ALD) utilizes sequential precursor gas pulses to deposit one monolayer or sub-monolayer of material per cycle based on its self-limiting surface reaction, which offers advantages, such as precise thickness control, thickness uniformity, and conformality. ALD is a powerful means of fabricating nanoscale features in future nanoelectronics, such as contemporary sub-45 nm metal-oxide-semiconductor field effect transistors, photovoltaic cells, near- and far-infrared detectors, and intermediate temperature solid oxide fuel cells.

High dielectric constant, κ, materials have been recognized to be promising candidates to replace traditional SiO_2 and SiON, because they enable good scalability of sub-45 nm MOSFET (metal-oxide-semiconductor field-effect transistor) without inducing additional power consumption and heat dissipation. In addition to high dielectric constant, high-κ materials must meet a number of other requirements, such as low leakage current, high mobility, good thermal and structure stability with Si to withstand high-temperature source-drain activation annealing. In this thesis, atomic layer deposited Er_2O_3 doped TiO_2 is studied and proposed as a thermally stable amorphous high-κ dielectric on Si substrate. The stabilization of TiO_2 in its amorphous state is found to achieve a high permittivity of 36, a hysteresis voltage of less than 10 mV, and a low leakage current density of 10^{-8} A/cm^2 at −1 MV/cm.

In III-V semiconductors, issues including unsatisfied dangling bonds and native oxides often result in inferior surface quality that yields non-negligible leakage currents and degrades the long-term performance of devices. The traditional means for passivating

the surface of III-V semiconductors are based on the use of sulfide solutions; however, that only offers good protection against oxidation for a short-term (i.e., one day). In this work, in order to improve the chemical passivation efficacy of III-V semiconductors, ultra-thin layer of encapsulating ZnS is coated on the surface of GaSb and GaSb/InAs substrates. The 2 nm-thick ZnS film is found to provide a long-term protection against reoxidation for one order and a half longer times than prior reported passivation likely due to its amorphous structure without pinholes.

Finally, a combination of binary ALD processes is developed and demonstrated for the growth of yttria-stabilized zirconia films using alkylamido-cyclopentadiengyls zirconium and tris(isopropyl-cyclopentadienyl)yttrium, as zirconium and yttrium precursors, respectively, with ozone being the oxidant. The desired cubic structure of YSZ films is apparently achieved after post-deposition annealing. Further, platinum is atomic layer deposited as electrode on YSZ (8 mol% of Yttria) within the same system. In order to control the morphology of as-deposited Pt thin structure, the nucleation behavior of Pt on amorphous and cubic YSZ is investigated. Three different morphologies of Pt are observed, including nanoparticle, porous and dense films, which are found to depend on the ALD cycle number and the structure and morphology of they underlying ALD YSZ films.

1. INTRODUCTION

1.1. Transistor History and Current Challenges

The transistor is one of the most fundamental electronic devices, acting as a switch or amplifier in almost all modern circuits for the control of electronic signals and electrical power. The first patent of transistor principle was filed by physicist Lilienfeld in 1926, describing features, construction, and operation of transistor [1, 2]. In the patent named, method and apparatus for controlling electronic current, Lilienfeld proposed a device, like modern field-effect transistor, to control the current between two terminals of a solid material by establishing a third potential [1]. However, Lilienfeld did not have any research paper published, and there is no evidence, if any of the devices proposed by him was built and worked [2].

More than 20 years later, the first point-contact transistor made use of high-purity germanium was invented at Bell Telephone Laboratories on December 16, 1947 by physicists William Shockley, John Bardeen, and Walter Brattain [2, 3]. This point-contact transistor was applied for a patent by John Bardeen and Walter Brattain and announced to public in June 1948 [4]. Compared with traditional vacuum tubes, the transistor offer many favorable advantages, such as small dimension, long lifespan, and no filament required [2]. The invention of transistor thereby not only propelled the electronics age forward, but also sparked an extensive interest in solid-state research. However, for the point-contact transistor, the metal wires were directly embedded in the semiconductor, which was difficult to manufacture and degraded the reliability. By

continuously paving the way for developing transistors, Dacey and Ross successfully built the first junction field-effect transistor in 1953 [5], which effectively improve the performance of transistors and feasibility for manufacturing.

Based on the invention and minimization of integrated circuit by Jack Kilby and Texas Instruments in 1950's [6], the small scale integration, up to 20 transistors per chip, was developed in 1960's [7]. Increasing the transistor density and count on integrated circuit then had been recognized an effective method to delivery better performance. In 1965, Gordon Moore described a long-term trend for the development of computing hardware in his paper [7]. Moore's law predicted a regular periodic doubling of transistor counts in an integrated circuit from the invention of the integrated circuit in 1958 until 1965, and Moore claimed that this trend would continue for at least ten years [7]. A reality means of extending Moore's law is continuously shrinking the feature size of transistors that populated the integrated circuit. According to Moore's law, transistor dimension was scaled by 30% every two years [8]. The classic scaling law of field-effect transistor was described in 1974 [9], and the very large scale integration, over 5000 transistors per chip, had been implemented in 1970s [10]. As seen in Fig. 1, Moore's law has been now proven to be accurate [10]. In addition, it is now widely used in industry to guide long-term planning and to act as the roadmap for the research and development of transistors. In 2011, the computer chip consisted of 2.6 billion transistors has been achieved by scaling the dimension of each transistor to 32 nm.

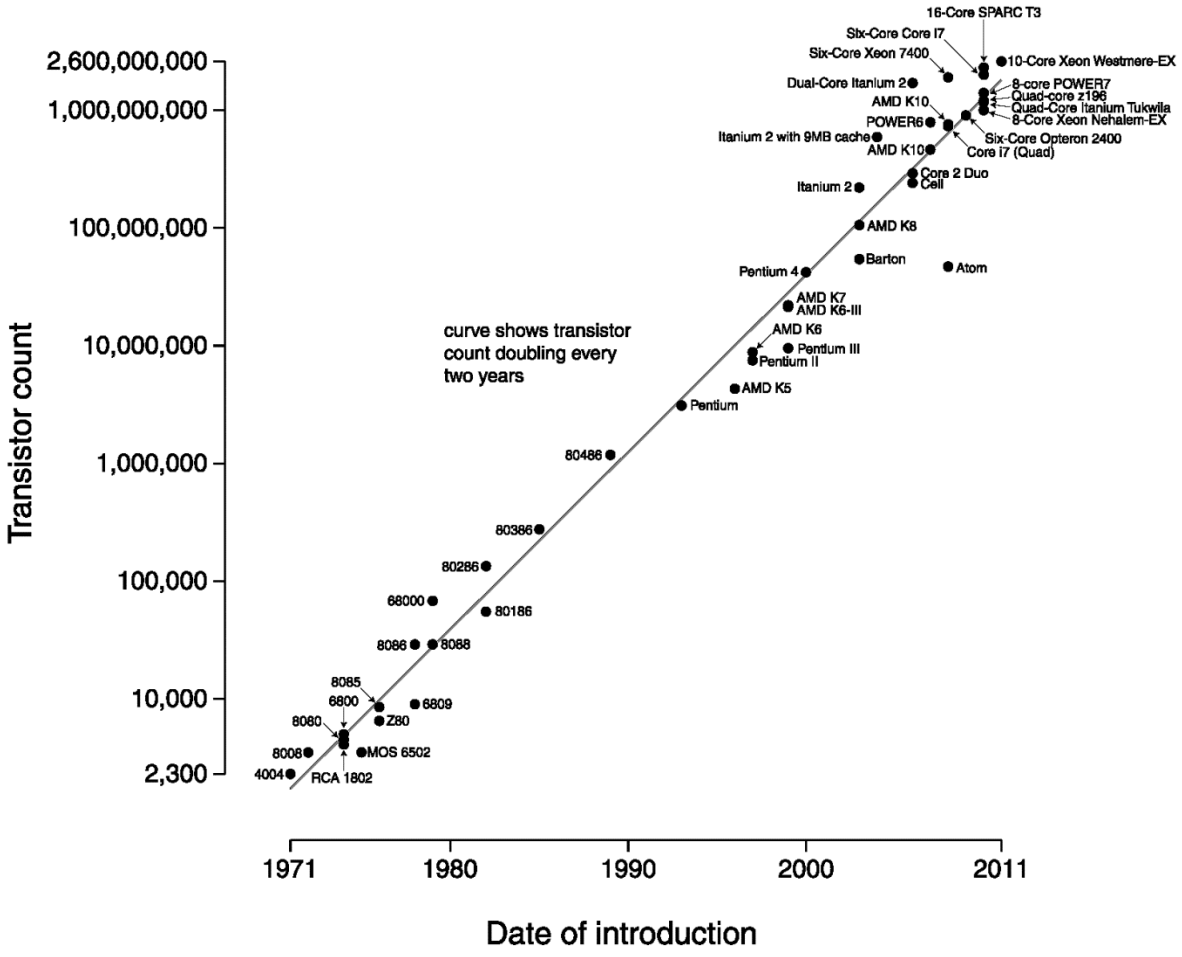

Figure 1. The transistor count per chip as a function of time [10]

Today, the most used transistors are metal-oxide-semiconductor field-effect transistors, in which a weak electrical signal applied on the gate electrode generates electrical field passing through the gate oxide to control the current of semiconductor between source and drain [2]. The dimension of Si-based MOSFET has been continuously shrinking for almost 40 years, since the classical scaling was described in 1974. According to the demanding scaling requirements for gate stacks, there are mainly two eras for feature size scaling of conventional MOSFET: SiO_2 era based on classic scaling and high-κ materials era based on innovations [11]. The traditional dielectric material, SiO_2, has been widely used for many decades. SiO_2 dielectric offers several advantages, including easy being grown, well known growth rate function, good compatibility with Si, and low interfacial state density when fabricated on Si. However, continued gate length scaling of MOSFETs requires simultaneous scaling of its geometrical parameters, especially SiO_2 insulator thickness [11, 12]. The fundamental thickness limitation for SiO_2 dielectric of less than 2 nm has been reached, resulting in a very high tunneling leakage current, exceeding 1 A/cm^2 at 1 V [13]. The leakage issue of SiO_2 was apparent since the late 1990's, and the power dissipation and inefficiency of the integrated circuit will rise to an unacceptable value, even for high power applications [13]. Therefore, the SiO_2 era ended in the early 2000's.

It has been known that the tunneling leakage current can be exponentially decreased by increasing the thickness of insulator [12]. Also, the capacitance of a planar complimentary MOS capacitor could be determined by using the equation:

$$C = \frac{\varepsilon_0 kA}{t}$$

, where ε_0 is the permittivity of free space, κ is the relative dielectric constant, A is the area and t is the thickness of insulator. To maintain the same capacitance as SiO_2, high-κ materials could have a thicker physical thickness, which would be able to significantly reduce the leakage current. Also, high-κ materials could be evaluated with an equivalent SiO_2 thickness calculated by the equation:

$$\mathrm{EOT} = \frac{3.9 \times t_{\mathrm{high-k}}}{\kappa}$$

, where $t_{high\text{-}k}$ is referred to the thickness of high-κ materials. For example, the high-κ material with a dielectric constant of 16 and a thickness of 4 nm would have an EOT of ~1 nm, which enables a further scalability by reducing leakage current. Therefore, high-κ materials are introduced to replace traditional SiO_2 and to break through the scaling barrier. In addition to high dielectric constant, high-κ materials must meets a great number of other necessary requirements, such as large conduction-band offset to Si, low leakage current, high mobility, low interfacial state density, and good structural and thermal stability with Si to withstand high-temperature source drain activation annealing [13].

In 2007, Intel has announced the first working 45-nm microprocessors built with the revolutionary high-κ dielectric plus metal gate transistors, and the high-κ technology was delivered in their 2007 processor series named Penryn [14]. As the performance and scalability of high-κ dielectric-based transistors could be further improved, extensive effort is currently devoted to the solid-state investigation of various high-κ materials, their related fabrication techniques and processing technology [12].

1.2. Challenges of III-V Semiconductor-based Devices and Passivation Technologies

III-V group semiconductors are important materials in a wide range of electronic devices, such as high speed electronics [15, 16], photovoltaic cells [17-19], and near- and far-infrared optoelectronic devices [20]. In particular, III-V group semiconductor is important for enabling mid- and long-wavelength infrared detectors in terms of their moderate band gap (for example, 0.72 eV for GaSb) and intrinsic carrier concentration [20, 21]. As the dimension of semiconductor devices has been continuously shrinking in recent years, the surface and interface region of semiconductors has been widely considered to be one of the most important components affecting the device performance [22].

An ideal surface or interface is defined as a sharp barrier, delimiting clearly the interior regions or the outer boundaries of materials. However, most of III-V group semiconductor surfaces often yield unsatisfied dangling bonds and native oxides, which result in inferior surface quality, inducing non-negligible leakage currents, high density of surface states, and serious degradation of long-term performance of III-V group semiconductor-based devices [23-25]. To eliminate the undesirable issues and improve the surface quality, surface passivation has been extensively investigated.

The semiconductor passivation is typically carried out on the outside of a semiconductor and it could be classified into two groups [22]. The first group is the chemical passivation which prevents a semiconductor from reacting with the atmosphere gas, for example, the oxidation of semiconductor surface by air. The second group is the

electrical passivation by eliminating the interfacial states from the band gap at surface or interface regions. In addition, the passivation method must provide an adequate barrier to avoid the loss of semiconductor electrons in the passivation layer [22]. Therefore, the passivation process must provide a chemically inert surface and effectively reduce the active recombination centers and charge trapped sites on the surface.

Among the surface passivation technologies, sulfide passivation, based on the surface modification with sulfur or selenium atoms, has been identified as one of the most effective passivation routes for III-V group semiconductors (e.g., GaSb or InAs), because it enables both chemical and electronic surface passivation on the surfaces. The sulfide passivation could form an encapsulating layer, as a result, restricting the oxidation of a semiconductor surface by atmospheric air, while simultaneously decreasing the interfacial state density and the surface recombination velocity. The development of sulfide passivation started in the mid-1980s [22]. So far, tremendous research efforts have been devoted to the passivation route, passivation mechanism, and interaction between semiconductor surfaces and sulfides applied [26, 27]. The passivation is generally carried out with three different methods [22]. The first route is treated the semiconductor surface with aqueous solutions using inorganic or organic sulfides, such as sodium sulfide and ammonium sulfide [26]. The second route is based on the interaction of semiconductor surface with sulfide atoms adsorbed from the gas phase, such as hydrogen sulfide gas [28]. The electrochemical deposition of sulfides on semiconductor surface is the third passivation route, which was first used to passivate InSb for metal-insulator-semiconductor application in 1991 [29]. The electrochemical deposition method for

passivation often offers a relatively thick encapsulating film to effectively insulate the semiconductor surface from atmosphere and, as a result, to reduce the formation of undesired native oxides on the surface. With the demanding needs of future electronics made of III-V group semiconductors, the investigation of surface passivation technology is of importance to improve the long-term performance and efficiency of passivation-treated devices [26]. By producing thin film with high uniformity and conformity, atomic layer deposition is now an emerging means of passivating III-V group semiconductor, especially with three-dimensional features.

1.3. Solid Oxide Fuel Cells and Current Challenges

Solid oxide fuel cell, as a clean and renewable energy source, is a promising next-generation energy conversion device, in which chemical energy is directly converted to electrical energy by utilizing fuel and oxidant gases at a required temperature [30].

SOFCs meet the demanding requirements for future energy conversion devices, including scalable feature size, high efficiency, good compatibility with a wide range of fuels, and low sensitivity to impurities in the fuel. Gas, such as hydrogen, natural gas, alcohols, or diesel, could be applied as fuel in a SOFC for converting energy with an expected efficiency up to 85%, which can be achieved by diverse systems, such as gas turbine hybridization [ref$].

Figure 2 shows the scheme of the classical planar solid oxide fuel cell. Similar to other kind of fuel cell, the SOFC generally consists of two electrodes sandwiched around

an electrolyte. Fuel gas is applied on the anode side of SOFC while oxidant simultaneously entering through the cathode side. Both cathode and anode should have a high electrical conductivity and need to be porous to allow fuel and oxidant gases to penetrate through. The electrolyte must be dense and conductive to ions rather than electrons or gas, as a result, to reduce the leakage current and to prevent the reaction between fuel and oxidant in gas phase [30]. The reactions taking place on anode and cathode sides of SOFC operated with H_2 and O_2 are, respectively, shown in the following equations.

$$H_2 + O^{2-} \rightarrow H_2O + 2e^-$$

$$O_2 + 4e^- \rightarrow 2O^{2-}$$

The operation of SOFCs, up to present technology, generally requires a very high temperature in the range of 800-1000 ℃, to permit the transport of O^{2-} from air reducing cathode to the fuel oxidizing anode due to the low ion conductivity of electrolyte at lower temperatures [31]. The low ion conductivity of traditional SOFCs is related to the mass production techniques being used for producing electrolyte or electrode with thickness of a few tens of microns, which also might induce high ohmic losses. However, the necessary high operating temperature degrades the cost efficiency of SOFCs for application required low temperatures. Recently, tremendous efforts have been devoted to developing of intermediate temperature SOFCs, in which a desired efficiency of converting energy is expected to be achieved at temperatures at least lower than 800 ℃ [30, 32].

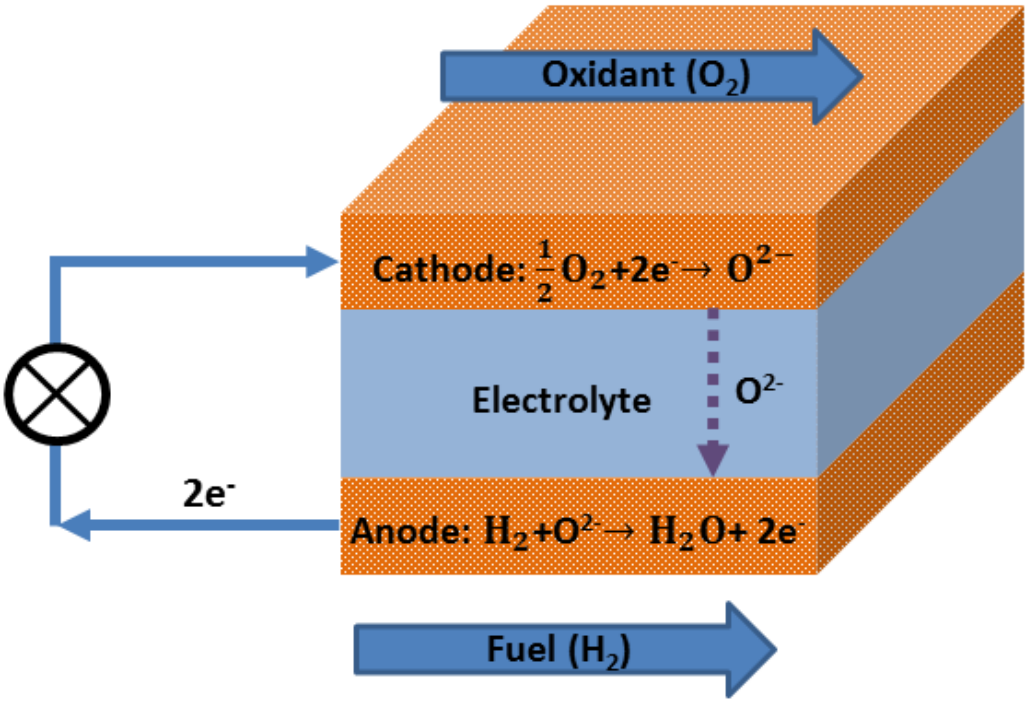

Figure 2. A typical scheme of a planar SOFC cell

With the development of thin film fabrication technologies, atomic layer deposition has been currently considered to be a powerful means of fabricating very thin structures for ITSOFCs [31]. The thin film of electrolyte, in nanometer scale, is capable to enhance the oxygen ion transport at intermediate temperatures, which could considerably slow down the thermal stress-induced aging process of materials used. Therefore, improving the construction of ITSOFCs utilizing ALD would be an effective solution to overcome the challenge for lowering the operating temperature without sacrificing energy conversion efficiency, and to empower the optimized ITSOFCs for more applications.

1.4. Overview of the Thesis

In this thesis, several atomic layer deposited materials, including oxide, sulfide, and metal, will be discussed, with attention focused on the applications of high-κ technology and chemical passivation of III-V group semiconductor as well as ITSOFCs. Chapter 2 reviews the background information for several classic thin-film deposition techniques and the recent research on novel titanium-based high-κ materials, III-V semiconductor passivation technology, and thin structures of ITSOFCs fabricated with ALD. Chapter 3 describes, in details, deposition and processing systems, experimental procedures, and characterization techniques used in this work. Chapter 4.1 presents the deposition and key properties of high-κ Er_2O_3 film made use of tris(methylcyclopentadienyl)erbium as metal precursor and ozone as oxidant by ALD process. Chapter 4.2 is an extension of Chapter 4.1, focusing on the development of amorphous high-κ material through doping ALD TiO_2 with Er_2O_3 for MOS structures in

Si integrated circuit technology, and the stabilization of TiO_2 in its amorphous state combined with required thermal process is found to achieve a high permittivity (i.e., 36) without sacrificing its leakage current characteristics and reliability. Apart from high-κ technology, chapter 4.3 demonstrates a novel ALD route for passivation of III-V semiconductors of GaSb and InAs using ultra-thin atomic layer deposited ZnS, which is found to provide a long-term protection against reoxidation for about 14 days due to its amorphous structure without any pinhole. In addition to high-κ material and semiconductor passivation, YSZ and Pt as electrolyte and electrode for SOFCs are atomic layer deposited and studied. Chapter 4.4 presents the potential for introducing novel tris(isopropyl-cyclopentadienyl)yttrium as a suitable ALD precursor and Ar^+ beam as an effective means of removing surface $Y(OH)_3$ on Y_2O_3 films. In chapter 4.5, a combination of binary ALD processes is developed and demonstrated for the growth of YSZ films using alkylamido-cyclopentadiengyls zirconium and tris(isopropyl-cyclopentadienyl)yttrium, as zirconium and yttrium precursors, respectively, with ozone as the oxidant. The desired cubic structure of YSZ films is achieved after post-deposition annealing. Chapter 4.6 presents the nucleation behavior and morphology control of ALD Pt on YSZ surfaces, and the property of YSZ substrates is found to be an important factor in determining Pt nucleation.

2. LITERATURE REVIEW

2.1. Thin Film Deposition Techniques

Thin film deposition techniques have been used in almost all modern electronic devices, and it is well known that the structure and property of fabricated thin films are strongly dependent on deposition routes [33, 34]. Thus, it is of importance to understand the principle and specific characteristics of different deposition techniques for matching the demanding requirements of various applications.

According to the mechanism of thin film fabrication, deposition techniques have been generally classified into two groups, physical vapor deposition and chemical reaction deposition [33]. Physical vapor deposition covers a number of deposition techniques, in which materials are released from a source utilizing physical method (e.g., high temperature or bombardment) and then transfer to the substrate. In chemical reaction deposition techniques, the formation of thin film is generally based on both delivery and reaction of reactants. In this session, a general introduction of several classic deposition techniques, including sputtering, electron beam evaporation, chemical vapor deposition, and atomic layer deposition, will be given for understanding the characteristics of different techniques.

Sputtering deposition is a process in which atoms are released from a solid material source, named target, by striking the target material with high kinetic energy ions, typically Ar^+ [34-36]. During operation, the target and substrate are used as cathode

and anode, respectively. Gaseous ion particles are accelerated toward target material by an imposed electrical field. The chamber pressure must be maintained at ~10^{-1} torr to achieve an effective discharge of sputtering gas (e.g., Ar) while avoiding the highly scattering with neutral atoms released from the target in the gas phase. The concentration of ions and electrons in sputtering system is determined with the DC power, because the secondary electrons are generated when the ions strike the target. To achieve efficient momentum transfer in the collision process, the atomic weight of the sputtering gas must be close to that of the target. Therefore, gaseous Ne is preferable for bombarding light elements, while Kr and Xe are more desired for bombarding heavy elements. Sputtering technologies are, in details, classified into 4 types, including DC sputtering, radio frequency sputtering, magnetron sputtering, and bias sputtering. Compare with other physical vapor deposition technique, such as evaporation, sputtering deposition generally offers a better control of stoichiometry and thickness uniformity, and are capable to deposit both crystalline and amorphous materials [33]. However, sputtered films are easier to be contaminated by sputtering gas, which restricts the use of sputtering deposition for epitaxial growth.

Electron beam evaporation is one of the most used physical vapor deposition techniques, in which a target anode is bombarded using an electron beam emitted from a tungsten thermal electron emission filament in vacuum environment (typically 10^{-6} torr) [34]. The kinetic energy of electron beam is transfer to thermal energy on the target surface, sharply raising the temperature of the surface and, as a result, causing a relatively high vapor pressure of the target material for deposition. Electron beam evaporation

could be used to deposit a variety of materials, such as oxide or metal. This deposition route generally yields a relatively high deposition rate in the range of 0.01–410 nm/s at low substrate temperature [36]. Electron beam evaporation often deposits thin films with high purity; however, the stoichiometry of inorganic compounds fabricated might be different from the source material due to the possible change of compound composition at high temperature in vapor phase [33]. In addition, the interaction of high-temperature vapor and substrate should be considered in this deposition process, which might result in interdiffusion in surface region of substrate. More technical details will be given in chapter 3.1.2.

Chemical vapor deposition is a deposition technique for solid films by utilizing surface reactions between a volatile inorganic or organic compound, named precursor, and other suitable reactant gas [37]. CVD has been extensively used for deposition of a variety of materials, such as oxides, metals, sulfides, nitrides and semiconductors with crystalline and/or amorphous structure [35]. The feasibility of a CVD process could be determined with the Gibbs free energy of the reaction, which could be calculated by using the free energy of formation of reactants and products. During the CVD process, precursor and reactant are pulsed simultaneously, and the properties, growth behavior, and thickness of thin films are typically influenced with the nature of precursor, operating temperature, chamber pressure, reaction surface, and the time used for deposition. Compared with the other reaction-based vacuum deposition technique, atomic layer deposition, CVD offers a higher growth rate through sacrificing the accurately uniformity and thickness control.

Atomic layer deposition is a technique that utilizes sequential precursor gas pulses to deposit thin film one monolayer or submonolayer at a time base on its alternate self-limiting surface reactions [38]. During ALD process, vapor of different reactants are sequentially pulsed into reactor chamber, and each of reactant pulse are followed by inert gas purging or evacuation to clean reactant residue in gas phase and/or physically adsorbed on reaction surface. Therefore, this deposition route could effectively prevent reactants from reaction in gas phase and induce unique self-limiting surface deposition mechanism. Compared to other deposition techniques, such as physical vapor deposition and chemical vapor deposition, atomic layer deposition offers several favorable benefits, including precise thickness control, low impurity, good stoichiometry, excellent uniformity and conformity [37], which enable versatile possibilities for emerging applications, such as high-κ technology, ultra-thin emasculating layer for passivation, and ITSOFCs. More details about ALD will be introduced in chapter 3.1.1.

2.2. Titanium Oxide-based High-κ Materials

Thin structures with high-dielectric-constant are one of the key components for improving the performance of semiconductor devices, such as metal oxide semiconductor (MOS) transistors and dynamic random access memories (DRAMs) [12, 39-42]. So far, a variety of high-κ candidates, including HfO_2, ZrO_2, La_2O_3, Y_2O_3, and TiO_2, have been proposed and investigated as replacements of conventional SiO_2 and SiON [12, 43, 44]. Among these materials, TiO_2 has been considered to be one of the leading candidates because of its high dielectric constant, 40 for amorphous or anatase structures and 80 or

higher for rutile structure [45]. However, crystalline TiO_2 often yields severe leakage current density (~1 A/cm^2 at 1 V), because its polycrystalline structure induces a large amount of grain boundaries, which serve as high leakage and Si dopants (i.e., B or P) diffusion paths [11, 13, 45, 46]. In addition, structural transitions and multiphase crystalline TiO_2 yield variable electrical properties, such as uneven capacitance values and leakage current characteristics among different regions.

In order to improve the properties of TiO_2 for high-κ applications, considerable interests have been focused on the stabilization of TiO_2 in its amorphous state by doping it with other high-κ metal oxides, such as Al_2O_3, HfO_2 , ZrO_2, Ta_2O_5 and Ln_2O_3 [45-48]. For instance, Jeon et al. reported that addition of praseodymium into titanium oxide films using E-beam evaporation made it possible to achieve amorphous films with a dielectric constant of ~23 and a leakage current density of ~10^{-5} A/cm^2 at −2 MV/cm on Si [49]. However, PVD is typically limited for the fabrication of devices with three-dimensional features. As the development of thin film fabrication technologies, ALD has been widely recognized as a powerful means of fabricating high-κ films in semiconductor industry. Because it matches the demanding requirements for fabricating CMOS and DRAM devices, including precise thickness control, high uniformity and conformity. Co-ALD of ZrO_2 and TiO_2, $Zr_xTi_yO_2$, had been previously investigated and found to result in films with a dielectric constant of ~20 and a leakage current of 10^{-5} A/cm^2 at 1 MV/cm, while its preferred amorphous state was able to be maintained up to 600 ℃ [46]. A recent study of Al-doped TiO_2 dielectric deposited with ALD showed that the incorporation of Al could result in mostly amorphous ternary oxide throughout necessary annealing processes

(less than 400 ℃), thereby reducing the leakage current density of anatase TiO_2 (10^1 A/cm^2 at 0.16 MV/cm) on a TaN electrode [45]. However, it was reported that optimized $AlTiO_x$ dielectrics were found to be incompatible with Si electrodes and yielded a leakage current density of 10^{-4} A/cm^2 at 0.16 MV/cm [45]. The ALD and annealing behavior of TiO_2 films doped with HfO_2 had been investigated and the Ti-rich $Hf_xTi_{1-x}O_2$ films were found to be amorphous even after annealing at 800 ℃ [48]. An amorphous Ta-doped TiO_2 dielectric deposited with ALD was reported, and this composited films exhibit a slightly high leakage current density of 10^{-3} A/cm^2 at 1MV/cm [47]. Erbium oxide, as a novel high-κ candidate, is of particular interest due to its large conduction band offset to Si (3.5 eV), low leakage current density (10^{-8} A/cm^2 at 1 V), and a moderate dielectric constant (10-14) [50, 51]. Thereby, Er_2O_3 could be a potential dopant for improving the properties of ALD TiO_2.

2.3. Recent Investigation of III-V Semiconductor Passivation

Previous studies of III-V semiconductor passivation have been mainly focused on sulfur passivation based on the use of aqueous solutions of inorganic or organic sulfides, such as sodium sulfide (Na_2S) [24, 52], ammonium sulfide [$(NH_4)_2S$] [26, 53], and thioacetamide [27, 54]. Recently, Banerjee at al. studied the short- and long-term passivation effectiveness of InAs/GaSb superlattices treated with aqueous ammonium sulfide solution [26]. It has been reported that the reoxidation of Ga and Sb could be apparently observed after exposing the sample to air for 30 min, and the amount of oxides is found to significantly increase after exposure to air for 10 days [26]. Compared to ammonium sulfide solution treatment, the TAM-based treatment has been reported to

provide superior passivation for GaSb-based surfaces. As seen in figure 3 reported by Stine et al., no oxide could be found on the TAM-treated surface even after exposure to air for 4 hours, and the antimony oxide appears after 3 days [27], indicating a better passivation efficacy possibly due to a thin layer for sulfide encapsulating film resulted from TAM treatment. In addition, TAM solution treatment offers several advantages such as milder reaction conditions and the ability to passivate surfaces under both acidic and basic conditions. However, TAM-based passivation offers good protection against oxidation only for a short term of less than 3 days [27].

In order to maintain long-term stability of passivated III-V semiconductor surfaces, a thin solid layer of encapsulating material has been under investigation. For instance, Gin et al. investigated the surface passivation of type II InAs/GaSb superlattice photodiodes using a 150 nm-thick layer of SiO_2 deposited with plasma enhanced chemical vapor deposition, which enhances the device resistance and exhibits lower reverse bias dark current [55]. More recently, Banerjee et al. evaluated the passivation efficacy of 30 nm-thick encapsulating layers made use of different materials, including ZnS, SiO_2, and Si_xN_y, for long-wavelength infrared InAs/GaSb strained layer superlattices [25]. Those thin layers of ZnS, SiO_2, and Si_xN_y were deposited, after ammonium sulfide treatment, using different techniques, molecular beam epitaxy, plasma enhanced chemical vapor deposition, and sputtering deposition. By comparing the resistance–area product and dark current density, it was found that ZnS capping film offers superior passivation efficacy over SiO_2 and Si_xN_y films [25]. The ZnS-passivated diode yields a high surface resistant of 2500 Ω-cm and exhibits a maximum zero-bias

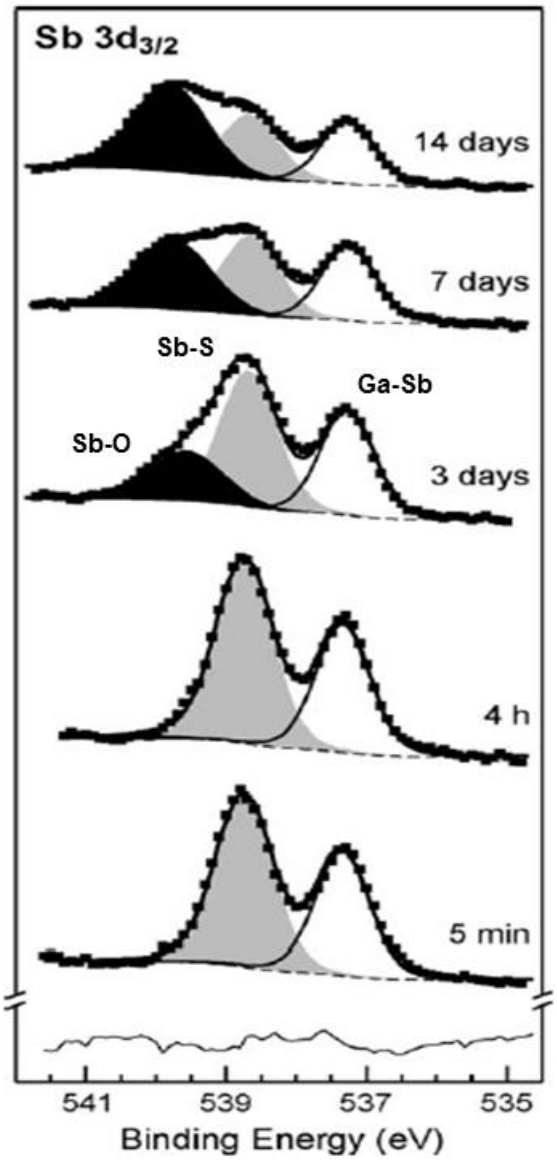

Figure 3. XPS Sb $3d_{3/2}$ core level spectra of TAM-treated GaSb samples. The TAM-treated samples were exposure to aire for 5 min, 4 h, and 3 to 14 days [27]

resistance–area product of 492 Ω-cm^2, which is three orders of magnitude higher than that of uncovered devices [25]. To further improve the passivation, ultra-thin films fabricated with ALD would be a promising encapsulating layer, because the ALD at lower temperature could prevent the superlattice structure from being damaged while yielding pinhole-free amorphous thin encapsulating film with high conformity for all dimensions. All of these characteristics would potentially enhance the passivation efficiency and enable more possibilities.

2.4. Atomic Layer Deposition of Thin Structures for Intermediate-Temperature SOFCs

Implementation of ultra-thin films, in nanometer scale, has been widely identified to be an effective means of increasing ionic conductivity of electrolyte in ITSOFCs [31]. For electrode, very thin porous structure with good electrical conductivity is desired to enhance the transport of fuel and oxidant gases [56]. Therefore, novel fabrication technique is required to satisfy the criteria, and a few additional requirements, such as fully coverage of three-dimensional features with dense and/or porous films, would be also important to enhance the efficiency of ITSOFCs.

ALD is a powerful deposition technique which is capable to yield highly uniform dense ultra-thin films [57]. Recently, ALD has been under investigated for the purpose of developing high efficient and low working temperature SOFCs [58-60]. In early 2000s, ALD was first applied for depositing electrolyte material, YSZ with 8 mol% of yttria, generally on soda lime glass and silicon as well as Ni-YSZ cermet, and the mainly

employed metal precursors were chloride, β-diketonates, and cyclopentadiene-ligand precursors with moisture and ozone as oxidant [61, 62]. In 2007, Shim et al. reported a free-standing structure made use of 60 nm-thick ALD YSZ sandwiched with 80 nm-thick sputtered Pt porous film as cathode and anode, and this structure yields a maximum power density of 270 mW/cm^2 at 350 ℃ due to its thin electrolyte and gas penetrable electrodes [32]. One year later, Su et al. reported a three-dimensional free-standing structure, consisting of 70 nm-thick ALD YSZ as electrolyte and 120 nm-thick sputtered Pt as electrode, for low-temperature SOFC application, which shows an enhanced maximum power density of 677 mW/cm^2 at 400 ℃ as a result of the increased surface area [63]. Ultra-large free-standing structure, in cm scale, was achieved, in 2011, by using ALD YSZ and 1.5 μm-thick Pt grid [64].

Also, ALD of electrical conductive materials, such as oxide or Pt, is of importance to empower the fabrication of electrode for ITSOFCs. Pt deposited with ALD has been deposited for electrode application, and the ALD process were mainly based on the use of (methylcyclopentadienyl)trimethylplatinum as metal precursor and oxygen as oxidant [65], however, the power of the resulted SOFCs is found to firstly increase and then decrease as the thickness of ALD Pt increasing. This might be related to the morphology of Pt film, such as island, porous, or highly dense. Therefore, the nucleation and morphology investigation of electrically conductive ALD materials would be important, which could be potentially utilized to obtain desired porous structure and enhance the performance of electrode.

3. EXPERIMENTATION AND CHARACTERIZATION TECHNIQUES

3.1. Applied Thin Film Deposition Techniques and Annealing Furnaces

3.1.1. Custom Designed & Made ALD System

ALD is a technique that utilizes sequential precursor gas pulses to deposit thin film one monolayer or submonolayer at a time base on its alternate self-limiting surface reactions at low pressure (0.5-1 torr). During ALD, vapor of different reactants are sequentially pulsed into reactor chamber, and the pulses of different reactants are separated by inert gas purging or evacuation. This deposition route could effectively prevent different reactants from reaction in gas phase, and induce unique self-limiting surface deposition mechanism. Compared to other deposition techniques, such as physical vapor deposition, sol-gel deposition, and chemical vapor deposition, atomic layer deposition therefore offers several favorable benefits, including precise thickness control, excellent uniformity and conformity.

The ALD system used, in our study, is a horizontal hot wall tubular ALD reactor with a quartz tube chamber (38 mm in diameter and 48 cm in length) [66]. The reactor can be operated at a temperature up to 600 ℃ (custom modified processing furnace, model 1043 Marshall, ThermCraft Inc.) and typical depositions can be carried out at the temperature range of 25–450 ℃. A K-type thermocouple is attached on the reactor chamber wall, which is just below the substrate holder for temperature monitoring. The substrates are mounted in a quartz holder and located at the center of the reactor with the substrate surface perpendicular to the gas flow. The base pressure of the ALD chamber is

less than 20 mTorr. There are four precursor lines on this system (the other two lines are not shown in Fig. 4), and this system therefore could deposit at least four different materials. A LabVIEW program is designed and written to control pneumatic valves, which could indeed control the gas delivery in the ALD system. The bubbler pressure is generally maintained at 10–12 torr. The bubbler temperature is determined by thermal gravimetric analysis and vapor pressure of precursors. The delivery line section from the bubbler to the reactor is maintained 20–30 ℃ higher than the bubbler temperature in order to prevent precursor condensation during delivery. The oxidant for ALD of oxides is a mixture of O_3 and O_2 (1000 ppm ozone) generated with O_2 (99.999% purity) flow through a UV lamp ozone generator immediately upstream of the deposition reactor. On the other hand, H_2S or O_2 gas is applied for deposition of sulfide or metal, respectively. Ar (99.999% purity) is used as both carrier gas for the metal precursor delivery and purge gas for the clean of system between the pulses of different reactants.

During deposition, the reactor pressure is maintained at 0.5 torr, which is a trade of between gas entrainment and interdiffusion. The Reynolds number of gas flow is typically less than 2100 to maintain laminar flow, which could effectively improve the gas delivery and purge. A cold trap is located between the ALD chamber and the mechanical pump, to prevent the residual precursors from condensation in the pump. The pump oil is changed every three months.

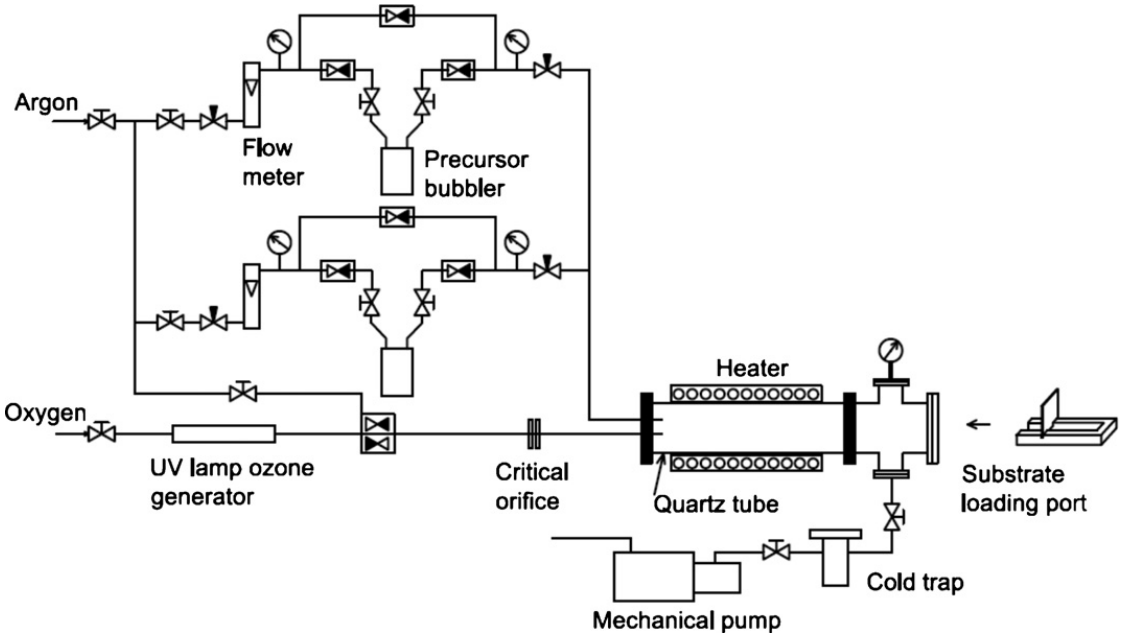

Figure 4. Scheme of the custom designed & made ALD reactor (only two precursor lines are shown).

For deposition of different materials (e.g., oxide, sulfide, or metal), one ALD cycle typically consists of four steps: (i) pulse of the first precursor (metal organic precursor); (ii) purge of the reactor chamber using Ar gas; (iii) pulse of the second precursor (O_3, H_2S, or O_2 for deposition of oxide, sulfide, or metal, respectively); (iv) purge of the reactor with Ar gas. In the first step of an ALD cycle, metal organic precursors in the gas phase chemisorb on the surface of substrate due to the reaction between precursor and active site, and the saturate adsorption of precursor is required to achieve the self-limiting mechanism. Next, Ar gas is used as purge gas to remove residual precursors in the gas phase and/or physisorbed on the substrate. In the third step, the second precursor (e.g., O_3 for deposition of oxide) is applied and fed into the ALD chamber, reacting with adsorbed precursor (metal organic precursor) on the reaction surface and forming a layer of film. In the last step, Ar gas is used as purge gas again to remove the unreacted precursor and byproduct of surface reaction. The ALD parameters, such as pulse and purge duration of each precursor and ALD cycle number, could be controlled by using a LabVIEW program. For a new deposition route, an optimization process should be carried out to obtain the ALD mechanism. Since each ALD cycle exactly produce a layer of film based on its self-limiting behavior, the thickness of resulting films could be precisely controlled by ALD cycle number. For ALD of composite films (e.g., ternary oxides), composition tunability could be achieved with ALD process control, and an overlapping ALD temperature window of different processes is desired and often enhance the reproducibility of resulting structures. The composition of ternary films can be controlled by varying ALD cycle ratio of the constituent binary processes.

3.1.2. Electron Beam Evaporation System

Electron beam evaporation is the most prominently used physical vapor deposition technique, in which a target anode is bombarded with an electron beam emitted from a tungsten thermal electron emission filament in high vacuum environment (10^{-6} torr). The kinetic energy of electron beam is transfer to thermal energy on the target surface, leading to high temperature and causing a relatively high vapor pressure of target for the deposition. Electron beam evaporation could be used to deposit a variety of materials, such as oxide or metal. This deposition route generally yields a relatively high deposition rate in the range of 0.01–410 nm/s at low substrate temperature [36].

Figure 5 shows the scheme of electron beam evaporation system used in this work. Prior to deposition, system chamber could be opened by filling the chamber with 1 bar N_2 gas. The substrates are mounted on the holder with frame structure, which is then placed in the chamber for deposition. The deposition chamber is firstly connected to a rough pump to reduce the chamber pressure to 1 mtorr. Next, a cryo pump is applied to reduce the pressure of chamber to 10^{-6} torr. The high vacuum environment is required to allow the target to evaporate freely in the chamber and prevents chemical reactions during the evaporation. The electron beam could be generated by a tungsten thermal emission filament. The resulting electron beam is accelerated and bended with electrical and magnetic field, respectively. Typically, the voltage used for the acceleration of the electron beam is ~10 kV, which significantly increase the kinetic energy and current of

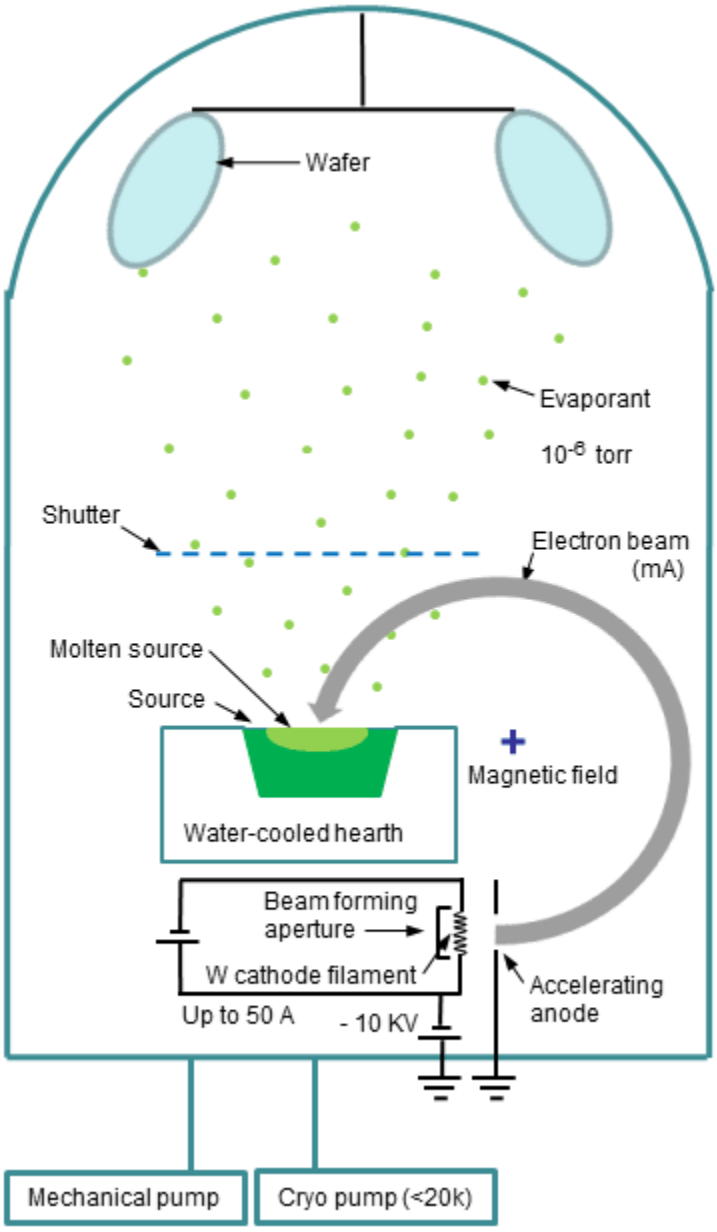

Figure 5. Scheme of electron beam evaporation.

the emitted electrons. The electron beam current is in the range of 10–200 mA. The position of the area that the beam bombards could be adjusted by magnetic field. When the electron beam bombards the target surface, kinetic energy of the beam is transferred to thermal energy, therefore sharply increasing the target surface temperature, enhancing the evaporation, and raising the deposition rate to the range of ~0.01–1.0 nm/s. The temperature of target holders is maintained at a relatively low temperature by using a water cooling system, which could effectively prevent any reaction or diffusion between the target and its holder. A shutter located on the top of the target is equipped in the chamber, and the shutter could precisely control the time of deposition and the thickness of resulting films. Based on the deposition of different materials, 10–20 mins of cooling time is needed after the deposition, and the low temperature of substrates could reduce the reaction between thin film and air, for example the undesired oxidation between metal films and O_2 in air.

3.1.3. Rapid Thermal Processing Furnace

Rapid thermal processing technique has been widely used in Si integrated circuit technology for annealing of metal-insulator-semiconductor structures at temperatures between 250 to 1200 ℃ [67, 68]. The rapid thermal processing meets demanding requirements, such as precise temperature control, uniform temperature profile of large wafers, and good compatibility with a variety of gas treatments. The rapid thermal processing furnace used is from Modular Process Technology Corporation with a model number of RTP-600S, and it could provide multifunctions, including real-time graphics, recipe management, data acquisition and display [69]. The size range of wafers treated is

from 2 to 6 inch in diameter. The rapid thermal processing furnace consists of a slim quartz chamber and tray, and the operation could be controlled with computer programs [68, 69].

As seen in Fig. 6, the wafer needed to be annealed is loaded on quartz tray with a K-type thermal couple contacting the bottom side of the wafer, and the wafer is then slide into furnace chamber. The temperature measurement of this system is based on the use of a K-type thermal couple and a pyrometer. The K-type thermal couple could be applied for precisely low temperature measurement and calibration of pyrometer, and the extended range pyrometer plus pyrometer is available to measure the temperature of the wafer in the range of 350-1250 ℃ [68, 69]. The lamp calibration feature enables user-optimization of temperature uniformity during annealing, and software diagnostics are available to monitor each lamp in the array and compensate for lamp aging effects [69].

The rapid thermal processing could be started at a temperature equal to or less than 25 ℃. The heating chamber of RTP-600S furnace consists of upper and lower series of tungsten halogen lamps, 10 lamps on the top and 11 lamps on the bottom of the furnace, which provide radiation for the uniform heating of wafers. The maximum heating rate of this furnace is 200 ℃/s. The stead-state temperature accuracy is ±2 ℃.

The cooling system of the furnace includes two parts [68]. The first part is the water cooling subsystem, which allows cold water (15 ℃) reduce the temperature of hot furnace wall and door. The second pat is the gas cooling subsystem, which provides the

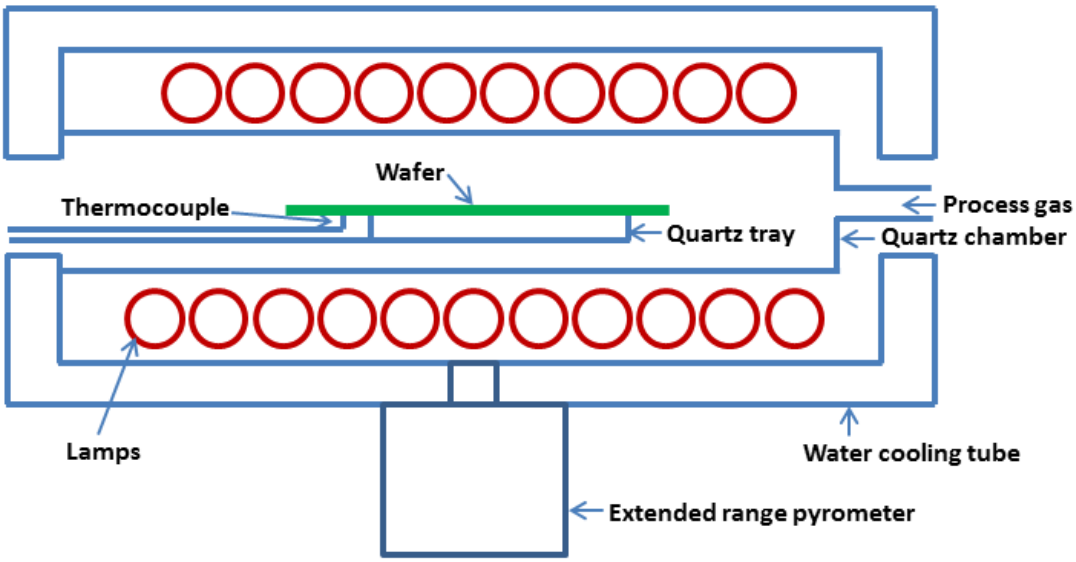

Figure 6. Scheme of rapid thermal processing furnace.

continual flow of gas (e.g., N_2, Ar, or Air) in the quartz chamber to remove the residual heat in the chamber . The maximum cooling rate is 150 ℃/s.

The RTP-600S furnace could be used for a variety of thermal processes, such as contact alloying, implant activation, silicide formation, nitridation of metals, oxidation, glass reflow [69]. In our study, rapid thermal processing was carried out at 700 ℃ in O_2 environment for 30 s. The O_2 used has an ultra-high purity (99.999%). The ramp time was 30 s for the heating and cooling processes.

3.1.4. Three-Zone Post-Deposition Annealing Furnace

The post-deposition annealing furnace (Lindberg Blue three-zone furnace) is a useful tool for annealing processes of thin structures on wafers with variable sizes (up to 3 inches in diameter), and the furnace can be carried out over a wide temperature range of 200–1100 ℃ in different gas environments, such as N_2 (99.999% purity) or H_2 with low concentration (4 mol% of H_2 in N_2).

As seen in the figure 7, the furnace has three annealing zones with equal length of ~8 inches for each zone [70]. The temperature of three zones is controlled independently, and the three zones are generally maintained at the same condition to keep the whole chamber heated uniformly. Prior to the thermal treatment, the chamber of the furnace is purged with N_2 (99.999% purity) for 20 min. The post-deposition annealing is typically carried out in N_2 at 1 bar with constant flow rate of ~44 sccm. For annealing, the sample is mounted in the middle zone of the furnace chamber, and a quartz boat is used to hold

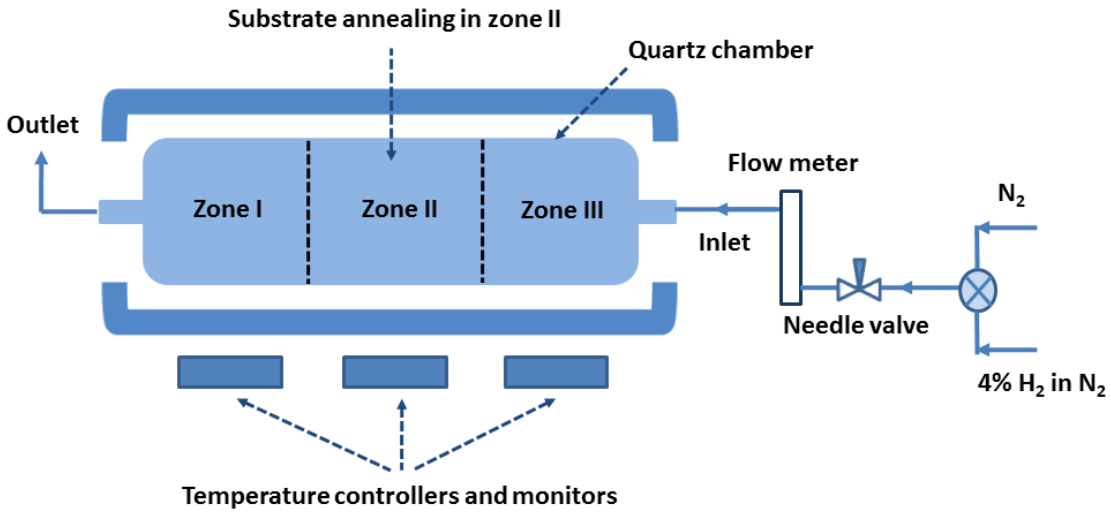

Figure 7. Scheme of three-zone post-deposition annealing furnace.

samples during high temperature process (e.g., 1000 ℃). To investigate the effect of different annealing temperatures on structures and interface of thin structures (e.g., metal oxide/semiconductor), the typical annealing time is set for 5 min and the annealing temperature varies from 600 to 1000 ℃.

3.2. Characterization Techniques

3.2.1. Spectral Ellipsometry

Spectral ellipsometry is a very powerful non-destructive technique for measuring thin film thicknesses (typically, in the range 1-1000 nm) and refractive index in single or multilayered structure. The ellipsometry system is shown in Fig. 8 [71]. As seen, the ellipsometry system mainly includes the following components: xenon lamp, polarization generator, sample mount, rotating polarization analyzer, detector, and ellipsometer control module.

The measurement procedures are shown in Fig. 9 and described as follows [71, 72]. An incident light beam produced by a xenon lamp firstly travels through a polarizer, which only allows the light with a preferred electric field orientation to pass. Next, the linear polarized light interacts with the thin film on substrate, and the reflected light becomes elliptically polarized due to amplitude and phase changes in both p- and s-polarized light. The polarization state of the reflected light is then analyzed by passing through a continuously rotating polarizer. The detector could convert light to electronic signal for determining the polarization of reflected light by computer. The change in polarization (ρ) is the ellipsometry measurement, commonly written as [73]:

$$\rho = \tan\psi \, e^{i\Delta}$$

The thickness of films is typically determined by the interference of light reflecting from the film surface and light traveling through the film, and the interference includes both amplitude and phase information. In the measurement, the thickness

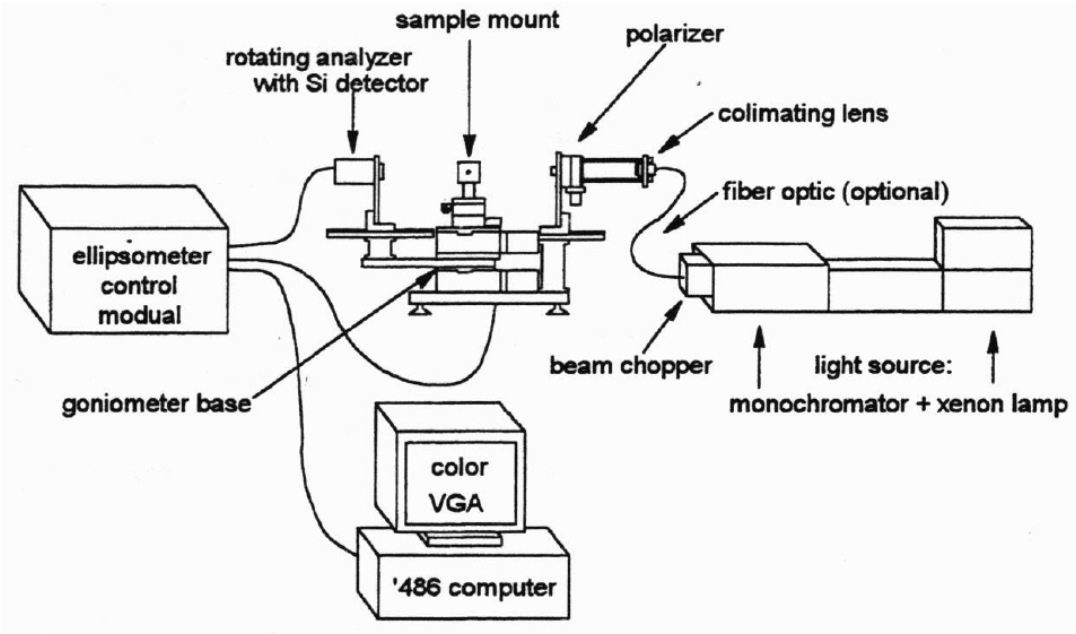

Figure 8. Scheme of ellipsometer system with xenon lamp as light source [71].

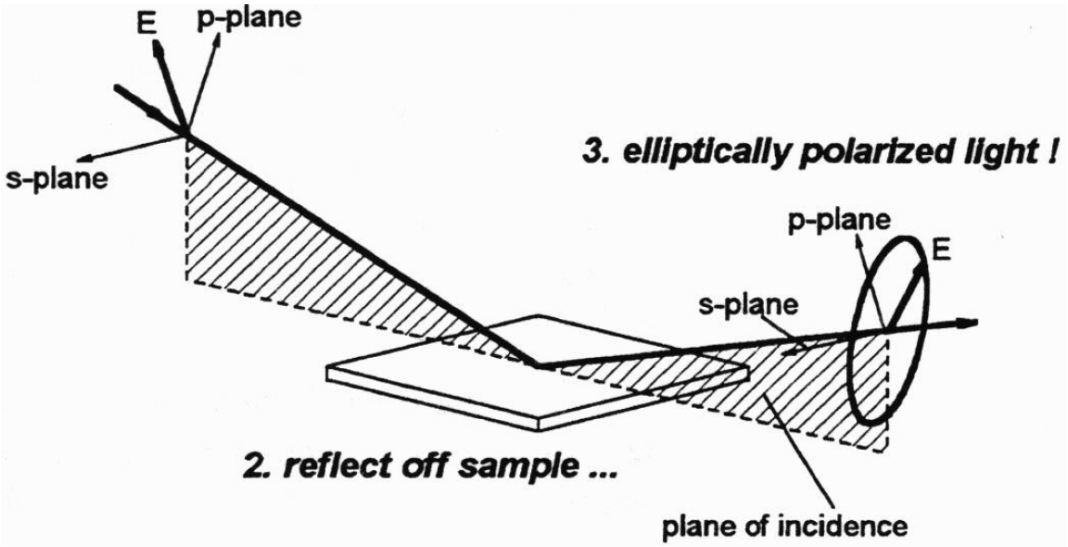

Figure 9. The measurement procedures of the spectral ellipsometry [71].

measurement is also dependent of the optical constants of the material. Because, on the one hand, the film thickness affects the optical path length in the film, and, on the other hand, the optical constant determines the velocity and refracted angle of light. Therefore, optical constants must be known or determined along with the thickness to obtain the correct results[71, 73, 74].

Data analysis proceeds as follows [73]: After collecting the data of a measurement, a model is built for describing the structure of the sample, including both film and substrate. Next, the model is applied to calculate the predicted sample information which includes thickness and optical constants. If any properties are unknown, an estimate data is given for the preliminary calculation. Base on the comparation between calculated and experimental data, any unknown properties of thin film can then be varied to improve the fit between experimentation and calculation. Calculating the best fit between the simulation and experiment data is often carried out upon regression analyses. An estimator, such as mean squared error, could be used to quantify the difference between calculation and experimentation curves. The unknown parameters are varied during fitting process, until the minimum mean squared error is obtained.

In this work, film thicknesses and optical constants are measured with a spectral ellipsometer (Model M-44, J. A. Woollam Co.) equipped with a Xenon arc lamp (UXL-75XE USHIO America Inc.). The light covers a wide wavelength range, from 400 to 750 nm [72]. For each thickness determination, three measurements across the entire

deposition area are carried out with mean values representing film thickness and standard deviation indicating thickness variation.

3.2.2. X-ray Photoelectron Spectroscopy

X-ray photoelectron spectroscopy is one of the most widely used techniques for the elemental analysis, and it could provide accurate information of the near surface region of samples, such as empirical formula, elemental composition, chemical binding state, and electronic state [75, 76]. The high-resolution XPS system enables the studies in various areas, including oxidation, corrosion, adsorption, catalysis, adhesion behavior, and thin film growth [77].

As seen in Fig. 10, during the XPS measurement, a beam of soft x-ray photons is generated by electrons bombarding metal target and applied to radiate the sample while simultaneously measuring the kinetic energy and number of photoelectrons emitted from the sample surface (1-10 nm). XPS requires high vacuum environment (10^{-9} torr) to eliminate the photoelectrons escaped from gas phase and to prevent scattering of photoelectrons in the chamber [76].

The chemical state of an atom determines the binding energy of a photoelectron, and the change in the chemical state could therefore lead to the change in the measured kinetic energy of a photoelectron. The binding energy is related to the measured photoelectron kinetic energy by the simple equation:

$$\mathrm{BE} = \mathrm{h}\gamma - \mathrm{KE}$$

, where hγ is the x-ray photon energy (1486.6 eV for Al Kα). The chemical or bonding information of the element is able to be derived from the shift of the chemical state in term of binding energy. The elemental composition of a sample is achieved by measuring the number of photoelectrons of each element during a period of time, for example, 1000 count/min. The area of an element peak divided by its sensitive factor is the relative amount of that element in the sample, which indeed could be applied to estimate the elemental composition.

In this work, chemical bonding states of films are probed with a high resolution XPS (Kratos AXIS-165, Kratos Analytical Ltd.) equipped with a monochromatic Al Kα (1486.6 eV) x-ray source operating at 15 kV and 10 mA. The energy width of the monochromatic x-ray is 0.16 eV. The filament current is 1.6–2.1 A. The working pressure of the XPS system is 10^{-9} torr. High resolution XPS spectra of the elements-of-interest are collected at a take-off angle 90 ° using pass energy of 20 eV, step size of 0.1 eV, and dwell time of 200 ms. The Carbon 1s line at 285 eV is used to calibrate the binding energy scale of the XPS spectra. The analyses of films are performed through XPS spectral peak-fitting (XPSPEAK 4.0 software), where peaks are subtracted from Shirley-type backgrounds and deconvoluted using Gaussian-Lorentzian peak shape functions.

As seen in fig. 10, an Ar^+ beam gun is installed in the XPS system to sputter depth profile. The Ar^+ beam is a gentle etching process for the removal of undesired surface contamination of sample and enable the XPS investigation of bulk film or underlying

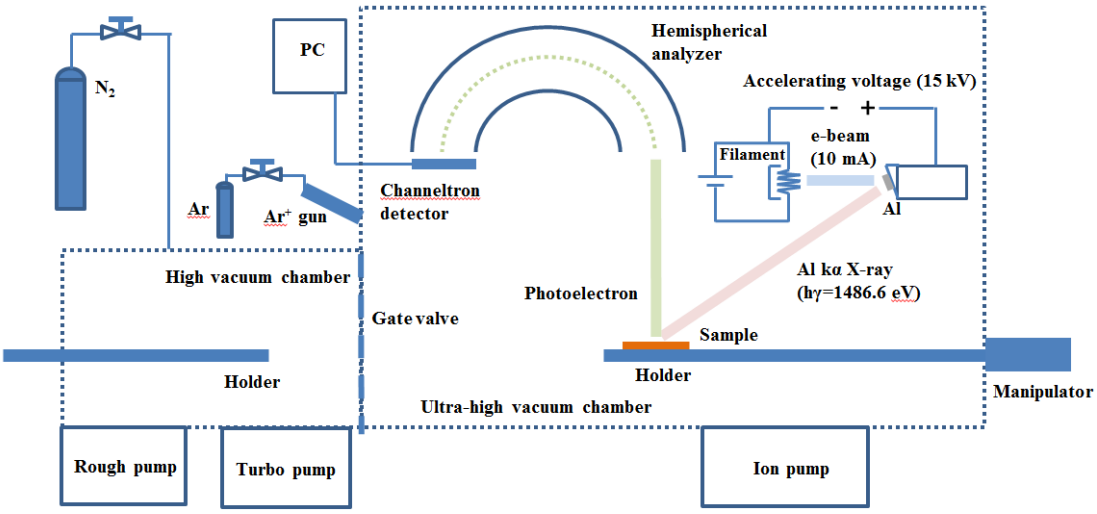

Figure 10. Scheme of XPS system equipped with Ar^+ beam gun.

structure. However, some materials, such as TiO_2, are very sensitive to the Ar^+ beam sputtering, and the sputtering process might change the binding energy and composition of materials [78]. In this work, Ar^+ beam sputtering is carried out at 4 kV and 200 nA, yielding a puttering rate of ~0.1 nm/min.

3.2.3. X-ray Diffraction

X-ray diffraction is a rapid non-contact technique for determining the structure of a variety of materials, ranging from simple inorganic to macromolecular organic, such as polymer or proteins [79, 80]. The XRD pattern could be used to extract structural details, including unit cell dimension, preferred orientation, lattice constant, grain size, crystallinity, stress, and defects [81, 82].

XRD characterization mechanism is based on the constructive interference of monochromatic x-ray waves diffracted from crystalline materials [83]. The constructive interference is observed in the XRD spectra, when conditions satisfy Bragg's equation.

$$n\lambda = 2d \sin\theta$$

In Bragg's equation, n is an integer, λ is the wavelength of the x-ray, d is the space between the lattice planes, and θ is the diffraction angle between the incident x-ray and the scattering lattice plane. Therefore, Bragg's equation can be applied to calculate the space between lattice planes. The average grain size in a material is often determined using Scherrer's quation:

$$D = \frac{k\lambda}{B \cos\theta}$$

, where D is the average grain size, k is a constant dependent on crystallite shape (0.89 for ball), B is the full-width half-maximum of the diffraction peak (rad as unit), and θ is the diffraction angle. The crystallinity can be estimated using the intensity of diffraction peak divided by the total intensity.

Figure 11 shows the configuration of a XRD system. The electron beam in the XRD technique is typically generated with a tungsten thermal electron emission filament. The x-ray beam is emitted from metal target when the electron beam bombards the metal targets, because the vacancy of electron in the core level is filled with outer electron while releasing x-ray photon. The x-ray beam is filtered to achieve monochromatic x-ray. The X-ray photons are then elastic scattered with the sample and the constructive interference of scattered x-rays results in diffraction peaks.

In this work, an x-ray diffractometer (X'pert, PANalytical BN Co.) is performed to achieve glancing incidence x-ray diffraction patterns of thin films. The filament is operated at 45 kV and 40 mA during measurement. The x-ray beam is filtered with Ni film. Therefore, monochromatic Cu kα x-ray emission line (λ=0.1542 nm) with a bandwidth of 0.05 nm is generated and used for characterization. The overall diffraction angle (2θ) resolution is 0.15º. GIXRD diffractograms are collected at an incident angle of 1 ºto enhance diffraction sensitivity within the film and to minimize interference from the single crystal Si (100) substrate. The crystalline features are identified using the International Center for Diffraction Data database of diffraction pattern Powder Diffraction Files.

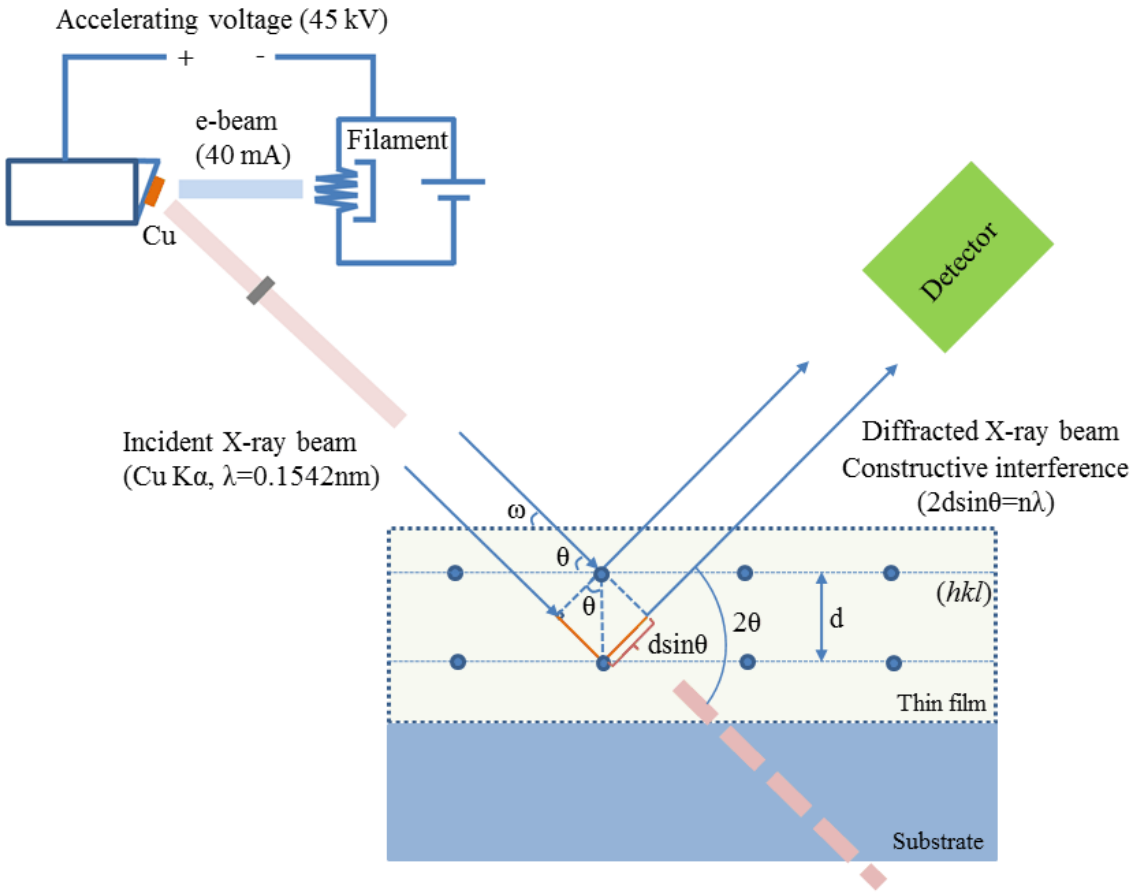

Figure 11. Scheme of XRD system with a monochromatic Cu Kα x-ray source.

3.2.4. Fourier Transform Infrared Spectroscopy

FTIR is a technique that has been widely used for identifying chemical bonds, composition, crystalline structure, and crystallinity of organic or inorganic materials [84-86]. FTIR spectroscopy utilizes infrared light with a wide range of wave number generally from 4000 to 1 cm^{-1}, which could be selectively absorbed by specific chemical bonds or structures of materials. Therefore, the resulting spectrum of FTIR spectroscopy could record the information of absorption and transmission of the infrared light and, as a result, present the chemical or structural details of sample [87, 88]. FTIR spectroscopy is typically equipped with an interferometer, in order to fits the need to preliminarily record the intensity as a function of optical path difference. In addition, compared with traditional spectrometers, FTIR is a fast and low-cost characterization technique, because the collecting of the information at all wave number is done simultaneously, and building of an interferometer is much easier than a monochromactor [89].

Figure 12 shows the simplified configuration of a FTIR system. Infrared light firstly pass through an interferometer and two parts of the light are reflected by a moving mirror and a stationary mirror. The combined infrared light reflected by mirror travels through the thin film sample. The infrared light after passing the sample could be detected by a thermal couple sensor and convert to light intensity. This intensity is a function of optical path difference, and this resulted spectrum is named interferogram. A mathematical Fourier transform is then applied by a computer in order to convert the intensity as a function of wave number. After subtracting the background spectrum, the resulting spectrum could be used to identify chemical or structural details of the sample.

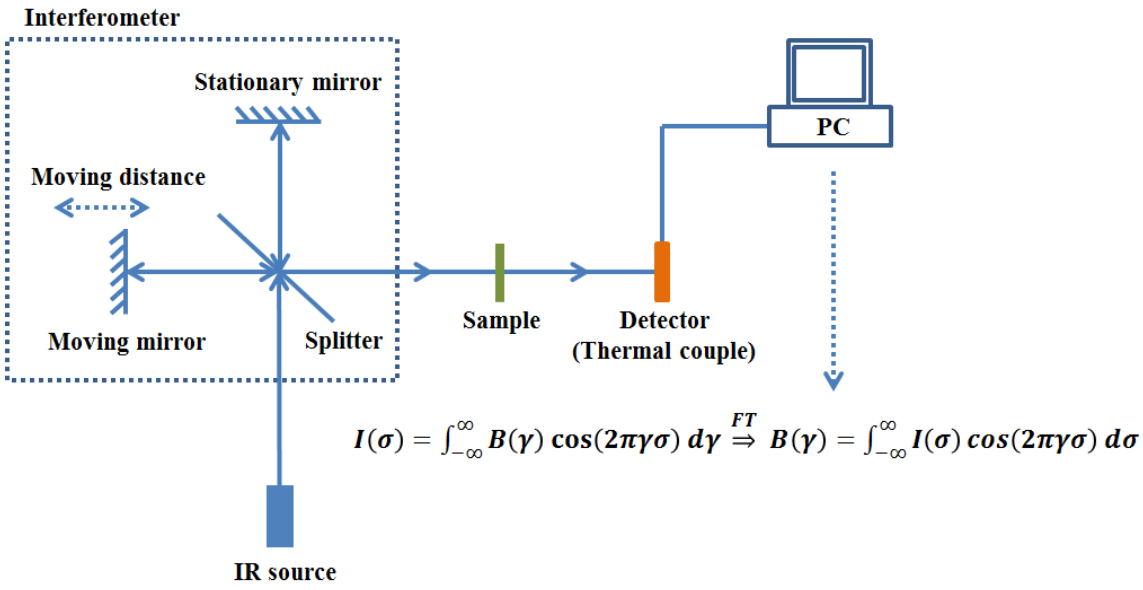

Figure 12. Scheme of FTIR spectroscopy system with transmission mode.

FTIR spectroscopy (Nicolet, Magna-IR 560) is used in the transmission mode over the wavelength range of 4000-400 cm^{-1}. Spectrum of RCA-SC1 cleaned Si(100) substrate is used for background subtraction from spectra of thin film samples, such as metal oxide thin film deposited on Si (100) substrate.

3.2.5. Rutherford Backscattering Spectrometry

RBS is an analytical technique used to determine the composition and thickness of materials [90]. The measurement process is based on elastic collision between high kinetic energy ion particles and stationary particles. During collision, high kinetic energy ions are scattered from atom nuclei in a sample. By measuring the high kinetic energy loss of ion particles, it could provide the information on sample composition as a function of depth [90-92].

The elastic scattering mechanism of RBS allows this measurement to follow the conversion of momentum and energy. Figure 13 shows the collision process during RBS measurement. The weight of atom nuclei in a sample could be calculated using the conversion equations of momentum and energy:

$$M_1 = M_1V_1 \cos\theta + M_2V_2 \cos\theta$$

$$0 = M_1V_1 \sin\theta + M_2V_2 \sin\theta$$

$$\frac{M}{2}V^2 = \frac{M_1}{2}V_1^2 + \frac{M_2}{2}V_2^2$$

, where θ is the scattering angle [91]. The amount of atom nuclei could be determined by counting the number of the scattered ion particles.

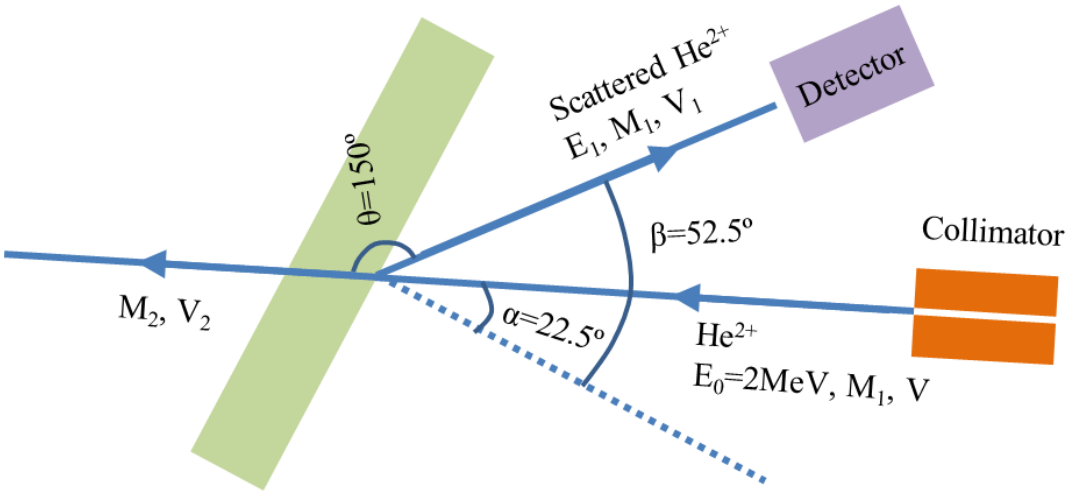

Figure 13. Scheme of RBS system and measurement process.

In this work, the bulk composition of the films is investigated using RBS with a general ionex tandetron accelerator (Model 5510, General Ionex Co.) employing 2 MeV He^+ particles. The beam size is 3 mm in diameter. The incident, exit, and scattering angles are 22.5, 52.5, and 150 º, respectively. The detector resolution is 26 keV and each channel covers 1.86 keV.

3.2.6. Phase Shifting Interferometry

PSI is a very simple and powerful means of technique for determining the roughness of very smooth surfaces in nanometer or even angstrom scale [93, 94]. Also, it is capable to measure the step height of 3D structures (step height less than 160 nm) [95]. It could supply precise information for surfaces that are smooth, hard or soft, adhesive, or deflectable, which allow it to match a wide range of applications, such as advanced materials, optics, plastics and polymers, coatings, and medical devices.

PSI is a noncontact profilometry, which based on the interference of light to produce high-precision images of the sample surface [94, 96]. The measurement utilizes a combination of waves, reflected from mirror and sample, with the same frequency and possibly different phases due to changes in optical path length, and the phase difference of waves determines that waves would undergo constructive interference or destructive interference [95]. The light intensity is then converted to phase data by using the following equation:

$$h\,(x,y) = \frac{\lambda}{4\pi}\Phi(\mathrm{x},\mathrm{y})$$

, where λ is the wavelength of the light, and Φ(x,y) is the phase data [93].

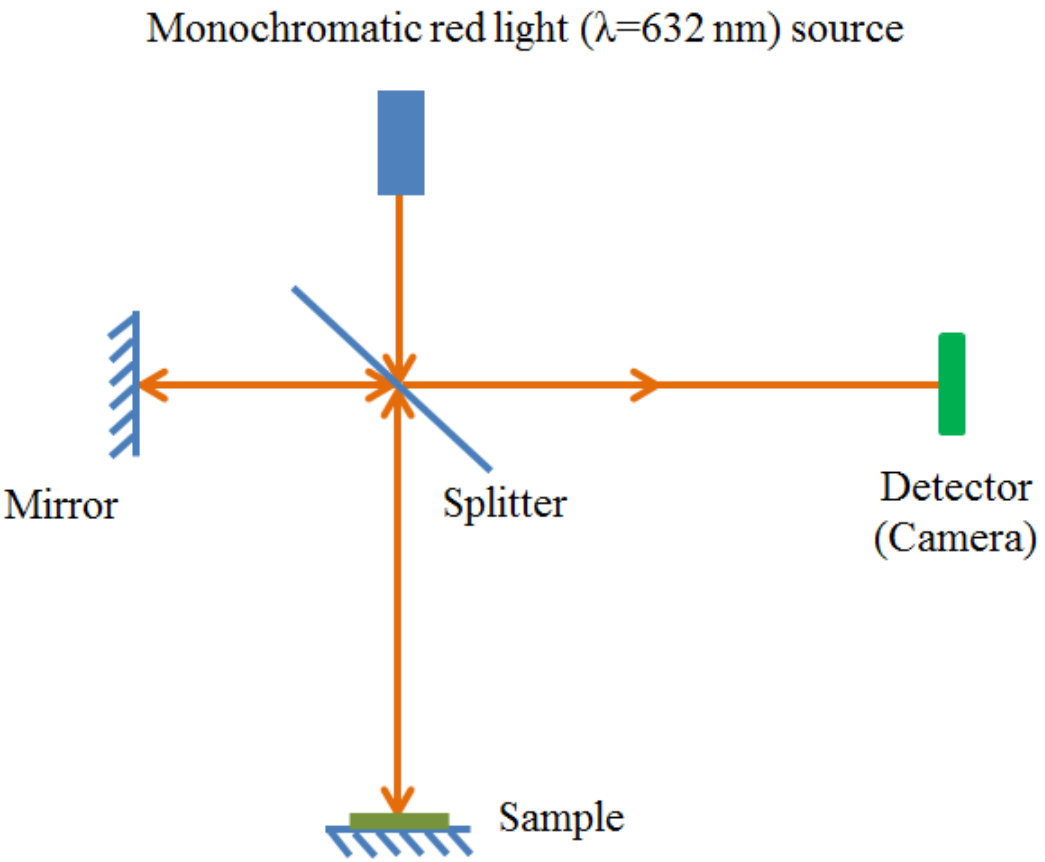

Figure 14. Scheme of phase shifting interferometry system with monochromatic red light source.

According to the measurement mechanism of PSI, PSI is limited to very smooth and continuous surfaces (e.g., step height less than 160 nm). Because, for example, if the height difference of two adjacent points on the sample surface is larger than λ/4, height errors in multiples of λ/2 could be induced and reduce the reliability of wavefront reconstruction [95].

Figure 14 shows the scheme of light path in PSI system. Monochromatic red light with wavelength of 632 nm is generated by a light source and then passes an interferometer. A part of the light reflected by a mirror, while the rest part of light reflected by sample. The combination of waves induces the interference of light, which could be detected by using a digital camera. The intensity of light is then converted to a high precision topography of the sample.

4. RESULTS AND DISCUSSION

4.1. Atomic Layer Deposition and Characterization of Stoichiometric Erbium Oxide Thin Dielectrics on Si(100) Using $(CpMe)_3Er$ Precursor and Ozone

4.1.1. Introduction

Structural, interfacial, and electrical studies of high dielectric constant (κ) materials are important in the continuous scaling of nanoelectronics such as complementary metal oxide semiconductors (CMOS) devices and dynamic random-access memories (DRAM) [12]. The use of traditional SiO_2 as a gate dielectric layer less than 1.5 nm-thick has reached its fundamental limit because of the excess direct tunneling leakage current. So far, various lanthanide oxides, such as Gd_2O_3, Pr_2O_3, and Er_2O_3, have been considered as pos-sible alternative gate dielectrics [97-103]. From these oxides, Er_2O_3 attracts increasing attention in terms of its large conduction band offset to Si (3.5 eV), moderately high dielectric constant (i.e. 9–14) and good thermal stability with silicon [97, 104-106]. In addition, when compared with other lanthanide elements, erbium has appropriate electronegativity and small ionic radius, which result in limited tendency to hydroxylation [107].

Er_2O_3 has been grown with various deposition techniques, such as RF sputtering [108], electron beam evaporation [109], metal–organic chemical vapor deposition [110, 111], and atomic layer deposition [51, 102, 112]. Among these techniques, ALD has been identified as a preferred technique for high-κ applications in order to maintain precise thickness at the needed dimensions within metal oxide semiconductor field effect transistors and to provide conformal coverage along the deep trenches of DRAM cells

[12]. In early ALD studies of Er_2O_3, the precursor used was mainly tris(2,2,6,6-tetramethyl-3,5-heptanedione) erbium, $Er(thd)_3$. For example, Paivasaari et al. used $Er(thd)_3$ with ozone as the oxidant and found the deposition process has a low growth rate (~0.025 nm/cycle) at temperatures between 250 and 375 °C [112]. The resulting erbium oxide thin films were reported to be oxygen-rich (O/Er = 1.7) with carbon, hydrogen and fluorine contents of 1.8, 4 and 1.7%, respectively. A higher growth rate and reduced impurities were demonstrated by using tris(amidinate) precursors, $Er(tBu_2amd)_3$, and ozone [102], i.e. ~0.05 nm/cycle at 270 °C. However, the growth rate was reported to increase with precursor pulse duration, which was likely due to partial thermal decomposition of $Er(tBu_2amd)_3$ during the precursor delivery process; the stoichiometric ratio O/Er of those films was found to be 1.8 with a carbon content of 1.8%. In both studies of β-diketonate and amidinate types of erbium precursors, as-deposited Er_2O_3 was found to be amorphous at deposition temperatures below 250 °C, but started to crystalize into polycrystalline cubic structure at a temperature of 250–350 °C. Recently, cyclopentadienyl precursors were used to deposit other metal oxide films [113-115]. When compared with β-diketonate and amidinate ligands precursors, cyclopentadienyl-type precursors exhibit good thermodynamic stability. In addition, cyclopentadienyl compounds have a relatively low sublimation temperature which leads to a high ALD growth rate due to its moderate vapor pressure [101, 116]. Tris(methylcyclopentadienyl)erbium, $(CpMe)_3Er$, was used with water vapor to deposit Er_2O_3 thin films on silicon [51]. The depo-sition rate was reported to be ~0.15 nm/cycle at 250–350 °C; the resulting films were found to be overstoichiometric (O/Er = 1.7) with

a carbon content of ~2.5%. The oxygen-rich O/Er composition was attributed to hydroxylation reaction between erbium oxide and water vapor.

In this study, the cyclopentadienyl ligand erbium precursor tris(methylcyclopentadienyl)erbium is used with ozone as the oxidant to deposit Er_2O_3 thin films on silicon(100) by ALD. A wide ALD window as well as a growth rate of 0.12 nm/cycle is found. Elemental quantitative analysis of as-deposited Er_2O_3 films indicates that the films are stoichiometric (O/Er = 1.5) with no evidence of detectable carbon contamination. Post-deposition annealing temperatures of 600–1000 ℃ are used for studies on the annealing behavior of the resulting ALD films; after annealing, changes in Er_2O_3 film structure, interfacial layer, and surface morphology are presented and discussed using a variety of analytical techniques. Further, electrical measurements of Er_2O_3 gate dielectrics on p-type Si before and after post-deposition annealing are carried out and the effect of annealing on the electrical properties of the dielectric is investigated.

4.1.2. Experimentation

Erbium oxide thin films were deposited using tris(methylcyclopentadienyl)erbium precursor and ozone as oxidant on Si(100) substrates in a horizontal hot wall tubular ALD reactor using a quartz tube 38 mm in diameter and 48 cm in length (Fig. 15). The reactor can be operated at a temperature up to 600 ℃ (custom-modified processing furnace, model 1043 Marshall, ThermCraft, Inc.) and typical depositions can be carried out at the temperature range of 25–450 ℃. The base pressure of the ALD reactor was less than 20 mTorr. The oxidant was mixture of ozone and oxygen (1000 ppm ozone)

generated with an oxygen (99.999% purity) flow through a UV lamp ozone generator immediately upstream of the deposition reactor. Argon (99.999% purity) was used as both carrier gas for the metal precursor and purging gas to clean the system between the delivery of precursor and oxidant. The precursor bubbler was kept at 95 ℃, and the delivery line section from the bubbler to the reactor was maintained 20–30 ℃ higher than the bubbler temperature in order to prevent condensation of the precursor during delivery. The depositions of Er_2O_3 films were carried out at a total pressure of 500 mTorr and in the temperature range of 100–400 ℃.

Er_2O_3 films were deposited on p-type Si(100) substrates (15 mm × 20 mm). Prior to deposition, substrates were cleaned with a 1:1:5 NH_4OH:H_2O_2:H_2O solution for 15 min to remove organic contaminants and particles, followed by 1% HF dip for 10 s. Each of the steps was followed by thorough deionized (DI) water rinse and drying by N_2 gas. This cleaning was found to leave ~0.5 nm (as measured by ellipsometry) of native oxide on the silicon substrate surface.

Thicknesses of as-deposited films were measured with a spectral ellipsometer (J.A. Woollam Co., Inc., model M44). Post-deposition annealing was carried out in a preheated quartz horizontal furnace (Lindberg Blue three-zone furnace) under N_2 atmosphere for 5 min between 600 and 1000 ℃ at 1 atm. Fourier transform infrared (FTIR) spectroscopy (Nicolet, Magna-IR 560) was used in the transmission mode over the wavelength range of 4000–400 cm^{-1}. A high resolution X-ray diffractometer (Philips X'pert) configured with 0.1542 nm X-ray emission line of Cu with bandwidth of 0.05 nm

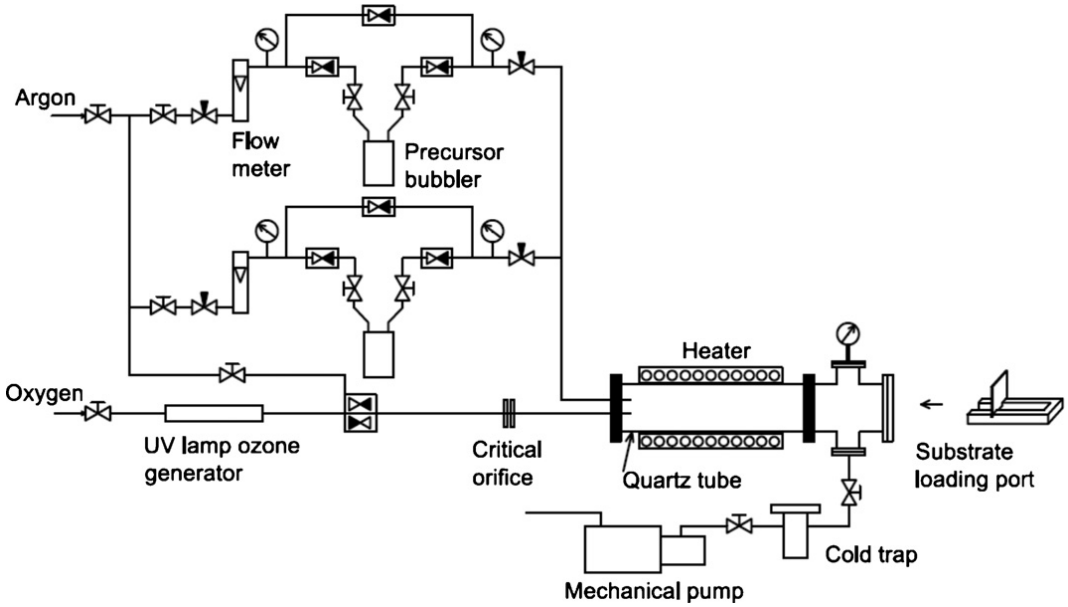

Figure 15. Schematic diagram of the ALD system used for the deposition of erbium oxide films on Si substrates from tris(methylcyclopentadienyl)erbium and ozone.

as the excitation source was used to obtain glancing incidence X-ray diffraction (GIXRD) diffractograms of ~30 nm-thick as-deposited and post annealed Er_2O_3 films at 600, 800 and 1000 ℃ in N_2 (99.999% purity) at 1 atm. GIXRD diffractograms were collected at an incident angle of 0.7 ° to enhance the diffraction sensitivity within the film and to avoid interference from the single crystal Si(100) substrate. The peaks were identified using the International Centre for Diffraction Data (ICDD) database of diffraction pattern Powder Diffraction Files (PDF). Chemical bonding and elemental analyses of Er_2O_3 films were probed with high resolution X-ray Photoelectron Spectroscopy (XPS) (Kratos Analyt-ical Ltd., Kratos AXIS-165) equipped with a monochromatic Al Kα (1486.6 eV) X-ray source operating at 15 kV and 10 mA. High res-olution spectra were collected at a take-off angle 90 ° with pass energy of 20 eV, step size of 0.1 eV, and dwell time of 200 ms. Surface morphology of as-deposited and post annealed thin films was studied using an optical surface profiler system (Veeco Instrument Inc., model Wyko NT3300) in the phase-shifting interferometry (PSI) mode with a vertical resolution of 0.1 nm. Current–voltage (I–V) and capacitance–voltage (C–V) characterizations were performed using an Agilent 4980 LCR meter equipped with a mercury probe station (Model 802 B, Materials Development Co.). The capacitors formed with the mercury probe had an area of 0.46 mm^2. The C–V characterizations were carried out at 10 kHz.

4.1.3. Results and discussion

A. ALD temperature window and growth rate of Er_2O_3 thin films

The thin film growth rate dependence on deposition temperature is shown in Fig. 16. The error bar shows less than 3% of thickness variation across the whole deposition

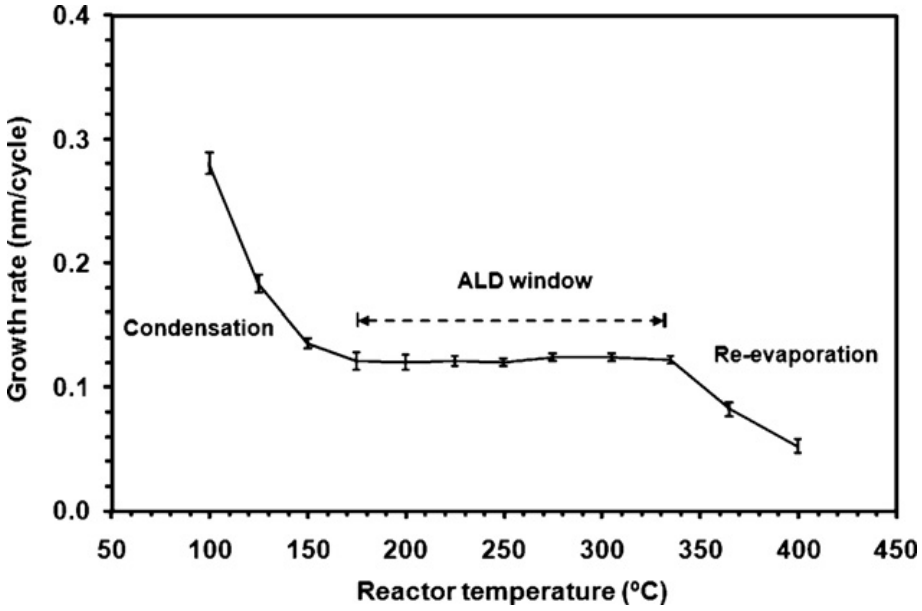

Figure 16. Er_2O_3 ALD rate as a function of reactor temperature. The vertical error bars indicate film uniformity across the sample. The bubbler temperature was 95 ℃. The system pressure was 0.5 Torr.

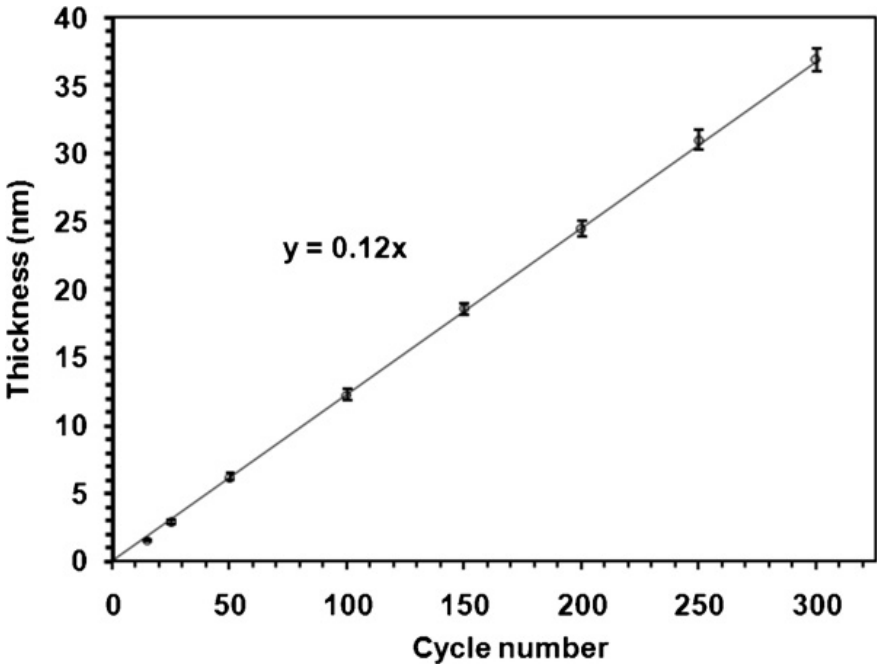

Figure 17. Number of cycles vs Er_2O_3 film thickness. Linear film growth with increasing number of ALD cycles is observed. The films were deposited at 250 ℃ and 0.5 Torr.

area. At the lower deposition temperature region of 100–170 ℃, a higher deposition rate that decreased with increasing deposition temperature was observed indicating a nonself-limiting film growth behavior because of likely precursor condensation on the substrate. Compared with other ALD Er_2O_3 studies that utilized different precursors [51, 102, 112], a wider ALD temperature window in the range of 170–330 ℃ was observed with a growth rate of 0.12 ± 0.01 nm/cycle. A decrease in the deposition rate is found at substrate temperatures higher than 330 ℃, and that is likely due to lower adsorption of $(CpMe)_3Er$ on the surface. Figure 17 shows the thickness of the as-deposited Er_2O_3 films measured after different number of cycles, i.e. from 15 to 300. From the slope of linear regression analysis of the data, the growth rate is found to be ~0.12 nm/cycle. In this case, the growth rate of Er_2O_3 is lower than that reported using $(CpMe)_3Er/H_2O$ [51], but much higher than that from other studies with different Er precursors, such as $Er(thd)_3$ or $Er(tBu_2amd)_3$ and ozone or oxygen plasma as the oxidant [102, 112, 117]. The self-limiting nature of ALD is also represented by the high degree of uniformity of the film thickness.

B. Fourier transform infrared spectroscopy studies

Figure 18 shows the FTIR transmission spectra of 15 nm-thick Er_2O_3 films as-deposited and subsequently annealed in N_2 at 600, 800, and 1000 ℃ for 5 min. Spectra were collected with 90 ° take-off angle. The IR spectra of the resulting films were obtained by substracting the substrate reference spectrum obtained from the Si(100) substrate after the cleaning process. As seen in Fig. 18, the spectrum of the as-deposited film shows small peaks at 440 and 600 cm^{-1} that can be assigned to phonon bands of

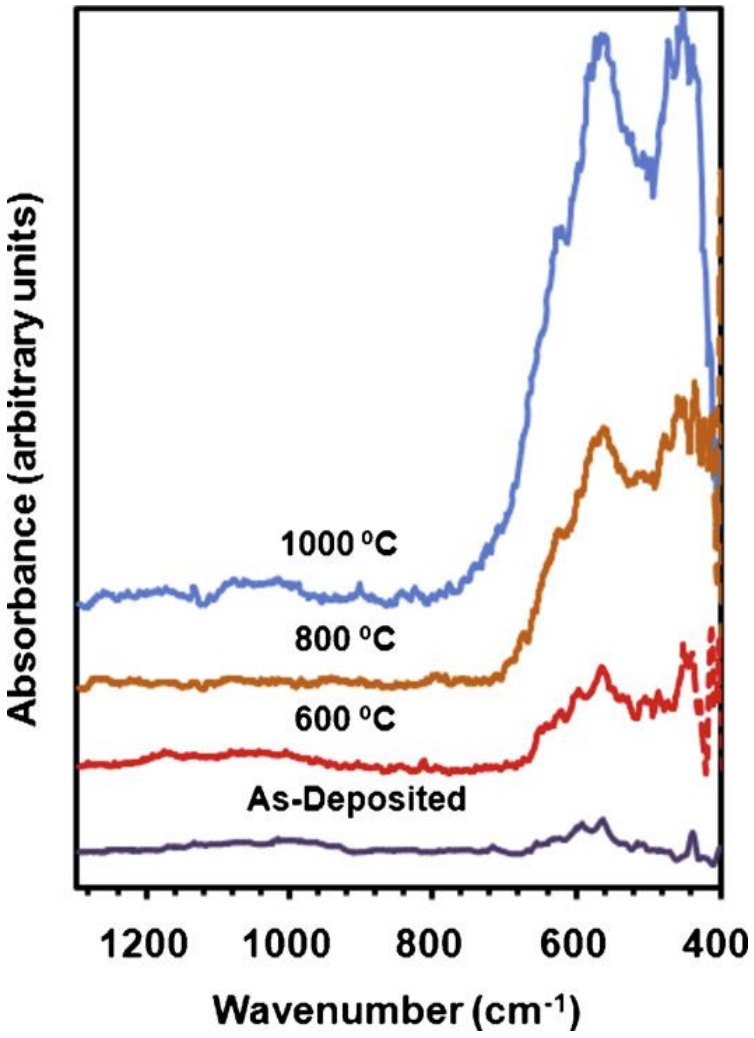

Figure 18. Transmission absorption FTIR spectra collected at 90 ° take-off angle to the normal of as-deposited Er_2O_3 and post-deposition annealed films at the indicated temperature for 5 min in N_2. The spectra are obtained after subtraction of background spectra obtained from cleaned Si substrate prior to deposition.

crystallized Er_2O_3 cubic phase [108, 118]. This suggests the onset of film crystallization under such deposition conditions, i.e. at 250 ℃. For the film annealed at 600 ℃, the appearance of sharper peaks at those low wave numbers (440 and 600 cm^{-1}) suggests more intense phonon bands of the cubic phase crystal structure of Er_2O_3. The intensity of the features in this region (400–650 cm^{-1}) increases with higher annealing temperature up to 1000 ℃, which is attributed to the increasing crystallinity of Er_2O_3 films. In the wave length region of 800–1000 cm^{-1}, a weak feature is observed (at ~900 cm^{-1}) for the film annealed at 1000 ℃ and this seems to be consistent with that reported by Ono and Katsumata [99] who attributed it to IR absorption of Si-O-Er bonds forming at a high annealing temperature. The absence of peaks in the 1300–3200 cm^{-1} region suggests that the carbon content in the films is below detectable level, which is corroborated by independent XPS studies (see later sections).

C. Chemical shifts and compositional analyses by XPS

a. XPS spectra of as-deposited films

Figure 19 shows high resolution XPS spectra of an as-deposited Er_2O_3 2 nm-thick film on silicon. It includes the core level spectra of Er 4d, O 1s, and Si 2p. The Er 4d spectrum (inset of Fig. 19(a)) was fitted with one Gaussian–Lorentzian distribution at 168.8 eV corresponding to Er^{3+}; this indicates that the film is composed of Er_2O_3 without formation of non-stoichiometric erbium oxide [119, 120]. The higher binding energy peak resulting from the chemical state of SiO_2 cannot be observed because of the overlap of the Si^{4+} and Er^{3+} auger peaks. The O 1s spectrum (Fig. 19(b)) could be deconvoluted into two symmetric peaks attributed to different chemical bonding states of the Er_2O_3/Si

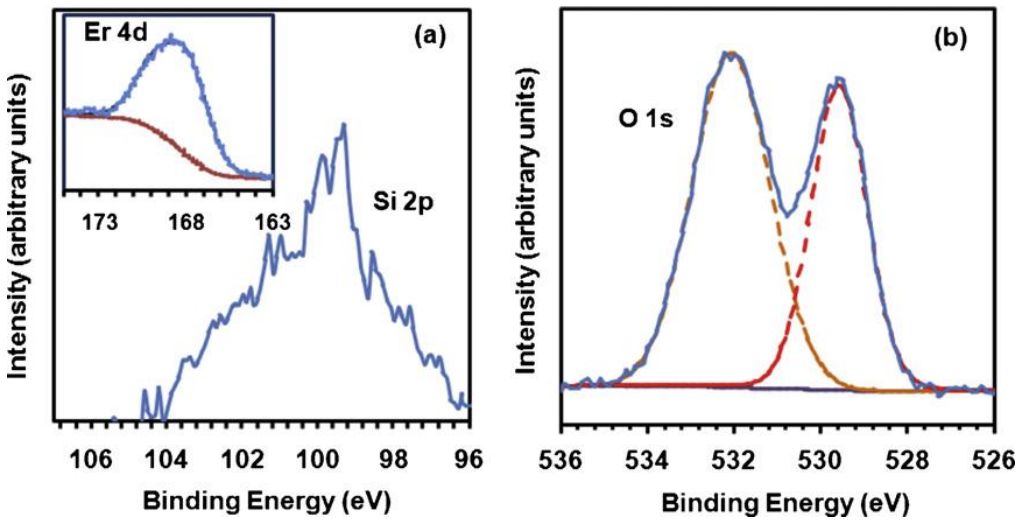

Figure 19. Core level Er 4d, Si 2p and O 1s XPS spectra of as-deposited Er_2O_3 film (2 nm-thick) collected at 90 ºtake-off angle. Er 4d and Si 2p XP spectra of as-deposited Er_2O_3 film (a) and O 1s features of as-deposited film (b). All ALD conditions are the same as those in Fig. 18.

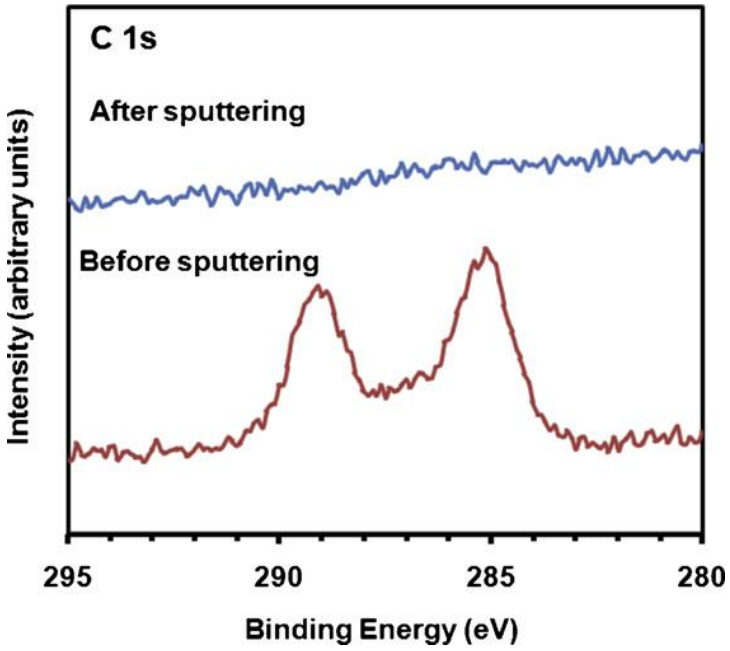

Figure 20. C 1s XP spectra of as-deposited Er_2O_3 films (30 nm-thick) collected at 90 ° take-off angle before and after sputtering using ~300 nA beam current argon ion gun for 10 min. Deposition conditions are the same as those in Fig. 18.

system. The low energy state centered at 529.7 eV is attributed to oxygen in Er_2O_3. The higher bonding energy state, at 532.2 eV, is assigned to Si-O bonds [119]. This also indicated that the interfacial layer consisted of silicon dioxide with-out formation of erbium silicate during the ALD.

Figure 20 shows the C 1s spectra of a 30 nm-thick Er_2O_3 film deposited on Si substrate. The spectra were collected before and after etching the film with Ar^+ beam in order to differentiate carbon on the surface from that in the bulk film. Before the removal of surface contaminants, the elemental ratios of O:Er:C are quantitatively determined to be 57.5:38.3:4.2 atom%. The ratio of O/Er corresponds to stoichiometric Er_2O_3, in contrast to the earlier ALD studies with different precursors [51, 102, 112]. After sputtering the surface using ~300 nA Ar^+ beam for 10 min, the amount of carbon is below detectable level, i.e. less than 0.5 atom%. Losurdo et al. reported that their MOCVD Er_2O_3 films resulting from $Er(CpiPr)_3$ and O_2 were close to the stoichiometric ratio [111]. However, studies on Er_2O_3 thin films deposited by e-beam evaporation and ALD were oxygen-rich (O/Er = 1.6–1.8) with carbon incorporation [51, 102, 112, 121]. This was likely due to the formation of $Er(OH)_3$ and $Er_2O_2CO_3$, the probable result of interactions between Er_2O_3 and moisture or carbon oxide [102, 108, 121].

b. XPS analyses of post-deposition annealed films

Figure 21(a) shows the changes in the core level spectra of Er 4d for 3 nm-thick Er_2O_3 films post-deposition annealed in N_2 at 600, 800 and 1000 ℃. The Er 4d peak is found to up shift as the annealing temperature increases from 600 to 1000 ℃. The Er 4d

spectrum of Er_2O_3 films annealed at 600 ℃ was similar to that of the as-deposited film (e.g. inset of Fig. 19(a)) and it could not be deconvoluted into more than one Gaussian–Lorentzian subordinate peak at 168.8 eV [120]. This suggests that films annealed at 600 ℃ consisted of unchanged Er_2O_3. For the film annealed at 800 ℃, the higher binding energy peak upon deconvolution resulted in an additional feature at 169.6 eV, which is attributed to the formation of $ErSiO_x$. Further, the spectrum of the sample annealed at 1000 ℃ showed increased intensity of the 169.6 eV peak, indicative of increased silicate formation; this is likely because the interdiffusion between the Er_2O_3 film and the interfacial SiO_2 during this annealing process.

Fig. 21(b) illustrates the core level O 1s XPS spectra for the same annealed 3 nm-thick Er_2O_3 films. O 1s spectra of the annealed films at 600 ℃ shows two peaks at 529.7 and 532.2 eV, assigned to Er_2O_3 (529.7 eV) and SiO_2 (532.2 eV). O 1s spectra of films annealed at 800 and 1000 ℃ could be deconvoluted into three Gaussian–Lorentzian subordinate peaks centered at 529.9 eV (Er-O), 531.4 eV (Er-O-Si) and 532.3 eV (Si-O), respectively, which are in agreement with the assignments of erbium oxide and silicate presented in Fig. 21(a) and discussed. At 1000 ℃, the intensity of the peaks at 529.9 eV and 532.3 eV decreases while the feature at 531.4 eV is seen to increase. The erbium silicate content is indeed found to increase during annealing from 800 to 1000 ℃, and the silicate peak becomes the dominant one; also, the O 1s spectral component assigned to Si-O down shifts from 532.2 to 531.9 eV, which also corroborates the increasing presence of erbium silicate. Increased silicate formation at 800 ℃ is consistent with an

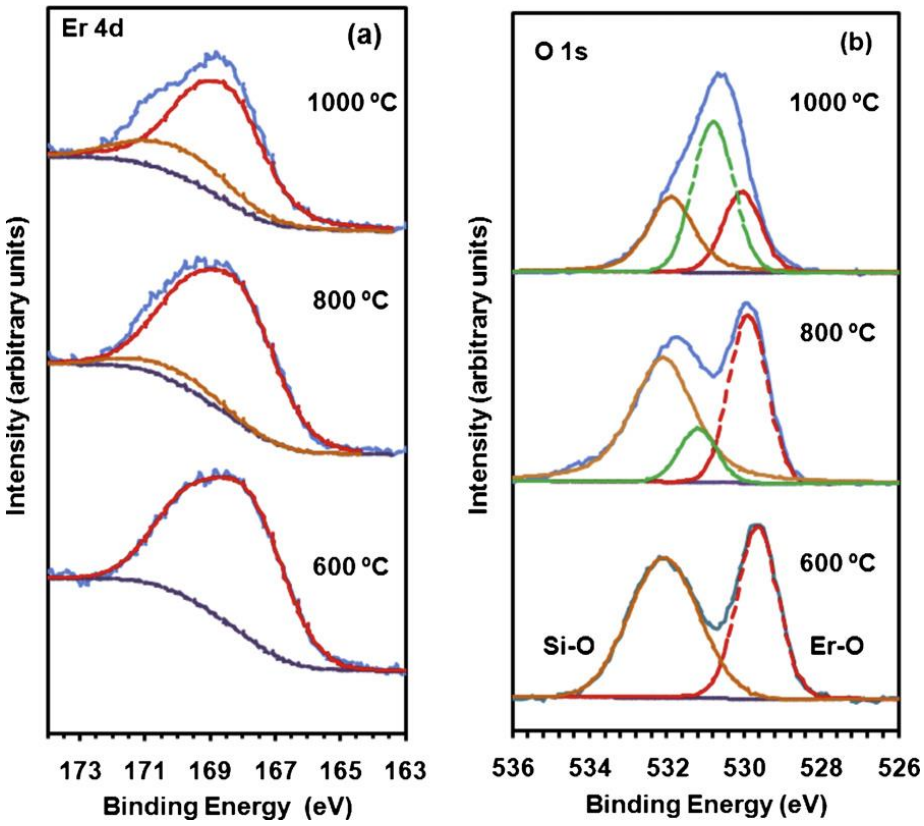

Figure 21. Er 4d core level (a) and O 1s XP (b) spectra of as-deposited Er_2O_3 (3 nm-thick collected at 90 ° take-off angle). The spectra are collected before and after post-deposition annealing in N_2 for 5 min at the temperature shown. All ALD conditions are the same with those in Fig. 18.

earlier XPS study of films deposited by physical evaporation [122]. However, Losurdo et al. reported that the onset temperature of formation of erbium silicate was 600 ℃ [111].

D. GIXRD studies of Er_2O_3 thin films

Figure 22 shows the GIXRD spectra of as-deposited Er_2O_3 films as well as films post-deposition annealed at 600, 800 and 1000 ℃ in N_2 for 5 min; the thickness of all films is 30 nm. The peak at 29.7 ° for the as-deposited films indicates the onset of film crystallization at the ALD conditions used, i.e. 250 ℃. Upon annealing, another two weak diffraction peaks at 34.2 and 49.1 °are observed when the annealing temperature is 800 ℃ or higher. The intensity of these cubic crystalline peaks increased with higher post-deposition annealing temperatures (up to 1000 ℃), suggesting increased crystallinity of the Er_2O_3 films. The major peaks have been identified to be in the cubic phase with the (222) orientation dominance (ICDD cards: 008-8242 and 26-0604) [51]. The average lattice constant (calibrated by Jade 9.0 software calculation of fitted peaks) is found to be about 1.047 nm for ALD Er_2O_3 films (as-deposited and annealed at temperatures between 600 and 1000 ℃) which is smaller than that of bulk Er_2O_3 (a = 1.055 nm). The grain sizes of the as-deposited and annealed films at 600, 800, and 1000 ℃ are 7.5, 8.2, 10.6 and 14.2 nm respectively, calculated by applying Scherrer's relation to the XRD (222), (400) and (440) peaks. In contrast, amorphous structure was found in earlier XRD studies of Er_2O_3 films deposited from different ALD precursors. For example, as-deposited Er_2O_3 films grown from $Er(thd)_3$ precursor at a temperature below 250 ℃ were reported to be amorphous with no observed diffraction peaks [112]. Paivasaari et al. reported that as-deposited Er_2O_3 films grown from $Er(tBu_2amd)_3$ precursor were also amorphous below 300 ℃ [102].

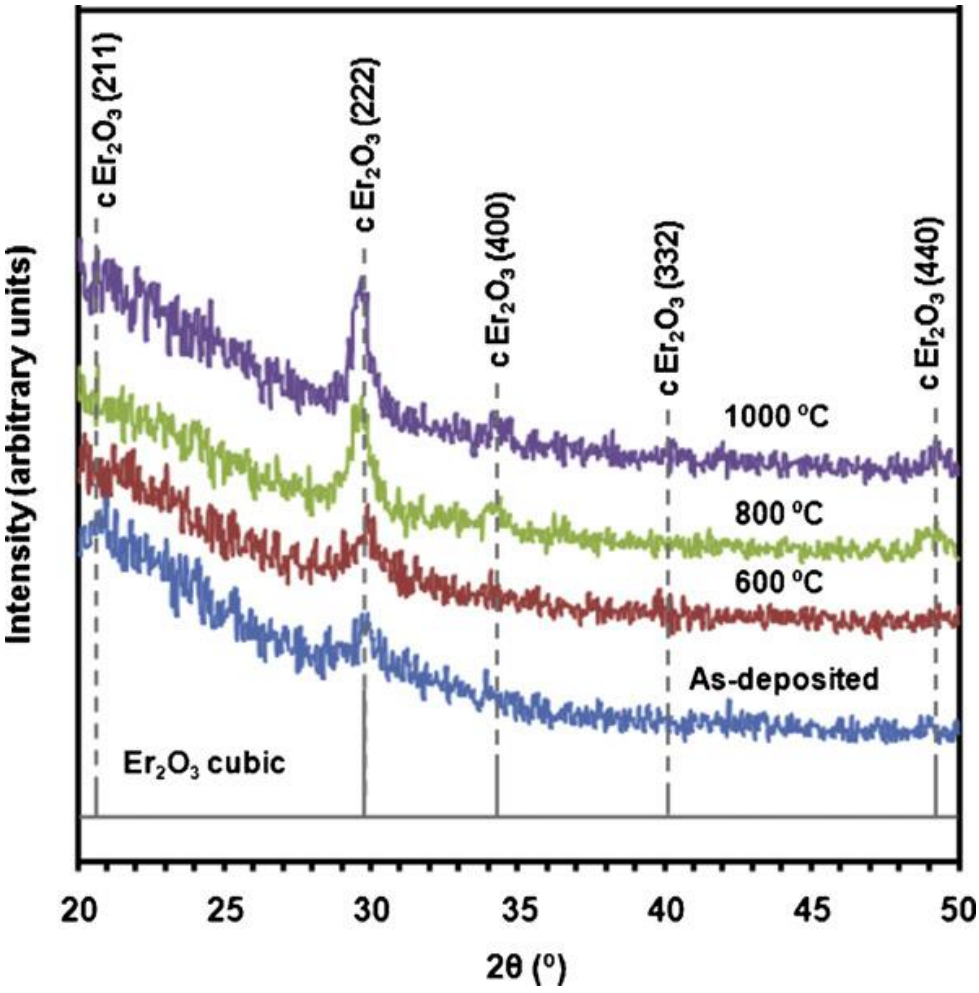

Figure 22. GIXRD of as-deposited and annealed Er_2O_3 films (30 nm-thick) at 600, 800 and 1000 ℃ in N_2 at 1 atm, for 5 min. The GIXRD analyses were carried out at a glancing angle of 0.7 º. Deposition conditions are the same as those in Fig. 18.

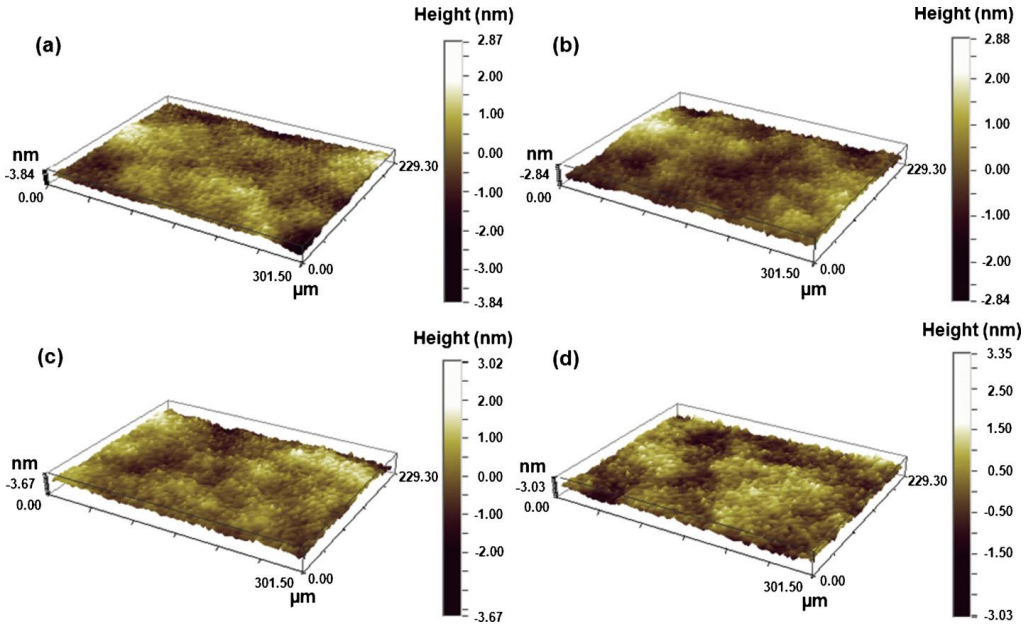

Figure 23. PSI images of Er_2O_3 30 nm-thick as-deposited films (a), and films annealed at 600 ℃ (b), 800 ℃ (c) and 1000 ℃ (d) in N2 at 1 atm. Film RMS roughness values are 0.71 (a), 0.75 (b), 0.85 (c) and 0.91 nm (d), respectively. Image size: 229.3 ×301.5 _m. Other film growth conditions are the same as those in Fig. 18.

E. Mapping of Er_2O_3 thin films using optical profilometry

The annealing effect on the surface morphology of 30 nm-thick Er_2O_3 films studied using the PSI mode of an optical surface profiler is shown in Fig. 23. As-deposited Er_2O_3 films have a smooth surface and a root-mean-square (RMS) roughness of 0.71 nm (Fig. 23(a)). The RMS roughness values of films annealed at 600, 800 and 1000 ℃ are found to be 0.75, 0.85 and 0.91 nm, respectively. The surface morphology and roughness is therefore found to barely increase from as-deposited to post annealed films in contrast with data reported in earlier related studies [102, 112]; this is likely because in those studies, post annealing could induce film crystallization from the amorphous structure of as-deposited films, while in our study, post annealing was found to enhance the crystallinity of as-deposited films that already had some crystallinity. It therefore indicates that the surface morphology/roughness can be more sensitive to phase transformation than to the enhancement of film crystallinity.

F. Electrical characteristics of Er_2O_3 thin films before and after post-deposition annealing

C–V measurements of Er_2O_3 thin films on p-type Si before and after post-deposition annealing were performed over the voltage range of −3 to +3 V in order to evaluate the effect of annealing on the dielectric film properties. Fig. 24 shows the C–V curves for Er_2O_3 films as-deposited and annealed at 600 ℃ in N_2. The relative permittivity of MOS devices was computed from the maximum capacitance observed in the accumulation region. The permittivity values of the overall MOS devices with Er_2O_3

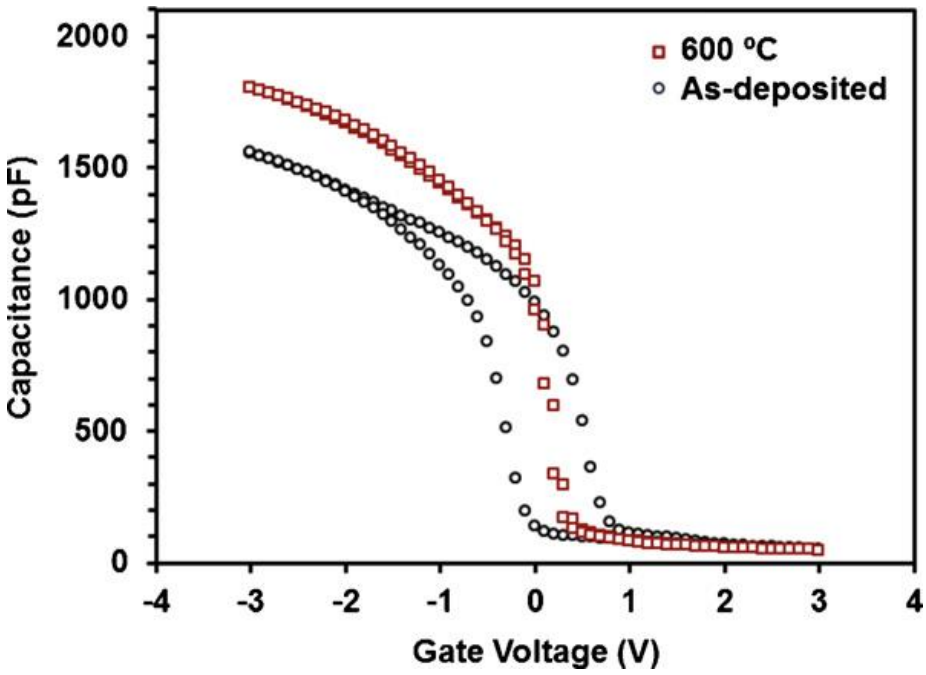

Figure 24. C–V curves measured in the rage of −3 to +3 V for a 29 nm-thick as-deposited Er_2O_3 dielectric and an annealed one at 600 ℃ in N_2 at 1 atm. The film growth conditions are the same as those in Fig. 18.

as-deposited and annealed at 600 ℃ were found to be about 9.8 and 11.8, respectively; the later value is higher than that of a sputtered Er_2O_3 film (i.e. 10.4) which was post-deposition annealed at 700 ℃ [50]. The C–V curve of as-deposited Er_2O_3 film shows a hysteresis voltage of 0.8 V at flatband voltage with a counterclockwise direction which was obtained by sweeping the voltage from inversion to accumulation region and back. The hysteresis voltage of an MOS capacitor is typically indicative of the presence of charges trapped in the resulting film, which might be related to oxygen vacancies or interstitial oxygen defects induced during the deposition process [123]. The as-deposited sample exhibits a flatband voltage (Vfb) of 0.66 V, which indicates negative charges trapped in the gate oxide. The C–V curve of a post-deposition annealed sample at 600 ℃ shows that the hysteresis voltage decreases significantly, i.e. to less than 50 mV. Such a small hystersis voltage and flatband voltage (0.3 V) suggests that the trapped negative charges and defects in the resulting gate oxide film were effectively reduced with the post-deposition annealing used. Compared with as-deposited films, the enhanced dielectric constant of Er_2O_3 films after annealing at 600 ℃ can be attributed to increased crystallinity, in agreement with the GIXRD results (Fig. 22).

I–V measurements of as-deposited Er_2O_3 films and films annealed at 600, 800, and 1000 ℃ were investigated in the range of −5 to +5 V and shown in Fig. 25. As it is seen, the I–V curve of as-deposited Er_2O_3 shows a low leakage current density of 10^{-8} Acm^{-2} measured at a gate bias voltage of 2 V. It has been reported that the I–V characteristics of gate oxide films are strongly depended on its conduction band offset to Si (3.5 eV) as well as its phase structure. Such a small leakage current of as-deposited

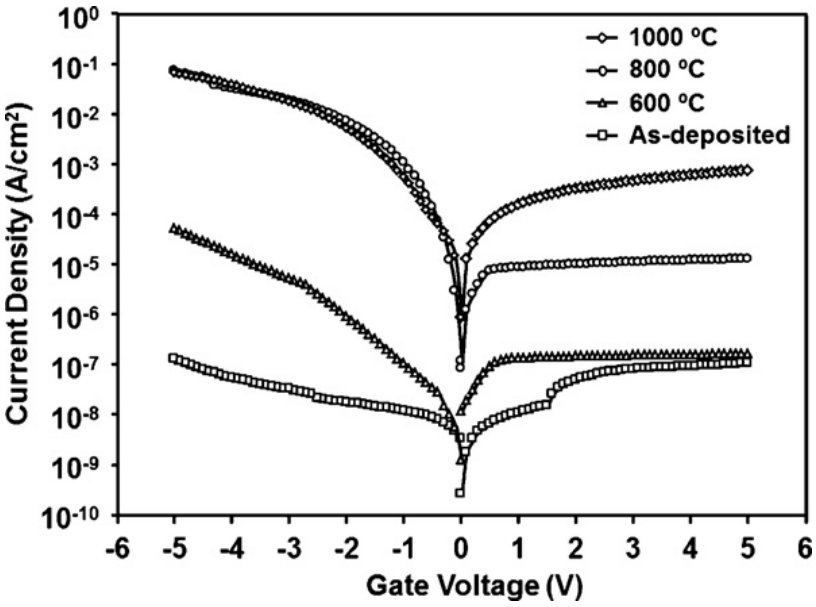

Figure 25. I–V curves measured in the range of −5 to +5 V for 29 nm-thick as-deposited Er_2O_3 dielectric and annealed ones at 600, 800, and 1000 ℃ in N_2 at 1 atm. The film growth conditions are the same as those in Fig. 18.

films was likely due to the mostly amorphous phase with only small intensity of crystalline peaks detected by GIXRD. For post-deposition annealed samples, the leakage current density measured at 3 V was found to continuously increase from 10^{-7} to 10^{-4} Acm^{-2} with increasing annealing temperature from 600 to 1000 ℃. The relatively higher leakage current density (10^{-5} Acm^{-2} at 3 V) measured after annealing at temperature at 800 ℃ was attributed to the presence of a larger amount of grain boundaries and leakage paths resulting from film crystallization, which is consistent with enhancements in film crystallinity as probed by GIXRD (Fig. 22). Therefore, post-deposition annealing carried out at a relatively low temperature, such as 600 ℃, is found to be an effective process for improving the electrical properties of Er_2O_3 MOS devices, which exhibits a small hysteresis voltage, less than 50 mV, a relatively high dielectric constant of 11.8 (κ_{SiO2} = 3.9), and a low leakage current density of 10^{-7} Acm^{-2} at 3 V (1 $MVcm^{-1}$).

4.1.4. Summary

Ultrathin Er_2O_3 dielectrics were deposited on p-type Si(100) substrates by atomic layer deposition using tris(methylcyclopentadienyl)erbium and ozone. The ALD temperature window for this process was found to be 170–330 ℃. The growth rate of Er_2O_3 with temperature-optimized ALD conditions was 0.12 nm/cycle. Elemental quantitative analysis of as-deposited Er_2O_3 films indicated the films were stoichiometric (O/Er = 1.5) with no evidence of detectable carbon contamination. Upon annealing in N_2 for 5 min, XPS results suggested that the formation of erbium silicate was initiated at an annealing temperature of 800 ℃ or higher and it was found to increase with increasing annealing temperature up to 1000 ℃. FTIR analyses of Er_2O_3 films annealed at 600 ℃

revealed sharper features corresponding to the cubic phase of Er_2O_3, and the intensity of the peaks increased with higher annealing temperature; this suggests increased film crystallinity with higher annealing temperatures in agreement with GIXRD results. The onset of film crystallization appeared in as-deposited films at the deposition temperature of 250 ℃ with an average lattice constant of 1.047 nm. Both as-deposited and annealed films exhibited smooth surfaces with rms values less than 1 nm; the surface morphology of Er_2O_3 films was found to become slightly rougher with increasing post-deposition annealing temperatures up to 1000 ℃. In addition, electrical characterizations of Er_2O_3 films showed that post-deposition annealing at 600 ℃ effectively improved the dielectric properties of Er_2O_3 MOS devices, which exhibited a small hysteresis of less than 50 mV, a relatively high dielectric constant of 11.8 (κ_{SiO2} = 3.9), and a low leakage current density of 10^{-7} Acm^{-2} at 3 V (1 $MVcm^{-1}$).

4.2. Atomic Layer Deposition and Characterization of Amorphous $Er_xTi_{1-x}O_y$ Dielectric Ultra-Thin Films

4.2.1. Introduction

Thin structures with high dielectric constant are one of the key components in the future fabrication of semiconductor devices, such as metal oxide semiconductor (MOS) transistors and dynamic random access memories (DRAMs) [12]. So far, a variety of high-κ candidates, including HfO_2, ZrO_2, La_2O_3, Y_2O_3, and TiO_2, have been proposed and investigated as replacements of conventional SiO_2 and SiON [12]. From these materials, TiO_2 has been considered to be one of the leading candidates in term of its high dielectric constant, 40 for amorphous or anatase structures and 80 or higher for rutile structure [45]. However, crystalline TiO_2 often suffers from severe leakage current density (~1 A/cm^2 at 1 V), because its polycrystalline structure induces a large amount of grain boundaries, which serve as high leakage and Si dopants (i.e., B or P) diffusion paths [11, 13, 45, 46]. In addition, structural transitions and multiphase crystalline TiO_2 yield variable electrical properties, such as uneven capacitance values and leakage current characteristics among different regions [13]. Therefore, stabilization of TiO_2 in its amorphous state throughout necessary thermal processes has been regarded as one of the challenges to achieve a high permittivity thin film without sacrificing its leakage current characteristics and reliability [45, 46].

An attractive approach to suppress crystallization of TiO_2 is doping it with other high-κ metal oxides, such as Al_2O_3, HfO_2 , ZrO_2, Ta_2O_5 and Ln_2O_3, forming thermally stable amorphous high-κ ternary oxides [45-49, 124]. For instance, a recent study of Al-

doped TiO_2 dielectric showed that the incorporation of Al could mostly result in amorphous ternary oxide throughout necessary annealing processes, thereby reducing the leakage current density of anatase TiO_2 (10^1 A/cm^2 at 0.16 MV/cm) on a TaN electrode [45]. However, it was reported that optimized $AlTiO_x$ dielectrics were found to be incompatible with Si electrodes and yielded a leakage current density of 10^{-4} A/cm^2 at 0.16 MV/cm [45]. Jeon et al. reported that addition of praseodymium into titanium oxide films using E-beam evaporation made it possible to achieve amorphous films with a dielectric constant of ~23 and a leakage current density of $\sim 10^{-5}$ A/cm^2 at −2 MV/cm on Si [49]. Among other lanthanide oxides, erbium oxide, as a novel high-κ candidate, is of particular interest due to its large conduction band offset to Si (3.5 eV), low leakage current density (10^{-8} A/cm^2 at 1 V), and a moderate dielectric constant (10-14) [50, 51]. In addition, studies of Er_2O_3 thin films showed a low fixed charge density and minimal interdiffusion between Er_2O_3 and Si substrate when used in metal-insulator-silicon (MIS) gate stacks [99]. Thus, Er_2O_3 could be a promising dopant of TiO_2 films, especially for the reduction in leakage current density by several orders of magnitude.

A challenge in the implementation of amorphous Ln-doped TiO_2 dielectric films is the development of a suitable route for thin film deposition; a few techniques such as co-precipitation [125], E-beam evaporation [49], and magnetron sputtering have been applied [126]. In cutting-edge micro/nanoelectronics fabrication, atomic layer deposition has been identified as one of the preferred means of fabricating nanoscale features in the semiconductor industry, because it offers distinct advantages and meets demanding requirements such as precise thickness control at the required dimensions within MOS

devices and conformal coverage in the deep trenches of memory cells [38]. In addition, ALD may enable composition tunability in the resulting materials, especially for ternary materials, which is important in determining structural, thermal and electrical properties of resulting dielectric films.

In this study, we report on the doping of TiO_2 with Er_2O_3 using ALD to form Si-compatible amorphous $Er_xTi_{1-x}O_y$ dielectrics with tunable content of Er. Tris(methylcyclopentadienyl)erbium [$(CpMe)_3Er$] and tetrakis(diethylamino) titanium [TDEAT] are used in the deposition of these films. $Er_xTi_{1-x}O_y$ films are analyzed and discussed in terms of impurity level, interfacial layer, structure, and surface morphology in order to investigate the effect of Er incorporation on the properties of as-deposited and post-deposition rapid thermal processing (RTP)-treated films. Furthermore, electrical measurements on $Er_xTi_{1-x}O_y$ films are performed before and after RTP treatment in order to develop optimized Si-compatible $Er_xTi_{1-x}O_y$ dielectrics with ultra-low leakage current, negligible hysteresis voltage, and high permittivity. After RTP treatment, the leakage current density of $Er_xTi_{1-x}O_y$ dielectrics on Si (10^{-8} A/cm^2 at −1 MV/cm), for example, is found to be superior to those reported for amorphous thin dielectrics, such as $AlTiO_x$ (125 nm)/Al_2O_3 (4 nm) (J = 10^{-4} A/cm^2 on Si or 10^{-7} A/cm^2 on TaN at 0.16 MV/cm) [45], TaTiO (J=10^{-3} A/cm^2 at 1 MV/cm on TiN),9 and $Zr_xTi_yO_2$ (J = 10^{-5} A/cm^2 at 1 MV/cm on RuO_2) [46].

4.2.2. Experimentation

$Er_xTi_{1-x}O_y$ thin films made use of $(CpMe)_3Er$ and TDEAT as metal precursors and ozone as oxidant (1000 ppm ozone in oxygen). Prior to deposition, Si (15mm×20 mm) samples were cleaned with the Radio Corporation of America (RCA) standard cleaning (SC-1) procedure to remove organic contaminants, followed by a 1% hydrofluoric acid dip for 20 s to reduce native oxide down to ~0.6 nm on Si surface. Each of these two steps was followed by thorough deionized water rinse and drying in N_2. After cleaning, Si substrates were immediately loaded into a custom designed hot wall ALD reactor for deposition. Both metal precursors were kept in stainless steel bubblers; during deposition, the $(CpMe)_3Er$ bubbler was maintained at 100 ℃ and the TDEAT one at 65 ℃.

Film thickness was measured with a spectral ellipsometer (Model M-44, J. A. Woollam Co.); for each thickness determination, three measurements across the entire deposition area were carried out with mean values representing film thickness and standard deviation indicating thickness variation. Chemical bonding states of $Er_xTi_{1-x}O_y$ films were probed with a high resolution XPS (Kratos AXIS-165, Kratos Analytical Ltd.) equipped with a monochromatic Al Kα (1486.6 eV) X-ray source operating at 15 kV and 10 mA. High resolution XPS spectra of the elements-of-interest were collected using pass energy of 20 eV, step size of 0.1 eV, and dwell time of 200 ms.

The Carbon 1s line at 285 eV was used to calibrate the binding energy scale of the XPS spectra. The analyses of $Er_xTi_{1-x}O_y$ films were performed through XPS spectral peak-fitting, where peaks were subtracted from Shirley-type backgrounds and

deconvoluted using Gaussian-Lorentzian peak shape functions. For studies on thermally induced changes at the interface, surface roughness, and electrical properties, the ALD films were annealed in an RTP furnace (RTP-600S, Modular Process Technology Co.) at 700 ℃ for 30 s in O_2 at 1 atm. The bulk composition of the resulting films was investigated using Rutherford back scattering (RBS) spectroscopy with a general ionex tandetron accelerator (Model 5510, General Ionex Co.) employing 2 MeV He^+ particles. An X-ray diffractometer (X'pert, PANalytical B.N. Co.) was used to obtain glancing incidence X-ray diffraction (GIXRD) patterns of as-deposited and RTP-treated films. The overall diffraction angle (2θ) resolution was 0.15 º. GIXRD diffractograms were collected at an incident angle of 1 º to enhance diffraction sensitivity within the film and to minimize interference from the single crystal Si (100) substrate. The crystalline features were identified using the International Center for Diffraction Data (ICDD) database of diffraction pattern Powder Diffraction Files (PDF).

4.2.3. Results and Discussion

A. ALD temperature window and growth of $Er_xTi_{1-x}O_y$ films

A sufficient overlap of ALD temperature windows of the constituent binary processes is desirable for the ALD of ternary thin films; this overlap could effectively improve the reproducibility of the ternary film growth. Figure 26 shows the temperature dependence of growth rates of both Er_2O_3 and TiO_2. At low temperatures, high growth rates that decrease with increasing substrate temperature were observed for both oxide thin films; these growth rates indicate a non self-limiting growth behavior likely resulting from multilayer condensation of the precursor during precursor pulsing. At high

temperatures, the low growth rates of Er_2O_3 could be attributed to lower adsorption of $(CpMe)_3Er$ on the reaction surface, whereas the rapid increase in the growth rate of TiO_2 was attributed to thermal decomposition of TDEAT at temperature higher than 250 ℃ [78]. The region where the growth rate is found to be independent of deposition temperature is taken as the ALD temperature window for each oxide process. In this system, a sufficiently overlapping temperature window of the binary oxide processes was found to be between 175 and 250 ℃; this common window offers a suitable temperature range for depositing $Er_xTi_{1-x}O_y$ films. Therefore, the deposition temperature of each metal oxide as well as of $Er_xTi_{1-x}O_y$ composite films in this study was maintained at 245 ℃.

Figure 27 shows the dependence of Er_2O_3, TiO_2, and $Er_xTi_{1-x}O_y$ films thicknesses on the total number of ALD cycles, and this dependence corroborates the precise thickness control of self-limiting ALD processes. For the ALD of each single-component oxide, linear regression analyses yield growth rates of 0.12 nm/cycle for Er_2O_3 and 0.047 nm/cycle for TiO_2. The growth rate of Er_2O_3 is found to be at least two times higher than that in earlier ALD studies using $Er(thd)_3$ and $Er(tBu_2amd)_3$ with O_3 as oxidant [102, 112]. On the other hand, the growth rate of TiO_2 is slightly lower than that obtained in our earlier study using the same precursor and moisture as oxidant in a different ALD system [48], but higher than that reported with other titanium precursors such as titanium isopropoxide (TTIP) and $TiCl_4$, using water or even oxygen plasma as oxidant [127, 128]. Such findings suggest relatively high reactivity of TDEAT with oxidants (i.e., H_2O or O_3) on silicon in our ALD reactors.

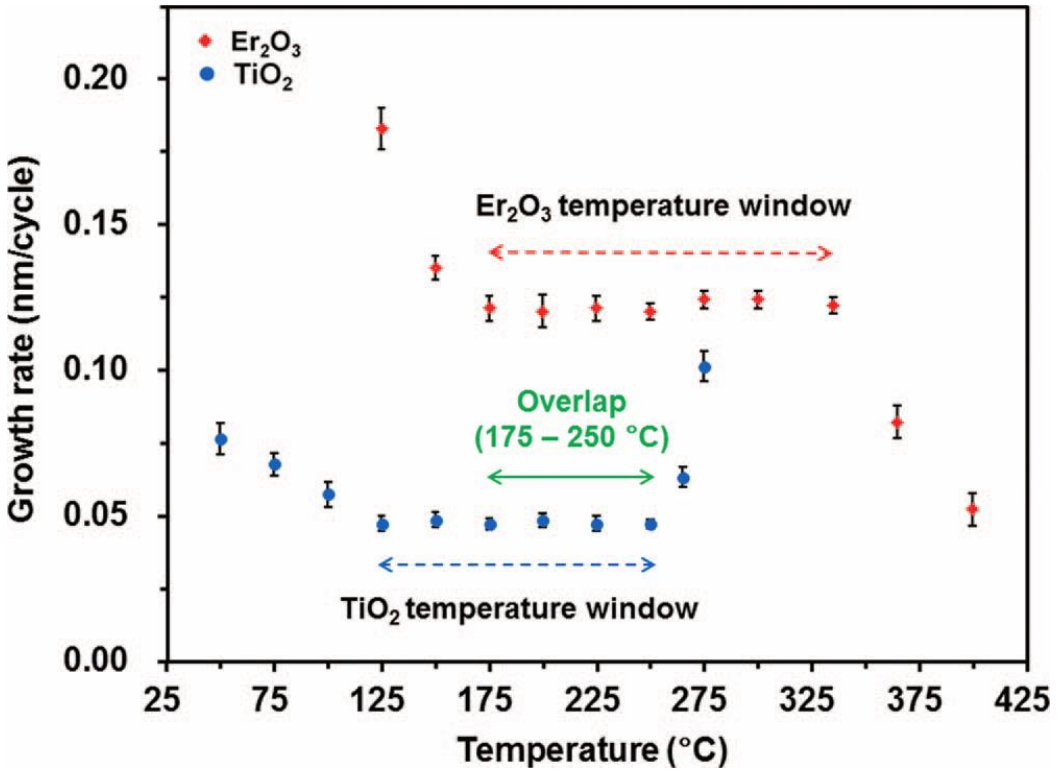

Figure 26. Dependence of growth rates of Er_2O_3 and TiO_2 films on ALD reactor temperature. The Er and Ti precursors were kept at 100 and 65 ℃, respectively. The error bars indicate film uniformity across the sample.

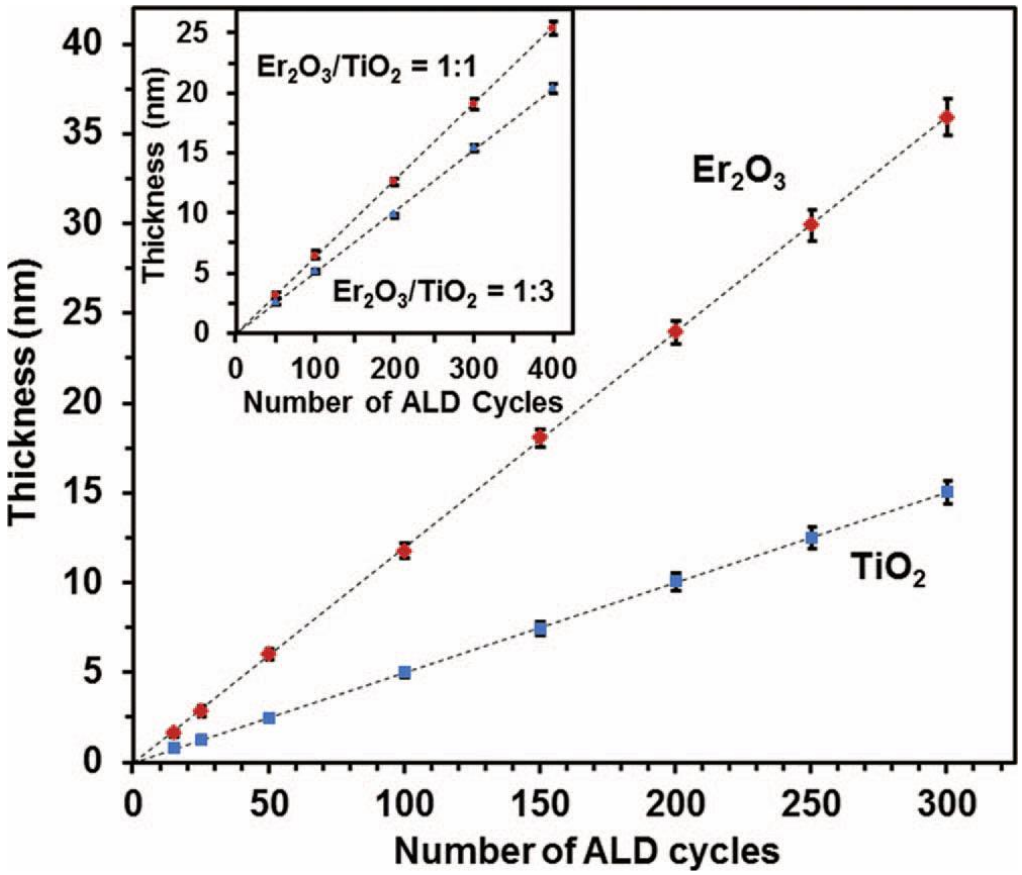

Figure 27. Thicknesses of Er_2O_3 and TiO_2 films as functions of ALD cycle number (main). Thicknesses of $Er_xTi_{1-x}O_y$ films with ALDCR (i.e., Er_2O_3:TiO_2) of 1:1 and 1:3 are shown as a function of the number of cycles in the inset. All films were deposited at 245 ℃. Other ALD conditions were the same as those in Fig. 26.

The growth of $Er_xTi_{1-x}O_y$ films shows a linear dependence of the film thickness on the number of ALD cycles (inset of Fig. 27). Moreover, the average growth rate is seen to increase with the ALD cycle ratio (ALDCR) of Er_2O_3/TiO_2; $Er_xTi_{1-x}O_y$ films with ALDCR of 1:3 and 1:1 yield growth rates of 0.051 and 0.064 nm/cycle, respectively. The self-limiting feature of the ALD processes in this work is also represented by the high degree of uniformity of Er_2O_3, TiO_2, and $Er_xTi_{1-x}O_y$ film thicknesses across the entire deposition area (Fig. 27).

B. Composition tunability - impurities

In order to study composition tunability of the atomic layer deposited $Er_xTi_{1-x}O_y$ films, a series of depositions was carried out with different ALD cycle ratios. For example, for a normalized cycle ratio $[Er_2O_3/(TiO_2+Er_2O_3)]$ of 0.2, one cycle of Er_2O_3 deposition alternated with four cycles of TiO_2 deposition. Figure 28 shows the effect of normalized cycle ratio $[Er_2O_3/(TiO_2+Er_2O_3)]$ on atomic composition [Er/(Ti+Er)] of 34 nm-thick as-deposited $Er_xTi_{1-x}O_y$ films, as determined from quantitative analyses of RBS spectra. The atomic ratio of Er/(Ti+Er) in $Er_xTi_{1-x}O_y$ films is found to monotonically increase almost linearly with increasing normalized cycle ratio $[Er_2O_3/(TiO_2+Er_2O_3)]$. This shows that the Er content in the resulting films can be effectively controlled by varying the ALDCR of Er_2O_3 and TiO_2. Similar effective atomic composition tunability was also reported in earlier studies with the ALD of other composite metal oxides, such as Y_2O_3-doped HfO_2 and HfO_2-doped TiO_2 [48, 129].

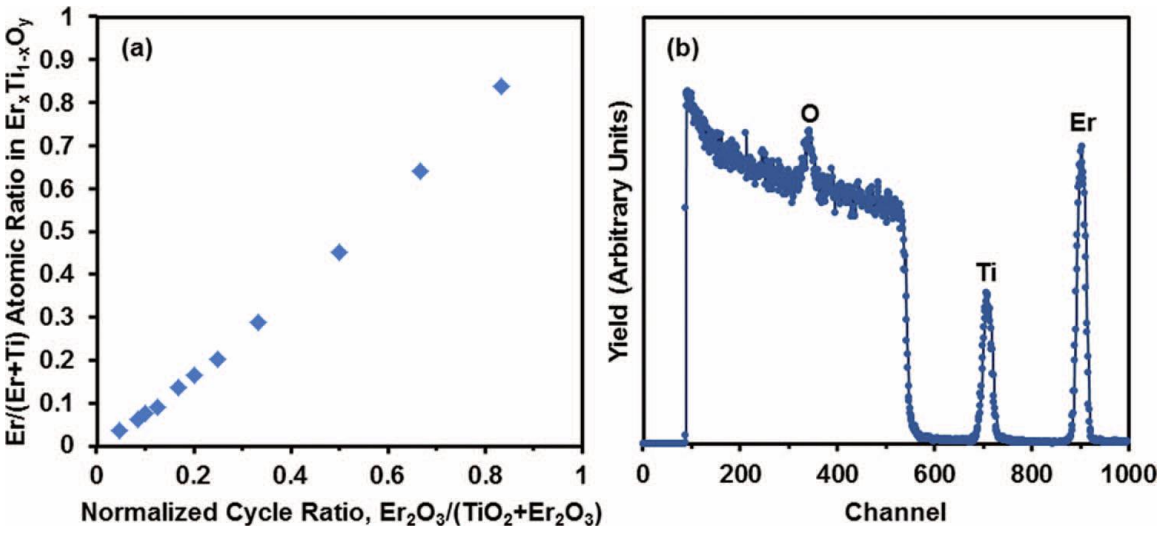

Figure 28. (a) $Er_xTi_{1-x}O_y$ (34 nm-thick) film composition evaluated using RBS as a function of normalized cycle ratio of $Er_2O_3/(Er_2O_3+TiO_2)$. (b) RBS spectrum of as-deposited $Er_xTi_{1-x}O_y$ film with an ALDCR of 1:3. Other ALD conditions were the same as those in Fig. 27.

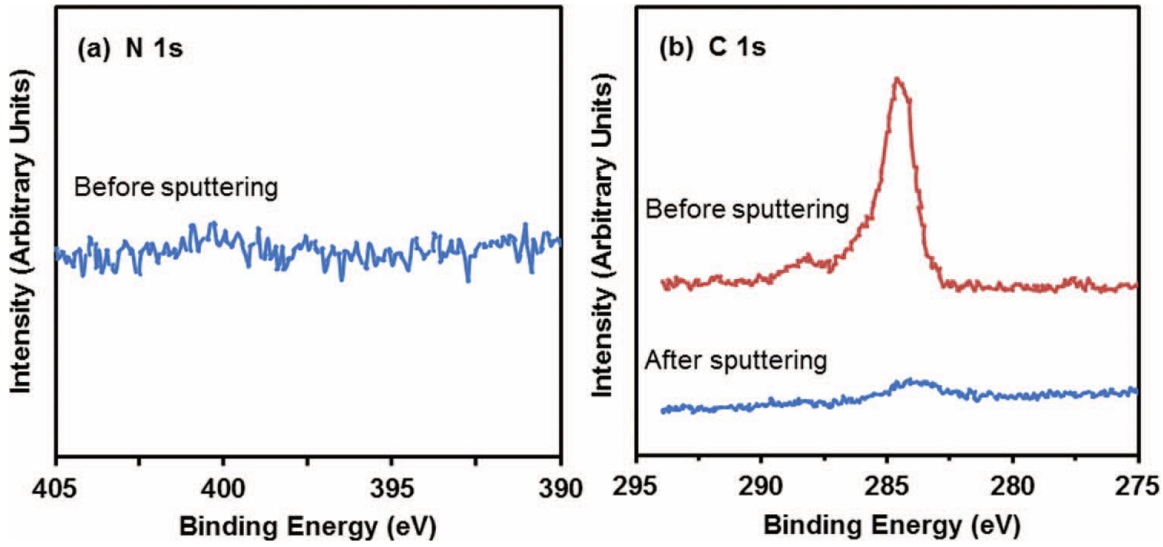

Figure 29. N 1s and C 1s XP spectra of $Er_xTi_{1-x}O_y$ film with an ALD cycle ratio of Er_2O_3/TiO_2 = 1:3. XP spectra were collected at 90 ºtake-off angle. C 1s spectra were collected before and after sputtering the surface using ~200 nA Ar+ beam for 10 min. Other ALD conditions were the same as those in Fig. 27.

For MOS and memory applications, impurities (e.g., C or Cl) in gate dielectric films are undesirable; they can be incorporated during deposition and often cause degradation of electrical performance, especially because of increased electronic trap centers and defects [130]. Also, itwas reported that carbon contamination could notably increase crystallization temperature of oxide films [124]. The impurity content of as-deposited films can be generally minimized with optimization of deposition conditions used, such as deposition temperature, operating pressure, and nature of precursor(s). Therefore, it is necessary to investigate the level of impurities in $Er_xTi_{1-x}O_y$ films formed with TDEAT/O_3 and $(CpMe)_3Er/O_3$ in our ALD studies. Figure 28b shows an RBS spectrum from a 34 nm-thick $Er_xTi_{1-x}O_y$ film with ALDCR of 1:3. The RBS reveals that there is no detectable nitrogen and carbon contamination in the film, which is corroborated by surface-sensitive XPS analyses (Fig. 29). No peaks are observed in the XPS spectrum of N 1s (Fig. 29a). After sputtering the film surface with ~200 nA Ar^+ beam for 10 min, the amount of surface carbon contamination seems to be at the XPS detection limit, i.e., less than 0.5 atom% (Fig. 29b). Such a low impurity level is in agreement with earlier studies of atomic layer deposited Er_2O_3 and chemical vapor deposited TiO_2 using $(CpMe)_3Er/H_2O$ and TDEAT/O_2 processes, respectively [51, 124].

C. <u>$Er_xTi_{1-x}O_y$/Si interface</u>

The XPS spectra of 3.5 nm-thick $Er_xTi_{1-x}O_y$ films with ALDCR of 1:3 are shown in Fig. 30. The XPS spectra were collected at a take-off angle of 90 ° in order to obtain information about the $Er_xTi_{1-x}O_y$ /Si interfacial region. The $Er_xTi_{1-x}O_y$ films deposited with different ALD cycle ratios generally have similar peak shapes and locations of the

XPS spectral features. The Er 4d core-level spectra of as-deposited and RTP-treated $Er_xTi_{1-x}O_y$ films show the same dominant feature centered at 168.8 eV (Fig. 30a), corresponding to the signature peak of Er_3^+ [50]. The small feature at the higher binding energy is attributed to the formation of Er silicate at the interface during deposition. Peaks indicative of erbium silicide at the lower binding energy of 168 eV are not observed. The Ti 2p core-level spectra of $Er_xTi_{1-x}O_y$ films before and after post-deposition RTP consist of two peaks assigned to Ti $2p_{1/2}$ and Ti $2p_{3/2}$ (Fig. 30b), in agreement with the oxidation state of Ti_4^+ [48]. No feature is found at lower binding energies than 453.9 eV; therefore, no titanium silicide is formed.

In order to further analyze the effect of post-deposition RTP on the $Er_xTi_{1-x}O_y$/Si interface, O 1s and Si 2p core-level spectra of as-deposited and RTP-treated films are shown in Figs. 30c and 30d, respectively. The O 1s spectrum of the as-deposited film (Fig. 30c, bottom) could be deconvoluted into three peaks, which are attributed to different chemical bonding states of the $Er_xTi_{1-x}O_y$/Si system: the dominant one at 530.3 eV is consistent with an M-O-M binding state (M refers to Er or Ti), while the two shoulder peaks located at 531.2 and 532.4 eV are assigned to M-O-Si and O-Si binding states of silicate and SiO_2, respectively [48]. Therefore, after ALD, the species at the $Er_xTi_{1-x}O_y$/Si interface seems to be silicate and SiO_2. Following the RTP treatment at 700 ℃, the O-Si peak at 532.4 eV is found to increase in intensity (Fig. 30c), which suggests increased formation of SiO_2 at the interface. This finding is corroborated by analyses of the Si 2p spectra (Fig. 30d) that show two main peaks at the binding energies of 99.3 and 99.8 eV

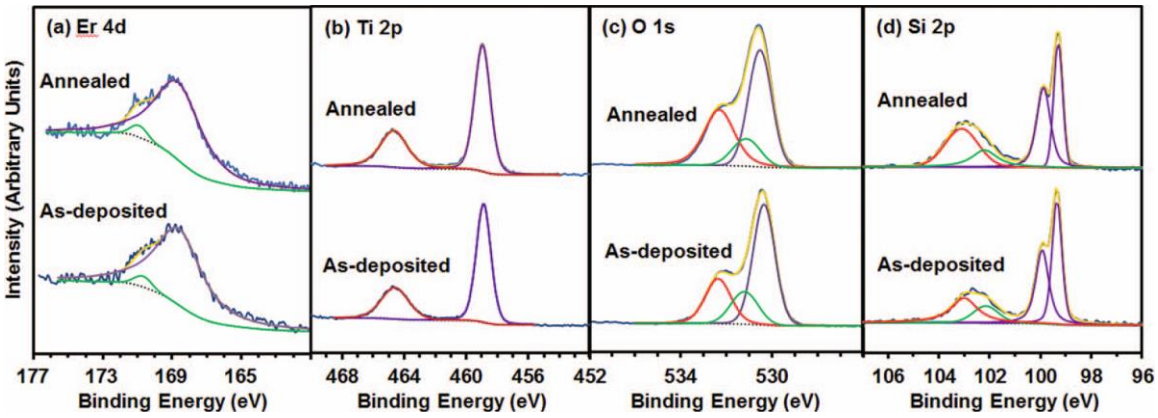

Figure 30. Er 4d (a), Ti 2p (b), O 1s (c), and Si 2p (d) core level XP spectra of as-deposited and RTP-treated 3.5 nm-thick $Er_xTi_{1-x}O_y$ films with ALDCR of 1:3. The film was rapid thermal annealed at 700 ℃ in O_2 for 30 s. Other ALD conditions were the same as those in Fig. 27.

(attributed to the Si substrate) along with two features at 102.2 and 103.1 eV assigned to silicate and SiO_2, respectively [48]. The Si 2p spectra show that the SiO_2 peak intensity of the RTP-treated film is higher than that of the as-deposited film, in agreement with increased formation of SiO_2 at the $Er_xTi_{1-x}O_y$/Si interface after the post-deposition RTP used.

D. Effect of rapid thermal processing on the $Er_xTi_{1-x}O_y$ film structure

The structure of dielectric films is important in determining their electrical characteristics, especially leakage current density. For example, Kwon et al. reported TiO_2 film suffers from serious leakage current (~0.1 A/cm^2 at 1 V) after post-deposition annealing at 500 ℃, which was attributed to a large amount of grain boundaries induced by film crystallization [46]. In the present study, structures of TiO_2 and $Er_xTi_{1-x}O_y$ films before and after post-deposition RTP were investigated using GIXRD (Fig. 31). All films were 34 nm-thick as measured with spectroscopic ellipsometry. The corresponding lattice structures of diffraction peaks were identified and labeled as indicated in Fig. 31.

As-deposited TiO_2 films show a trace presence of a diffraction feature at 25°, which corresponds to anatase (101) and therefore suggests onset of TiO_2 film crystallization at the deposition temperature of 245 ℃. A similar onset of TiO_2 crystallization temperature in the anatase phase was observed and reported in an earlier ALD study utilizing the $Ti[OCH(CH_3)_2]_4/H_2O$ process on Si substrates [131]. On the other hand, the pure amorphous structure of TiO_2 film deposited at a lower temperature (i.e., 200 ℃) was obtained in our earlier study using TDEAT with moisture as oxidant,

and that work indeed suggested a higher onset crystallization temperature than 200 ℃ for TiO_2 on Si [48]. After RTP at 700 ℃ in O_2, a sharp increase of the diffraction peak of TiO_2 (101) at 25 ° was observed (Fig. 31) along with the appearance of features at 48.1, 53.9, and 55 ° that were assigned to (200), (105), and (211), respectively; these are indicative of anatase TiO_2. The absence of rutile peaks in the XRD pattern suggests no phase transition to rutile during the post-deposition RTP used. This is in agreement with earlier studies on TiO_2 films grown with TDEAT/H_2O or TTIP/H_2O ALD processes and annealed in N_2 [48, 131], but it is in contrast to the presence of the TiO_2 rutile phase in films deposited from the TDEAT/O_2 chemical vapor deposition (CVD) process followed by post-deposition annealing at the same temperature in Ar [124].

All as-deposited Er-doped TiO_2 films with the ALDCR used were found to be amorphous, since no features were found in their diffraction patterns (not shown). After the post-deposition RTP, a weak diffraction pattern corresponding to the anatase structure emerges in the resulting $Er_xTi_{1-x}O_y$ film deposited with ALDCR of 1:12 (Fig. 31 main), representing a likely onset of crystallization under the annealing condition used. On the contrary, RTP-treated $Er_xTi_{1-x}O_y$ films deposited with ALDCR of 1:8, 1:5, 1:3, and 1:1 remain amorphous (Fig. 31 inset), and this result is attributed to the breaking of the originally crystalline structure of TiO_2 due to a sufficient dosage of Er. Similar annealing behavior of amorphous ternary gate oxides was observed in previous ALD studies of Hf-doped TiO_2, Zr-doped TiO_2, and Al-doped TiO_2 films [46, 48, 124]. Such a good thermal stability in amorphous structure is mostly attributed to the incorporation of ions with radii much larger or smaller than Ti, and the impurity atoms could significantly distort the

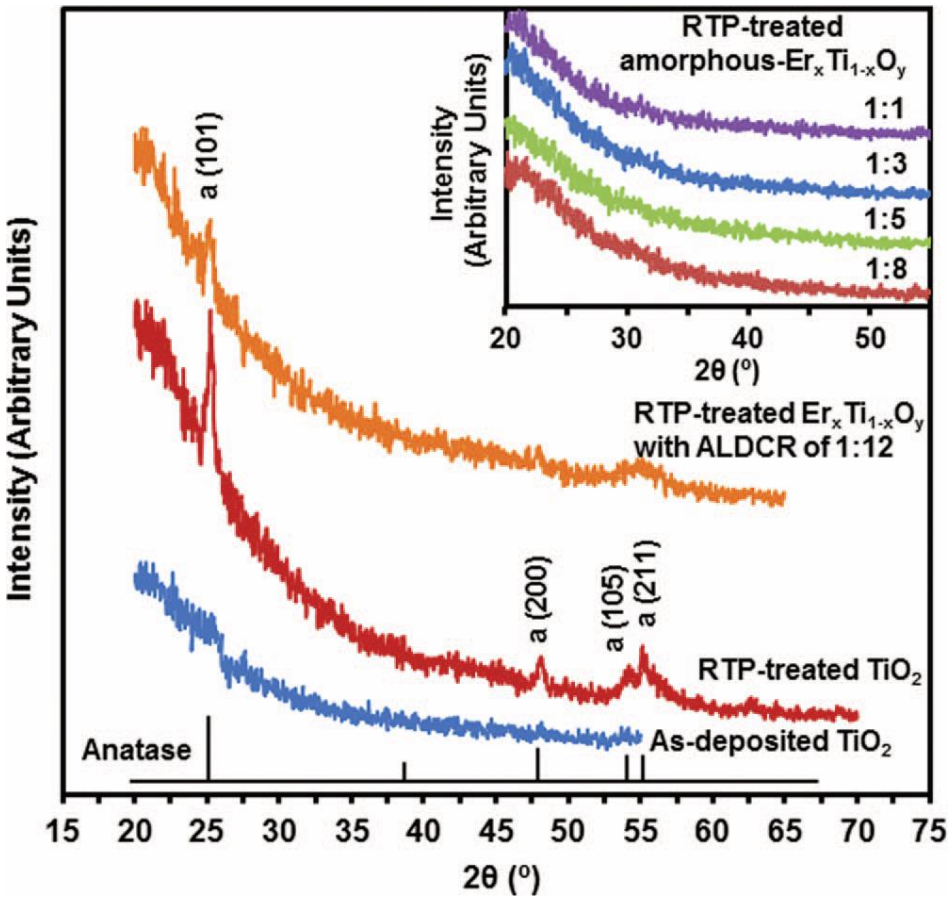

Figure 31. GIXRD patterns of as-deposited and RTP-treated TiO_2 films as well as of RTP-treated $Er_xTi_{1-x}O_y$ with ALDCR of 1:12 (main); diffractograms of RTP-treated amorphous $Er_xTi_{1-x}O_y$ films with ALDCR of 1:8 or higher (inset). GIXRD characterizations were collected at an incident angle of 1º. All deposition and RTP treatment conditions were the same with those in Fig. 30. Anatase TiO_2 reference: PDF Card No. 00-021-1272.

original TiO_2 structure and enhance the entropy for the crystallization process.

E. Surface morphology and roughness

The surface morphology and roughness of dielectric films are significant for CMOS applications, for example, because uneven surface morphology could lead to variable electrical properties at different regions [13]. Also, changes in surface roughness often reveal changes in the underlying structure [48]. In this study, the surface roughness of films was investigated using the PSI mode of an optical surface profiler. Figure 32a shows the root-mean-square (rms) roughness of 34 nm-thick TiO_2 and $Er_xTi_{1-x}O_y$ films for various ALDCR measured before and after RTP at 700 ℃ in O_2. For as-deposited films, all $Er_xTi_{1-x}O_y$ films are found to have rms roughness of ~0.4 nm. The TiO_2 film shows a higher rms roughness of ~0.6 nm, which coincides with the onset of TiO_2 film crystallization at the ALD conditions used (Fig. 31) [48]. After RTP treatment, the rms roughnesses of $Er_xTi_{1-x}O_y$ films with ALDCR of 1:8, 1:5, 1:3, and 1:1 are found to barely increase (Fig. 32a), suggesting good thermal stability of the underlying structure; the slight increase in rms roughness of $Er_xTi_{1-x}O_y$ films with ALDCR of 1:12 is likely due to the presence of crystalline phase (Fig. 31). Figures 32b and 32c show the PSI images of RTP-treated amorphous $Er_xTi_{1-x}O_y$ film and crystalline TiO_2 film, respectively; the latter apparently shows a rougher surface with visible clusters on its surface. The rms roughness of post-deposition RTP TiO_2 films, 1.1 nm, is found to be double that of as-deposited films, and such a sharp increase in rms roughness is often accompanied with structural phase change (Fig. 31) [48]. The roughness of the resulting anatase TiO_2 film is similar to that of 30 nm-thick anatase TiO_2 film deposited with the TDEAT/H_2O process,

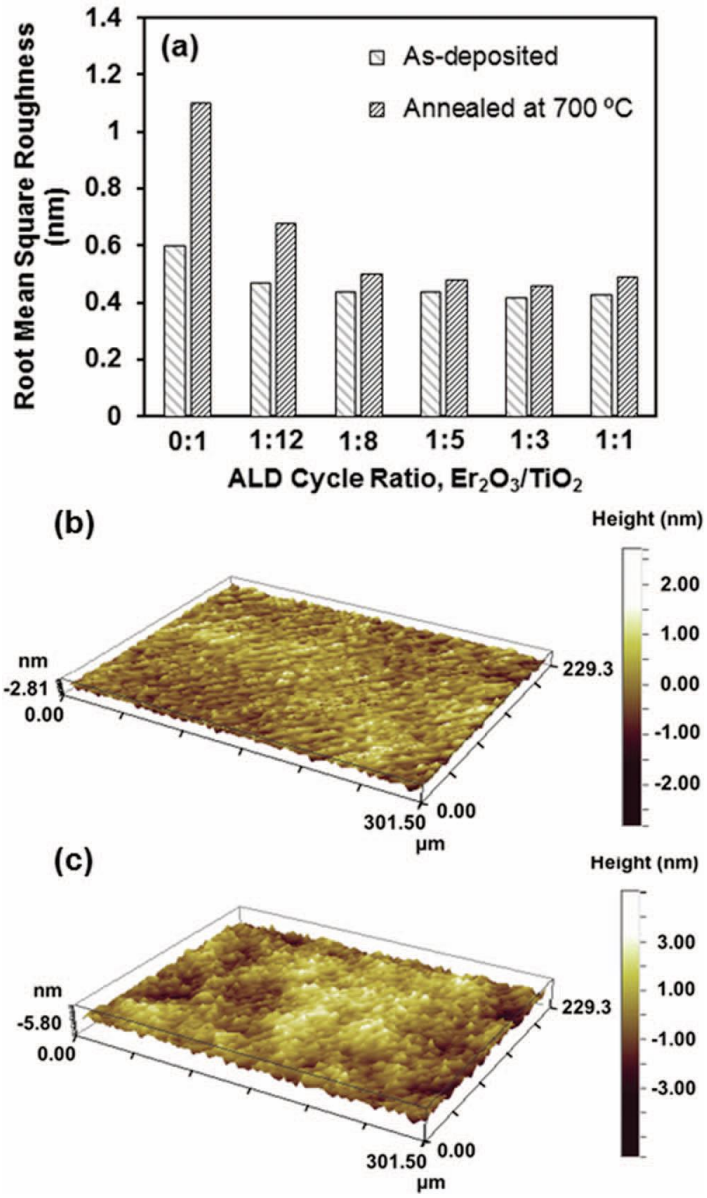

Figure 32. Surface rms roughnesses of as-deposited and RTP-treated TiO_2 and $Er_xTi_{1-x}O_y$ films as measured by PSI (a); PSI images of RTP-treated $Er_xTi_{1-x}O_y$ film with ALDCR of 1:3 (b) and TiO_2 film (c). $Er_xTi_{1-x}O_y$ films were deposited with different ALDCR of 1:12, 1:8, 1:5, 1:3, and 1:1 labeled in (a). All deposition and RTP treatment conditions were the same as those in Fig. 30.

but higher than that of amorphous TiO_2 film (rms = 0.26) deposited at 200 ℃ [48]. Thus, changes in surface morphology and rms roughness are found to relate to structural transitions (e.g., from amorphous to anatase), suggesting that the incorporation of Er into TiO_2 film could suppress crystallization and prevent surface roughening during annealing. An earlier study of TiO_2 showed a much higher rms roughness (~4 nm) for 30 nm-thick TiO_2 deposited by CVD process using TTIP as the metal precursor at 300 ℃ [124], and this indicates the deposition process itself could be another contributing factor to surface roughness.

F. Electrical characteristics

The C-V measurement of $Er_xTi_{1-x}O_y$ films was performed before and after RTP treatment over the voltage range of −3 to +3 V. The electrical parameters of the resulting films were extracted from the C-V data [13]. Figure 33 (inset) shows the hysteretic behavior of $Er_xTi_{1-x}O_y$ films deposited with ALD cycle ratio of Er_2O_3/TiO_2 = 1:1. Prior to RTP, the as-deposited $Er_xTi_{1-x}O_y$ film exhibited an instability in the flatband voltage (i.e., ΔV_{fb} = 1500 mV) and a large hysteresis in the counterclockwise direction. Such hysteretic behavior in the C-V measurements of an MOS capacitor is indicative of the presence of trapped charges in the gate oxide, and this is mostly related to oxygen vacancies or interstitial oxygen defects formed during deposition [13, 123]. Also, the significant shift of flatband voltage toward positive bias suggests a considerable amount of negative charges trapped in the as-deposited film, which is consistent with the high trapped charge density (6.9×10^{12} cm^{-2}) extracted from the C-V data. Since the large hysteresis of as-deposited $Er_xTi_{1-x}O_y$ film still hampers its use for high-κ applications,

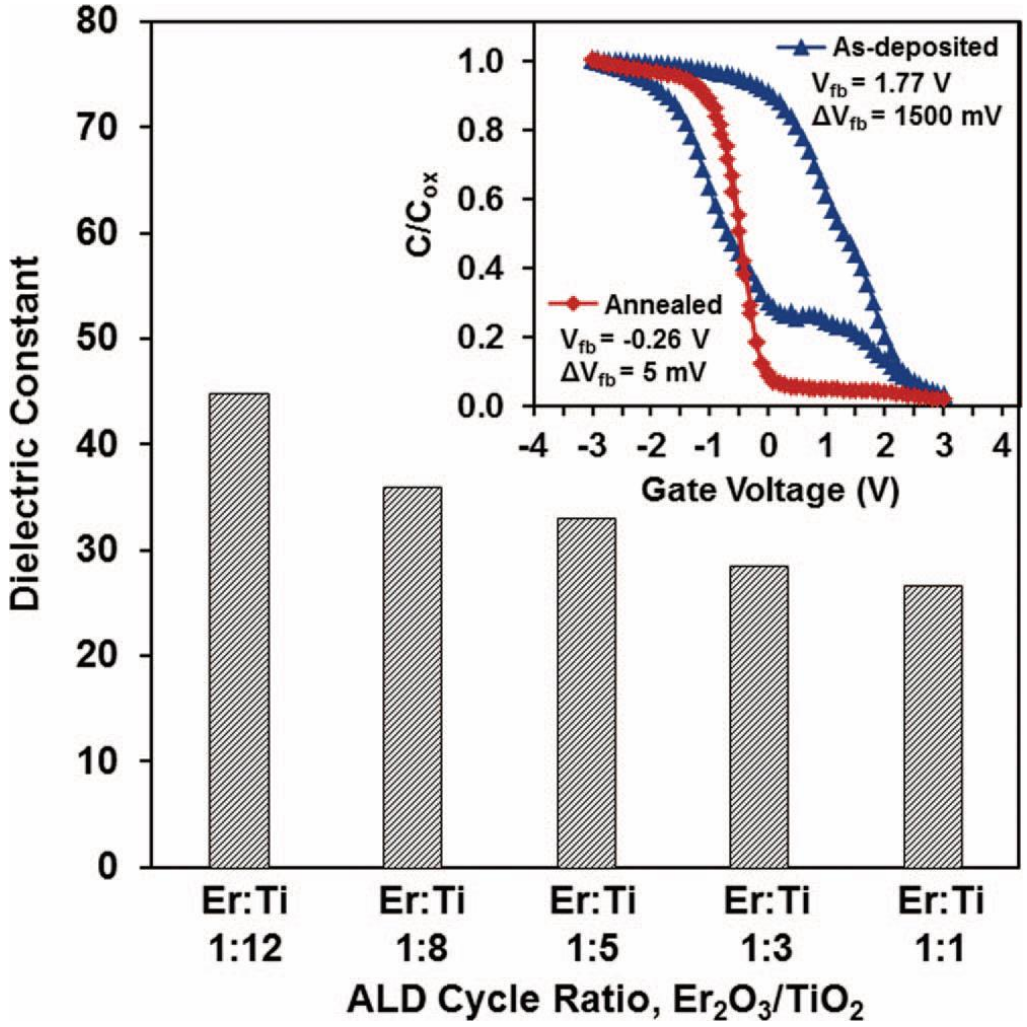

Figure 33. C-V hysteretic behavior for as-deposited and RTP-treated $Er_xTi_{1-x}O_y$ films with ALCR of 1:1 (inset), and the dielectric constant of RTP-treated $Er_xTi_{1-x}O_y$ films as a function of ALDCR (main). The thickness of films is 34 nm. All other deposition and RTP treatment conditions were the same as those in Fig. 30.

additional treatment could be necessary to improve the C-V characteristics of the film.

Based on earlier studies of gate oxides, it is suggested that a large bulk density of defects and trapped charges can be reduced by subjecting gate oxides to appropriate annealing treatments [11, 13]. For instance, Lehnert et al. recently reported that annealing treatment in O_3 at a temperature lower than 400 ℃ could reduce oxygen vacancy defects in TiO_2 dielectrics [45]. In our study, as-deposited $Er_xTi_{1-x}O_y$ films were subjected to post-deposition RTP in O_2 at 700 ℃ for 30 s in order to passivate defects and improve C-V characteristics. As seen in Fig. 33 (inset), the RTP-treated $Er_xTi_{1-x}O_y$ film exhibits a remarkably small hysteresis (i.e., ΔVfb = 5 mV), a flatband voltage at −0.26 V, and a lower trapped charge density (6×10^{11} cm^{-2}), indicating that the RTP treatment used can effectively lead to significant improvements in the C-V characteristics of such structures.

The effect of Er incorporation on the permittivity value of TiO_2-based film at different ALDCR is shown in Fig. 33 (main). Prior to these measurements, all $Er_xTi_{1-x}O_y$ dielectrics were treated with RTP to enhance electrical properties. As the ALDCR increased from 1:12 to 1:1, the dielectric constant of resulting films is found to continuously decrease from 45 to 28, which can be attributed to the increasing content of Er_2O_3 (Fig. 28). The κ value of amorphous $Er_xTi_{1-x}O_y$ films is found to be comparable with that of mostly amorphous $AlTiO_x/Al_2O_3$ films [45], and higher than the highest permittivity (κ=30) of amorphous HfO_2 reported recently [132]. However, the dielectric constant of amorphous $Er_xTi_{1-x}O_y$ is lower than that of TiO_2 (κ=40–110) crystallized in the tetragonal structure (i.e., anatase or rutile). The relatively higher κ value of $Er_xTi_{1-x}O_y$

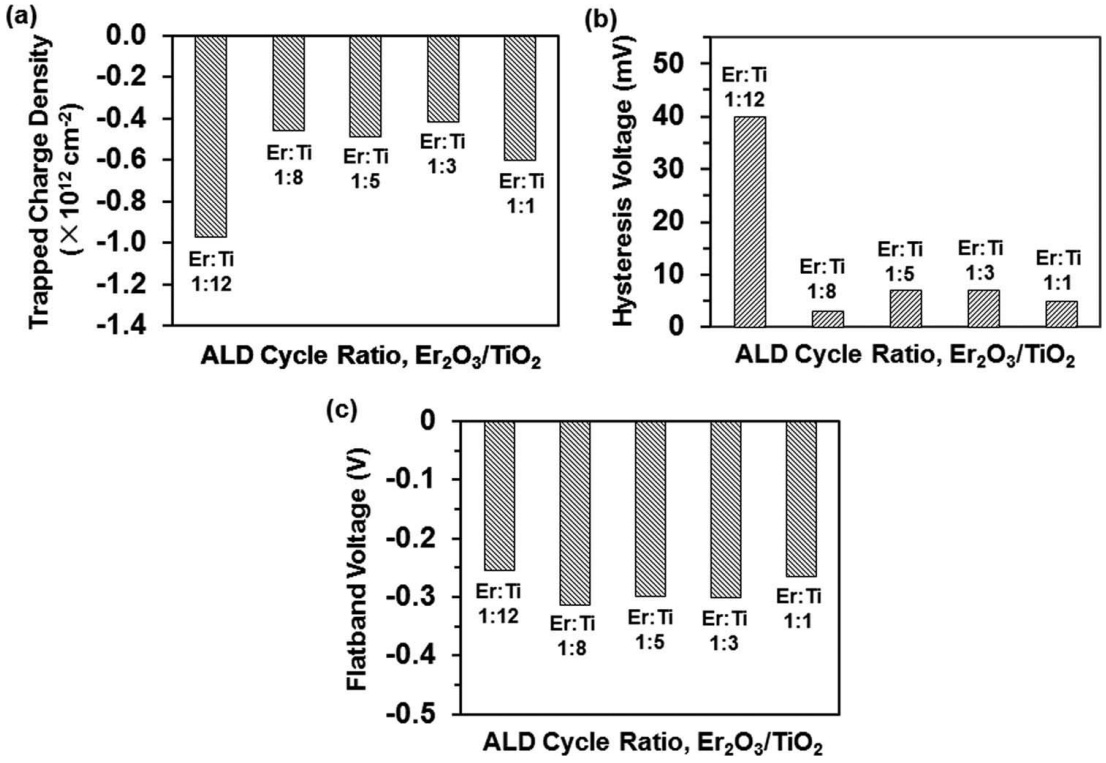

Figure 34. Trapped charge density (a), hysteresis voltage (b), and flatband voltage (c) of RTP-treated 34 nm-thick $Er_xTi_{1-x}O_y$ films deposited with ALDCR of 1:12, 1:8, 1:5, 1:3, and 1:1. All other deposition and RTP treatment conditions were the same as those in Fig. 30.

film with ALDCR of 1:12 can be attributed to the presence of some tetragonal crystalline phase in the bulk film. For high-κ applications, it is desirable for the gate oxide to remain amorphous throughout implemented or necessary annealing process(es), because amorphous films often exhibit isotropic electrical properties and can be deposited by different techniques. On the contrary, grain size and orientation changes throughout a polycrystalline film can cause large variations in its κ value. Furthermore, grain boundaries in crystalline phases often serve as high-leakage paths (planar defects), leading to inferior leakage characteristics (also discussed later).

Figure 34 shows electrical characteristics of RTP-treated $Er_xTi_{1-x}O_y$ films, i.e., trapped charge density, hysteresis voltage, and flatband voltage. The RTP-treated $Er_xTi_{1-x}O_y$ films with ALDCR of 1:8 or higher are found to exhibit low trapped charge densities, on the order of 10^{-11} cm^{-2}, and small hysteresis voltages, less than 10 mV. The trapped charge density of RTP-treated $Er_xTi_{1-x}O_y$ films is seen to be an order of magnitude lower than that of Y-doped HfO_2 film [133]. On the other hand, the RTP-treated $Er_xTi_{1-x}O_y$ film with the lower ALDCR of 1:12 shows a notably higher trapped charge density ($\sim 10^{12}$ cm^{-2}); this could be connected to the phase transition discussed earlier (Fig. 31) and the increased presence of defects in the resulting film.

The leakage current density of crystalline TiO_2 films was investigated previously, and a large value, i.e., 1 A/cm^2 at 1 V, was reported [45]. In this work, as-deposited TiO_2 film is found to exhibit a leakage current density of 10^{-7} A/cm^2 at −1 V, i.e., less than 10^{-4} A/cm^2 at −1 MV/cm (Fig. 35). This is attributed to its mostly amorphous phase of

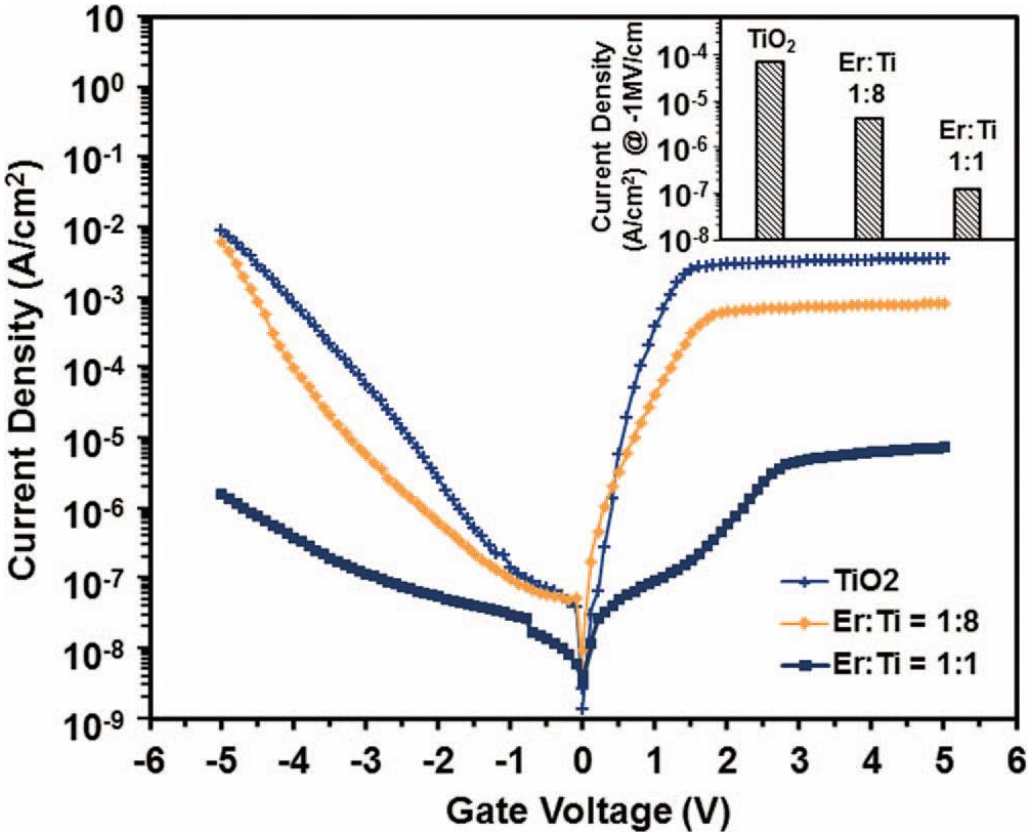

Figure 35. J-V characteristics of as-deposited TiO_2 and $Er_xTi_{1-x}O_y$ films with ALDCR of 1:8 and 1:1 as marked. The inset shows the leakage current density of films measured at −1 MV/cm. The thickness of films is 34 nm. All other deposition and RTP treatment conditions were the same as those in Fig. 30.

the as-deposited film, since crystalline structure can induce undesired grain boundaries, serving as planar defects and high-leakage paths. A leakage reduction was achieved by incorporation of Er_2O_3 intoTiO_2, and this was likely due to the absence of grain-boundary-induced defects in its amorphous phase. Also, the TiO_2-Si conduction-band offset (1 eV) is lower than that of Er_2O_3-Si (3.5 eV) [134]. The leakage current density in $Er_xTi_{1-x}O_y$ films is therefore seen to decrease with increasing Er content (Fig. 35).

The effect of RTP treatment on the J-V characteristics of both TiO_2 and $Er_xTi_{1-x}O_y$ films was also investigated and our results are shown in Fig. 36. The RTP-treated TiO_2 film shows a leakage current density on the order of 10^{-2} A/cm^2 at−1MV/cm. Such a considerable leakage degradation can be attributed to a wide distribution of grain boundaries in TiO_2 arising from a phase transition, e.g., from mostly amorphous into anatase structure. A similar tendency was observed in earlier ALD studies of TiO_2, in which post-deposition annealed TiO_2 films were reported to have worse leakage characteristics resulting from crystallization [45, 46]. In this study, the leakage current density of RTP-treated TiO_2 with anatase structure is one order of magnitude lower than that of rutile TiO_2 reported earlier (10^{-1} A/cm^2) [46], and this is likely related to a higher band gap of anatase TiO_2 (3.2 eV) than that of rutile TiO_2 (3.0 eV). Among RTP-treated $Er_xTi_{1-x}O_y$ films with different ALDCR, the film with an ALDCR of 1:12 is found to exhibit a leakage current density of 10^{-2} A/cm^2 at −1 MV/cm, which is at least 5 orders of magnitude higher than that of films with ALDCR of 1:8 or higher. This is in agreement with our GIXRD results, which showed the presence of anatase phase in the RTP-treated

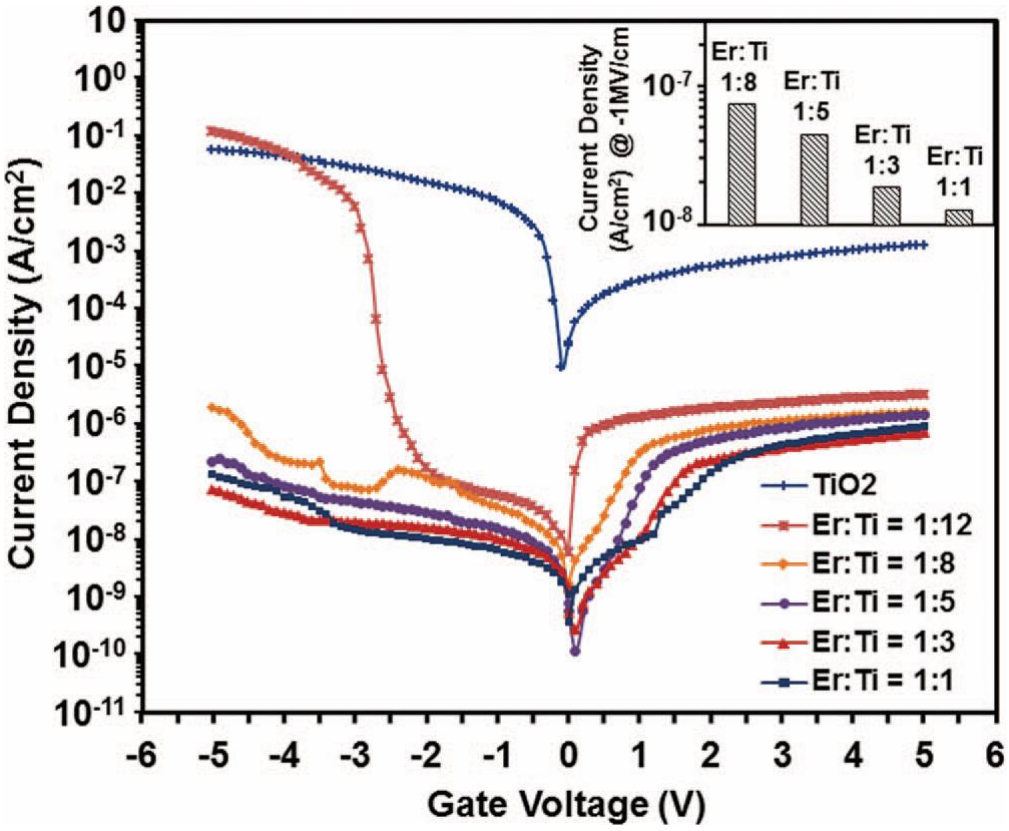

Figure 36. J-V characteristics of RTP-treated TiO_2 and $Er_xTi_{1-x}O_y$ films deposited with ALDCR of 1:12, 1:8, 1:5, 1:3, and 1:1. The inset shows the leakage current density of films measured at −1 MV/cm. The thickness of films is 34 nm. All deposition and RTP treatment conditions were the same as those in Fig. 30.

$Er_xTi_{1-x}O_y$ film with ALDCR of 1:12. The significant improvement in leakage reduction obtained for RTP-treated amorphous $Er_xTi_{1-x}O_y$ films with ALDCR of 1:8 or higher could be attributed to two factors: first, the post-deposition RTP could saturate oxygen vacancies and fix related defects, which are major source of charges and can act as leakage paths in metal oxides [11]; and second, as the GIXRD results showed, the RTP-treated $Er_xTi_{1-x}O_y$ films with ALDCR of 1:8 or higher can effectively suppress crystallization and remain amorphous (Fig. 31) that in turn lack planar defects, such as grain boundaries.

The leakage current density of amorphous $Er_xTi_{1-x}O_y$ films (10^{-8} A/cm^2 at −1 MV/cm) is one order of magnitude lower than 125 nm-thick amorphous $AlTiO_x$ film deposited on TaN with a 4 nm-thick Al_2O_3 interlayer [45]. Yet, the $AlTiO_x/Al_2O_3$ film was reported to be incompatible with Si, showing a much higher leakage current density of 5×10^{-4} A/cm^2 at 0.16 MV/cm on a Si electrode. An amorphous Ta-doped TiO_2 dielectric deposited with ALD was reported to exhibit a leakage current density of 10^{-3} A/cm^2 at 1MV/cm [47]. Co-ALD of ZrO_2 and TiO_2, $Zr_xTi_yO_2$, was found to result in films with a dielectric constant of ~20 and a leakage current of 10^{-5} A/cm^2 at 1 MV/cm, while its preferred amorphous state was maintained up to 600 ℃ [46]. Thus, the electrical properties of optimized amorphous $Er_xTi_{1-x}O_y$ films in our study include a dielectric constant of ~36, hysteresis voltages of less than 10 mV, trapped charge densities of~10^{11} cm^{-2}, flatband voltages of ~−0.3 V, and leakage current densities of 10^{-8} A/cm^2 at −1 MV/cm on Si.

4.2.4. Summary

A combination of binary ALD processes was developed and demonstrated for the growth of $Er_{1-x}Ti_xO_y$ dielectrics using tris(methylcyclopentadienyl)erbium and tetrakis(diethylamino)-titanium as metal precursors with O_3 as oxidant. The growth rates of Er_2O_3 and TiO_2 with temperature-optimized ALD conditions were found to be 0.12 and 0.047 nm/cycle, respectively. A sufficient overlapping temperature window of $(CpMe)_3Er/O_3$ and TDEAT/O_3 processes was obtained between 175 and 250 ℃. The atomic ratio of Er/(Er+Ti) in $Er_{1-x}Ti_xO_y$ films was found to increase monotonically with increasing normalized cycle ratio of $Er_2O_3/(Er_2O_3+TiO_2)$, showing excellent tunability of the thin film composition. No nitrogen and carbon contamination was detected in the film. Interfacial layer XPS studies suggested the presence of silicate and silicon oxide after deposition, while an increased formation of SiO_2 was observed after RTP at 700◦C in O_2 at 1 atm. TiO_2 was found to start crystallizing at the ALD conditions used as detected by GIXRD and the as-deposited TiO_2 showed a relatively small rms roughness value; after RTP, a sharp increase in the intensity of the crystalline features along with a larger rms value corroborated a mostly amorphous-to-anatase phase transition. $Er_{1-x}Ti_xO_y$ films deposited with ALDCR of 1:8 or higher showed desired levels of uniformity, surface roughness, and good thermal stability up to 700 ℃. The resulting amorphous $Er_{1-x}Ti_xO_y$ films after RTP treatment showed a dielectric constant of ~36, small hystereses (i.e., less than 10 mV), low trapped charge densities ($\sim 10^{11}$ cm^{-2}), and low leakage current densities on the order of 10^{-8} A/cm^2 at −1 MV/cm on p-type Si. Therefore, the incorporation of Er into TiO_2 combined with the RTP treatments used exhibited a remarkable improvement over pure TiO_2 films ($J = 10^{-2}$ A/cm^2 at −1 MV/cm).

4.3. Chemical Passivation of GaSb-based Surfaces by Atomic Layer Deposited ZnS Using Diethylzinc and Hydrogen Sulfide

4.3.1. Introduction

Gallium Antimonide (GaSb) is an important semiconductor in a wide range of electronic devices, such as high speed electronics [15, 16], photovoltaic cells [17-19], and near- and far-infrared optoelectronic devices [20]. In particular, GaSb is important for enabling mid- and long-wavelength infrared (MWIR and LWIR) detectors in terms of their moderate band gap (0.72 eV) and intrinsic carrier concentration [20, 21]. However, issues including unsatisfied dangling bonds and native oxides result in inferior surface quality, which yields non-negligible leakage currents and limits the long-term performance of GaSb-based devices [23-25]. Therefore, for improvements in the overall GaSb-based device performance, one of the demanding challenges is the surface passivation of GaSb.

Previous studies have been devoted to sulfur passivation in order to effectively remove native oxides and passivate exposed GaSb-based surfaces. So far, the most common means of sulfur passivation treatments have been based on the use of aqueous solutions of inorganic or organic sulfides, such as sodium sulfide (Na_2S) [24, 52], ammonium sulfide [$(NH_4)_2S$] [26, 53], and thioacetamide (TAM) [27, 54]. Among these, the TAM-based treatment has been reported to provide superior passivation for GaSb-based surfaces and to offer advantages such as milder reaction conditions and the ability to passivate surfaces under both acidic and basic conditions. However, TAM-based passivation offers good protection against oxidation only for about one day [27]. Hence, a

thin solid layer of encapsulating material has been under investigation in order to prevent/minimize degradation of device performance over time and to maintain long-term stability of passivated GaSb surfaces. For instance, Gin et al. investigated the surface passivation of type II InAs/GaSb superlattice photodiodes using a 150 nm-thick layer of SiO_2 deposited with plasma enhanced chemical vapor deposition, and the SiO_2-passivated device showed a higher device resistance and lower reverse bias dark current [55]. More recently, Banerjee et al. deposited ZnS thin film using molecular beam epitaxy for surface passivation. After comparisons of the efficacy of different thin film passivation layers, the authors reported that a ZnS cap film following $(NH_4)_2S$ surface treatment was superior to that obtained with SiO_2 and Si_xN_y which were deposited with plasma enhanced chemical vapor deposition and sputtering [25].

A challenge in the implementation of ZnS passivation film is the development of a suitable route for the thin film growth on three-dimentional (3D) structures of different devices, especially on side wall and mesa structures of infrared detectors. Atomic layer deposition has been widely identified as one of the preferred means of fabricating 3D features in the integrated circuit industry [57]. The self-limiting nature of ALD offers a wide range of possibilities and it meets the challenging requirements for enabling future optoelectronic devices, such as precise thickness control, excellent uniformity, and conformality for all needed dimensions [38].

In this work, ultrathin ZnS passivation films are grown by ALD in order to enhance the chemical passivation of TAM-treated GaSb-based surfaces. X-ray

photoelectron spectroscopy (XPS) is used to investigate GaSb-based surfaces passivated with a TAM-treatment or with an ALD ZnS passivation film on the nanometer length scale following TAM treatment. For the chemical passivation of TAM-treated InAs/GaSb structures with different thickness ZnS films (i.e., 1 and 2 nm), the effect of thickness on the chemical passivation efficacy of these systems is investigated. The extent of oxidation of passivated GaSb-based surfaces exposed to atmospheric air is also studied over time.

4.3.2. Experimentation

The ALD and characterization of ZnS thin films were done on TAM-treated p-type GaSb substrates and on TAM-treated InAs/GaSb type-II strained-layer superlattices (SLS) structures. For the GaSb substrates, prior to the ALD ZnS, 10 mm by 10 mm sections of GaSb substrates were degreased in acetone and methanol to remove organic contaminants, rinsed in deionized (DI) water, and dried with N_2 (99.996%) gas. For the removal of native oxides, the GaSb substrates were next soaked in TAM solution (0.2 mol/L) at 70 ℃ for 30 min and the pH of the TAM solution was adjusted to 2.0 by adding acetic acid (10%).

The InAs/GaSb type-II SLS structures were 1.86 μm-thick and consisted of 13 monolayers (ML) InAs/7 ML GaSb/1.3 ML InSb (300 periods) grown on a 5 mm by 5 mm section of GaSb (100) substrate using a solid source molecular beam epitaxy (MBE, VG 80 system) [25]. The InSb layer was incorporated in every SLS period to compensate for the strain along the growth direction. The samples were degreased in acetone and methanol, rinsed in deionized (DI) water, and blown dry with N_2. A fresh surface was

exposed by etching the samples for 1 min with a hydrogen peroxide (H_2O_2): phosphoric acid (H_3PO_4): DI water (2:1:20) etching solution. The abovementioned TAM-based treatment was then carried out on the resulting surface. One of the samples was left as-treated with TAM for comparison purposes, while the remaining ones were capped with ALD ZnS nanofilms following the TAM-treatment.

The ALD of ZnS made use of diethylzinc (DEZn, Sigma-Aldrich Co. Ltd., St. Louis, MO, USA) and H2S (99.5%, Matheson Gas Products Inc., USA) precursors in a tubular hot wall ALD reactor maintained at 200 ℃; during deposition, both DEZn and H_2S were kept at room temperature (25 ℃). Argon (99.999%) was used as both carrier gas for the delivery of each precursor and purge gas for cleaning the system in between the delivery of the Zn and S precursors. The thicknesses of ZnS thin films were measured using a spectral ellipsometer (M-44, J. A. Woollam Co. Inc., USA); for each thickness determination, three measurements across the entire deposition area were carried out with mean value representing the film thickness. The index of refraction model for ZnS was provided by J. A. Woollam Co. Inc. Chemical binding energies and elemental quantifications of as-deposited ZnS were analyzed with XPS (Kratos AXIS-165, Kratos Analytical Ltd., United Kingdom), which was equipped with a monochromatic Al Kα (1486.6 eV) x-ray source operating at 15 KV and 10 mA. XPS measurements were carried out at 90 ºtake-off angle using a concentric hemispherical analyzer coupled with a charge neutralizer. All XPS scans were done at room temperature under ultrahigh vacuum (base pressure ~5×10^{-7} mtorr) with 0.1 eV step size, 300 ms dwell time, and no additional in situ processing. X-ray photoelectron spectra analyses were performed

through spectral peak-fitting, where peaks were subtracted from Shirley-type backgrounds and deconvoluted using Gaussian-Lorentzian peak shape functions (software XPSPEAK, version 4.1). The spectral line of C 1s (284.6 eV) was used for the calibration of the binding energy. A high resolution x-ray diffractometer (X'Pert, PANalytical B.V. Co., Netherlands) configured with 0.1542 nm x-ray emission line of Cu with bandwidth of 0.05 nm as the excitation source was used to obtain glancing incidence x-ray diffraction (GIXRD) diffractogram of ZnS film. The diffractogram was collected at an incident angle of 0.7 ^{o}to enhance the diffraction sensitivity within the film and to avoid interference from the GaSb-based substrates. Surface morphology of as-deposited ZnS thin film was also studied using an optical surface profiler system (Wyko NT3300, Veeco Instrument Inc., USA) in the phase-shifting interferometry (PSI) mode with a vertical resolution of 0.1 nm.

4.3.3. Results and Discussion

A. Film growth

Figure 37 (a) shows the effect of varying the pulse time of DEZn on the growth rate of ZnS films, studied at 200 ℃ with the error bars representing standard derivations of film thickness measurements at three points across the entire substrate area. During the deposition process, hydrogen sulfide was pulsed into the reactor for 500 ms, follow by 10 s Ar purging. The amount of precursor dosage was controlled with the duration of precursor pulse. The growth rate of ZnS was found to increase with increasing precursor pulse time and saturate after 80 ms. Figure 37 (b) shows the dependence of ZnS growth rates on H_2S pulse time with a constant DEZn pulse time of 85 ms. The growth rate of

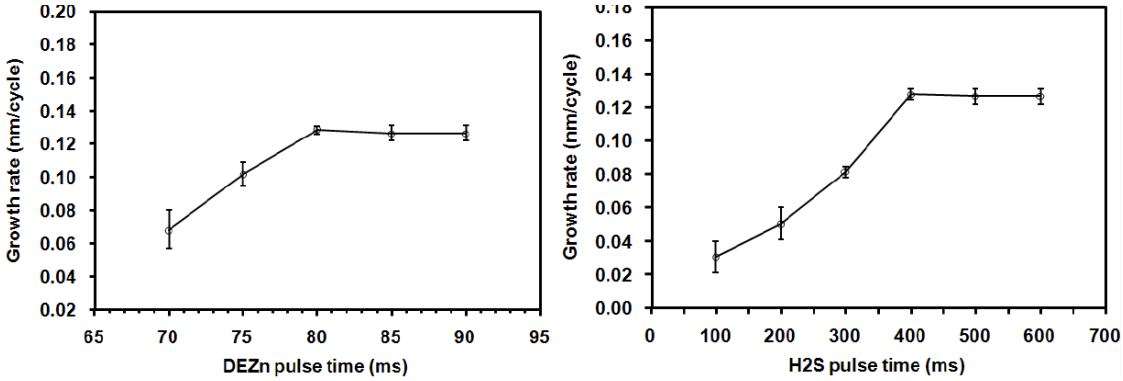

Figure 37. Growth rates of ZnS films on TAM-treated GaSb substrates as a function of DEZn precursor pulse (a) and H_2S pulse (b) at 200 ℃. The Zn precursor was maintained at room temperature. Hydrogen sulfide was pulsed into the reactor for 500 ms.

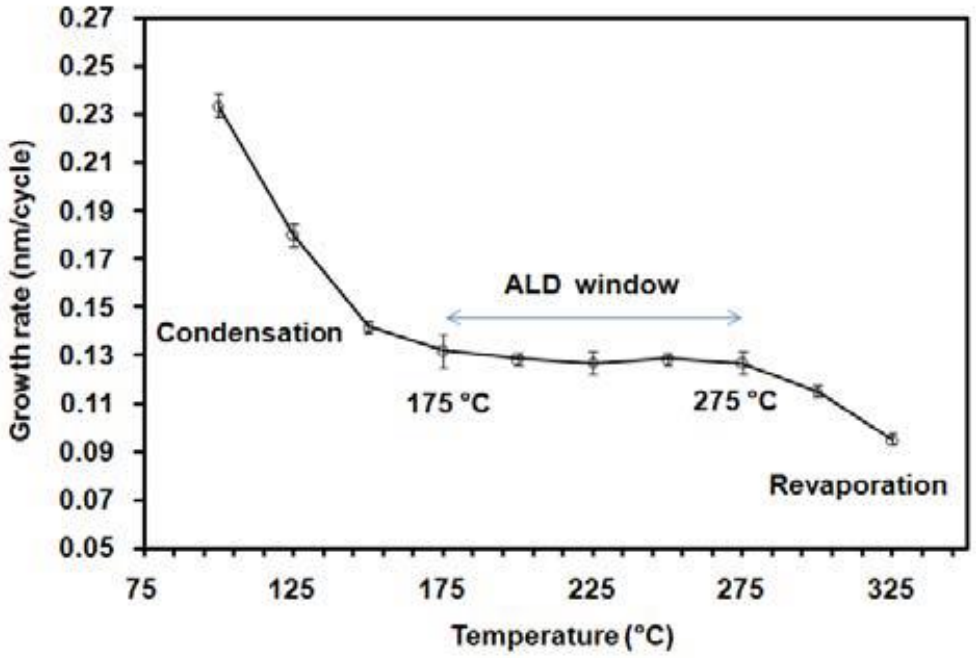

Figure 38. ZnS growth rate as a function of reactor temperature with 85 ms DEZ pulse time. The other deposition conditions were the same as those in Fig. 37(a).

ZnS was found to saturate after H_2S pulse of 400 ms (Fig. 37b). These growth behaviors indicate that ZnS ALD from DEZn and H_2S in our system occurs through self-limiting growth kinetics.

The reactor temperature dependence of growth rates is investigated and shown in Fig. 38. In these studies, all the depositions were carried out with DEZn and H_2S pulse times of 85 and 500 ms, respectively. The higher growth rates at the low temperature region of 100–175 ℃ often results from the condensation of precursor vapor on the substrate, while the lower growth observed at the high temperature region of 275–325 ℃ is likely due to the lower adsorption of the precursor on reaction surface. A wide ALD temperature window in the range of 175 – 275 ℃ was observed, with a growth rate of 0.13 ± 0.01 nm/cycle.

The self-limiting nature of ALD ideally yields linear growth with increasing number of ALD cycles, which allows precise thickness control during deposition. However, studies of ALD are sometimes reported with an incubation (or initiation) period prior to the linear growth of nanoscale films [135, 136], and this has been attributed to poor nucleation at the initial stage of film growth; for example, on surfaces which may lack active adsorption sites [136, 137]. In view of such process considerations, a better understanding of the initial stage of deposition is important.

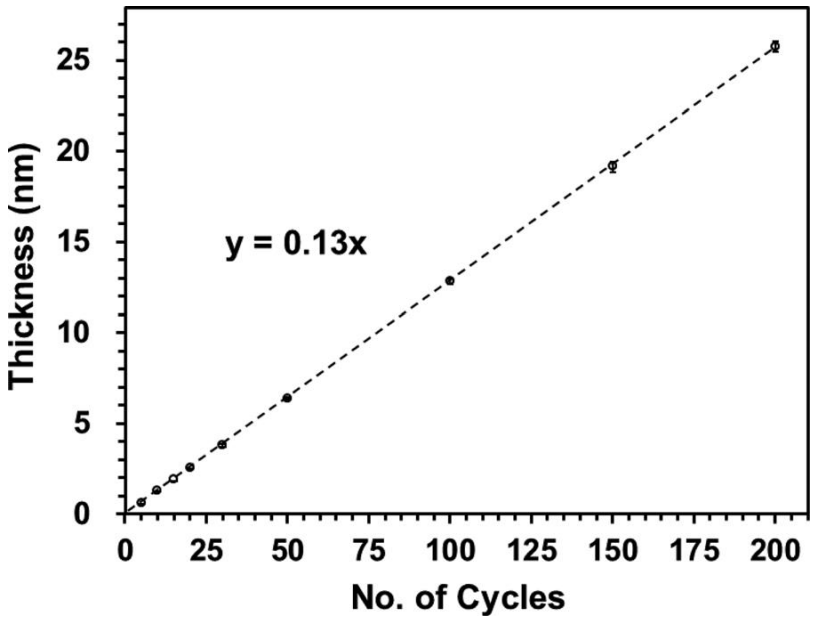

Figure 39. Thickness of ZnS as a function of the number of ALD cycles at 200 ℃. ZnS films are deposited on TAM-treated GaSb substrates. The DEZn precursor and H_2S are at room temperature and they are pulsed into the reactor for 85 and 500 ms, respectively.

The growth behavior of ZnS thin films deposited on TAM-treated GaSb surfaces at 200 ℃ was investigated in detail with spectral ellipsometry for 5–200 ALD cycles. Our results show linear dependence of the ZnS film thickness with the number of ALD cycles, as it is illustrated in Fig. 39. From the linear regression analysis of the data, the growth rate is found to be 0.13 nm/cycle, which is higher than that of ZnS films deposited from the same precursor on silicon substrates in an earlier study [138]. The growth mechanism of ZnS from $Zn(C_2H_5)_2$ and H_2S on silicon was reported in earlier studies. The relevant reaction on the substrate surface during the zinc precursor pulse is surface-S-H + $Zn(C_2H_5)_2 \rightarrow$ surface-S-Zn-C_2H_5 + C_2H_6 [139, 140], which suggests that the robust chemical adsorption of $Zn(C_2H_5)_2$ likely requires active adsorption sites of sulfide species (i.e., surface-S-H) [140].

As seen in Fig. 39, the linear growth behavior is observed from the very early stage of ZnS growth on TAM-treated GaSb substrates under the ALD conditions used. The lack of incubation period at the very beginning is likely due to the presence of an ultrathin layer of sulfide on the GaSb surface after the TAM-treatment, which can enhance the surface adsorption of the metal precursor.

B. XPS analyses of ALD ZnS films

Figure 40 shows the XPS spectra of an as-deposited 15 nm-thick ZnS film on a TAM-treated GaSb substrate. It includes the core level spectra of Zn 2p and S 2p. The core level spectrum of Zn 2p consists of two peaks corresponding to Zn $2p_{1/2}$ (1044.5 eV) and Zn $2p_{3/2}$ (1021.5 eV) with the standard spin-orbital splitting (SOS) of 23 eV, which is

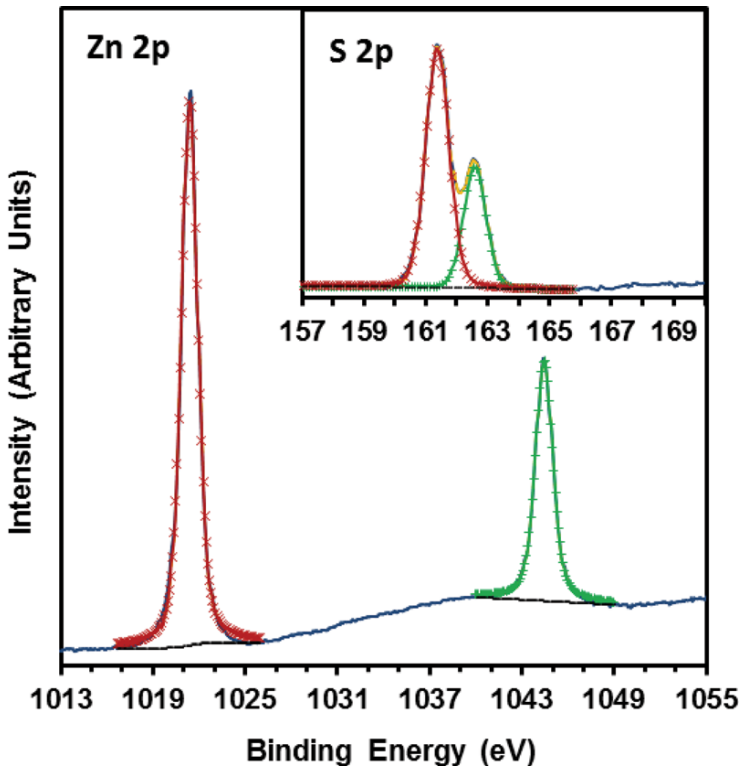

Figure 40. (Color online) Zn 2p and S 2p (inset) core scans of 15 nm-thick as-deposited ZnS. XPS spectra are collected at 90 ºtake-off angle. Other deposition conditions are the same as in Fig. 39.

attributed to the formation of ZnS [141]. A doublet is observed for S 2p (inset of Fig. 40), and its spectrum could be fitted with two Gaussian–Lorentzian distributions at 162.6 for S $2p_{1/2}$ and 161.4 eV for S $2p_{3/2}$ with a SOS of 1.2 eV, which corroborates the formation of ZnS [142]. Also, there are no peaks observed in the binding energy range of 164–170 eV, indicating no formation of other sulfur species in the as-deposited film, such as elemental sulfur (164.0 eV), chemisorbed SO_2^{2-} (163–165.5 eV), sulfite SO_3^{2-} (166.4 eV), or sulfate SO_4^{2-} (168–170 eV) [142]. The elemental ratio of Zn:S is found to be 49.9:50.1 at.% using quantitative analyses of peak intensities and it suggests that the resulting ZnS films are stochiometric. These XPS analyses of ALD ZnS are consistent with that of ZnS deposited by chemical bath deposition and ALD on silicon in earlier reports [142, 143].

C. Passivation of TAM-treated GaSb

The studies on the passivation of GaSb surfaces were carried out with XPS analyses. The elemental components and changes in different samples are presented in Table I. The quantification is based on quantitative analyses of peak intensities of the corresponding elements.

a. Freshly passivated GaSb

Figure 41 shows the XPS core level spectra of Ga $2p_{3/2}$ and Sb $3d_{3/2}$ obtained from TAM-treated GaSb substrates and GaSb passivated with ALD ZnS after the TAM treatment. Figure 41(b) shows that prior to the ALD of ZnS, the TAM treatment is effective in removing the native oxide of Ga, because of the absence of a corresponding peak at 1118.3 eV. The feature centered at the binding energy of 1117.2 eV is assigned to

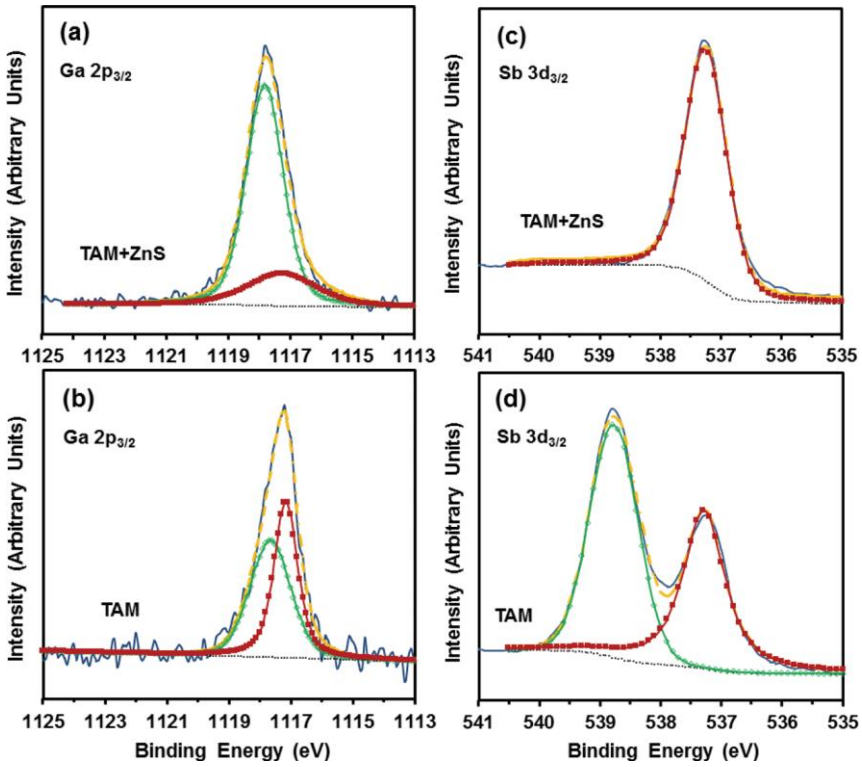

Figure 41. (Color online) Ga $2p_{3/2}$ [(a) and (b)] and Sb $3d_{3/2}$ [(c) and (d)] core scans of GaSb substrates capped with a 1 nm-thick ZnS layer following treatment with TAM and TAM-treated GaSb substrates, respectively. Both GaSb substrates were loaded into the XPS chamber immediately after the corresponding treatment. XPS spectra were collected at 90 º take-off angle. Other ALD conditions are the same as those in Fig. 39.

Ga–Sb bonds in GaSb. The higher binding energy feature centered at 1117.8 eV corresponds to Ga–S, which is attributed to the formation of gallium sulfide during the TAM treatment; this is in agreement with an earlier study on the passivation of GaSb surfaces with TAM [27]. After the ALD of 1 nm-thick ZnS on TAM-treated GaSb, the Ga–Sb peak intensity at 1117.2 eV is reduced (Figs. 41(a) and 41(b), and Table I), whereas the Ga–S feature at 1117.8 eV is significantly enhanced. This is indicative of increased formation of gallium sulfide at the interface under the deposition conditions used.

The XPS spectra of Sb $3d_{3/2}$ are shown in Figs. 41(c) and 41(d). Immediately after TAM treatment, two symmetric peaks are observed, indicating two different chemical binding states of Sb on the surface of TAM-treated GaSb [Fig. 41(d)]. The low energy state, centered at 537.3 eV, is attributed to Sb in bulk GaSb. The high energy state at 538.8 eV is assigned to Sb–S resulting from the TAM treatment.

No peaks are found at higher binding energies (e.g., 540 eV), indicating that native oxides of Sb are effectively removed with the TAM treatment. Thus, the GaSb surface treated with TAM seems to be a mixture of Ga–S and Sb–S, which can enhance the initial growth of ZnS on such substrates and result in the linear deposition rate behavior observed from the early stages of film growth (Fig. 39). Moreover, in an earlier study, the formation of Ga–S and Sb–S were observed on ammonium sulfide-treated GaSb, and no evidence was found that S on the treated surface was lost during annealing at 300 ℃ [144].

After the ALD of 1 nm-thick ZnS on TAM-treated GaSb, an intense feature at 537.3 eV is observed and attributed to Sb in Ga–Sb [Fig. 41(c)]. The XPS feature at 538.8 eV attributed to Sb–S seems to disappear from the spectrum of the TAM-treated GaSb with the ZnS passivation film, which suggests increased formation of another sulfide, e.g., gallium sulfide, under our ALD conditions; this is indeed corroborated by the tandem significant increase of the gallium sulfide XPS feature (Fig. 41(a) and Table I). Therefore, after the capping of TAM-treated GaSb surface with the 1 nm-thick ALD ZnS layer, the major species at the interface of ZnS/TAM-treated GaSb system is found to be gallium sulfide.

b. Evolution of passivated GaSb surfaces in atmospheric air

In order to study the extent of (re)oxidation of passivated surfaces over time, the same samples (i.e., TAM-treated GaSb and TAM-treated GaSb capped with ALD ZnS) were left in the cleanroom atmosphere for a long-term exposure to air before repeat XPS measurements and analyses were carried out.

Figure 42 shows the core level spectra of Ga $2p_{3/2}$ and Sb $3d_{3/2}$ of the same samples after they are exposed to the atmospheric air for 14 days. In Figs. 42(a) and 42(b), a new fitted peak centered at the higher binding energy of 1118.3 eV is now observed in the spectra of both samples passivated with and without a ZnS passivation film; that is indicative of the appearance of gallium oxide resulting from the air oxidation of GaSb surfaces. However, when compared to the TAM-treated GaSb sample (with 44% Ga–O, Table I), the TAM-treated GaSb with the ZnS nanofilm shows significantly less intense

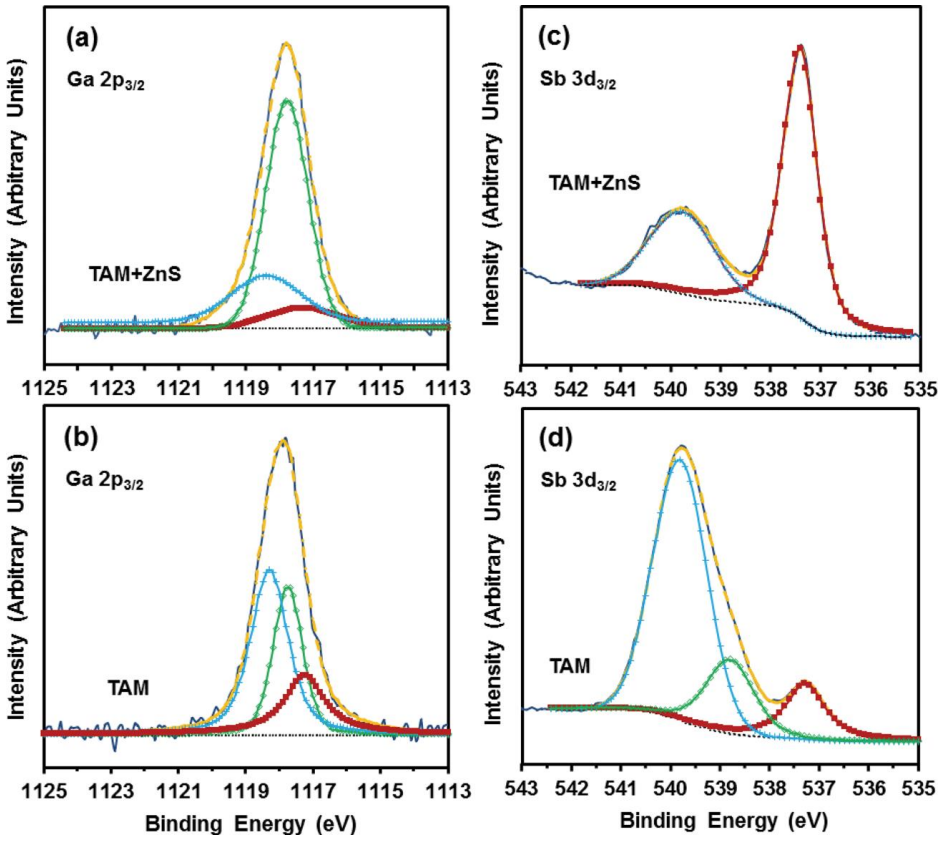

Fig. 42. (Color online) Ga $2p_{3/2}$ [(a) and (b)] and Sb $3d_{3/2}$ [(c) and (d)] core scans of GaSb substrates capped with a 1 nm-thick ZnS layer following treatment with TAM and TAM-treated GaSb substrates, respectively. Both GaSb substrates were loaded into the XPS chamber after 14 days of exposure to atmospheric air. XPS spectra were collected at 90 ° take-off angle. Other ALD conditions are the same as those in Fig. 39.

Peak	Component	Binding energy (eV)	Intensity percentage (%)			
			Fresh passivation		After 14 days	
			TAM	TAM + ZnS	TAM	TAM + ZnS
Ga $2p_{3/2}$	Ga–Sb	1117.2	57	13	17	7
	Ga–S	1117.8	43	87	39	76
	Ga–O	1118.3	0	0	44	17
Sb $3d_{3/2}$	Sb–Ga	537.3	40	100	13	79
	Sb–S	538.8	60	0	16	0
	Sb–O	540.0	0	0	71	21

Table I. XPS results of passivated GaSb surfaces immediately following treatment and after 14 days of exposure to atmospheric air.

presence of Ga–O (i.e., 17%); this suggests that even 1 nm-thick ZnS noticeably reduces the formation of gallium oxide at the interface of ZnS/TAM-treated GaSb system.

The binding energies in the spectra of Sb $3d_{3/2}$ have also been obtained and shown in Figs. 42(c) and 42(d), after the samples are exposed to atmospheric air for 14 days. The higher binding energy peak appearing at 540.0 eV shows the presence of Sb–O in both TAM-treated GaSb samples passivated without and with the ZnS passivation nanofilm; this is attributed to the oxidation of Sb after exposure to the atmospheric air. For TAM-treated GaSb, the intense peak observed at 540 eV suggests a considerable amount of antimony oxide (i.e., 71%, Table I) formed on the surface during the long-term exposure to the atmosphere. On the other hand, ZnS passivated TAM-treated GaSb shows a weaker peak at 540 eV (i.e., 21%), indicating a significantly reduced amount of Sb–O formed at the interface during the long term exposure to air. These results show that air oxidation of TAM-treated GaSb surfaces can be substantially reduced with an ultrathin ZnS passivation film. The relative peak intensities of GaSb seem to decrease with the appearance of oxides during exposure in the atmosphere over time, which is also indicative of the oxidation of the underlying bulk GaSb. This can be the result of oxygen diffusion through the ultrathin sulfide film coupled with interfacial chemistry, which could be in agreement with an earlier study of passivation using TAM aqueous solution [27].

D. Passivation of TAM-treated InAs/GaSb

a. Freshly passivated InAs/GaSb substrates

Figure 43 shows the XP spectra of In $3d_{5/2}$, As 3d, and Sb $3d_{3/2}$ obtained from TAM-treated InAs/GaSb and InAs/GaSb passivated with 1 and 2 nm-thick ALD ZnS following the TAM treatment. In the analyses of chemical binding energies of InAs/GaSb nanostructures, In $3d_{5/2}$ and As 3d peaks were desirable for use in characterization of S-passivated surfaces, because they offered favorable features for XPS analyses, such as high intensity, narrow full width at half maximum, and large chemical binding energy shifts between different chemical bonds. For comparison purposes of the different samples, each element of the corresponding components was identified and quantified in Table II. The quantification method used was the same with that used for the data of Table I.

The bottom graph of Fig. 43(a) illustrates that the TAM treatment is effective in removing the native oxide of In, due to the absence of the oxide shifted peak of In $3d_{3/2}$ at 445 eV. The intensive peak centered at 444.1 eV represents In bonded to As or Sb, while the small feature at 444.7 eV is attributed to In–S resulting from the TAM-treatment [27]. After the ALD of ZnS on TAM-treated InAs/GaSb surfaces, an increase in the intensity of the In–S peak at 444.7 eV is observed (Fig. 43(a), middle and top spectra), whereas the intensity of the peak centered at the lower binding energy of 444.1 eV is found to decrease (Table II); this is due to the increased presence of In–S at the interface for the ALD conditions used.

The XPS spectra of As 3d are shown in Fig. 43(b). For a TAM-treated surface, peaks observed at 40.7 and 42.9 eV are assigned to As–In and As–S, respectively [145].

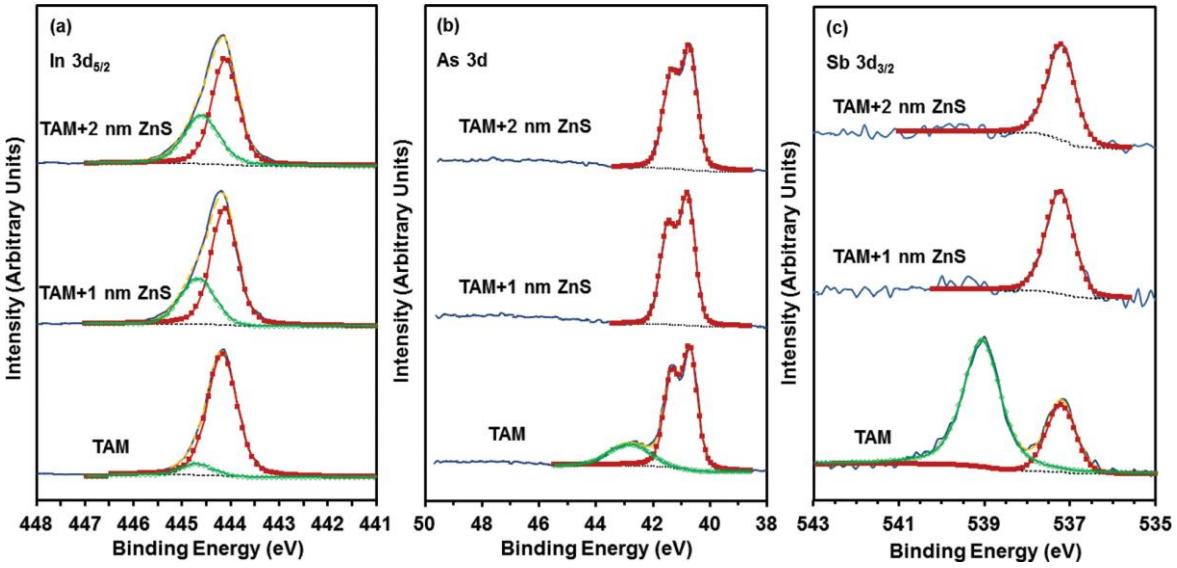

Figure 43. (Color online) In $3d_{5/2}$ (a), As 3d (b), and Sb $3d_{3/2}$ (c) core scans of TAM-treated InAs/GaSb surfaces (bottom) and InAs/GaSb surfaces passivated with 1 (middle) and 2 (top) nm-thick ZnS following TAM treatment. All samples were loaded into high vacuum XPS chamber immediately after passivation and treatment. XPS spectra were collected at 90 ° take-off angle. Other ALD conditions are the same as those in Fig. 39.

No peaks are observed at the higher binding energy for As–O (45.7 eV), suggesting the complete removal of native oxides of As. After the ALD of ZnS on TAM-treated InAs/GaSb, an intense doublet is observed at 40.7 eV and it is attributed to In–As [middle and top graphs of Fig. 43(b)]. The XPS feature for As–S at 42.9 eV seems to disappear from the spectra, and this corroborates the tandem increase of the indium sulfide XPS feature after the ALD ZnS (Fig. 43(a) and Table II).

Ga 2p was also used to analyze the bonding energy changes of Ga in the resulting samples (with and without ALD ZnS); however, no peaks could be observed in the spectra; this was likely because Ga was covered by other components and could not be detected using XPS. The XPS spectra of Sb $3d_{3/2}$ are shown in Fig. 43(c). For TAM-treated surface, two symmetric peaks are observed, showing the two different chemical binding states of Sb on the surface. The low energy state centered at 537.3 eV is attributed to In–Sb. The higher bonding energy state, at 538.8 eV, is assigned to Sb–S resulting from the TAM treatment. The lack of peaks at higher binding energies (e.g., 540 eV) shows that native oxides of Sb are effectively removed with the TAM treatment. Therefore, the surface of samples treated with TAM is indeed a mixture of sulfides; this is consistent with an earlier study based on the use of TAM for surface passivation [27]. After the ALD of ZnS, the Sb–S peak disappears, just like the As–S feature does [middle and top graphs of Figs. 43(b) and 43(c)]. Hence, following the capping of TAM-treated surfaces with an ALD ZnS thin film, the major species at the interface of ZnS/TAM-treated samples is found to be indium sulfide (Fig. 43 and Table II).

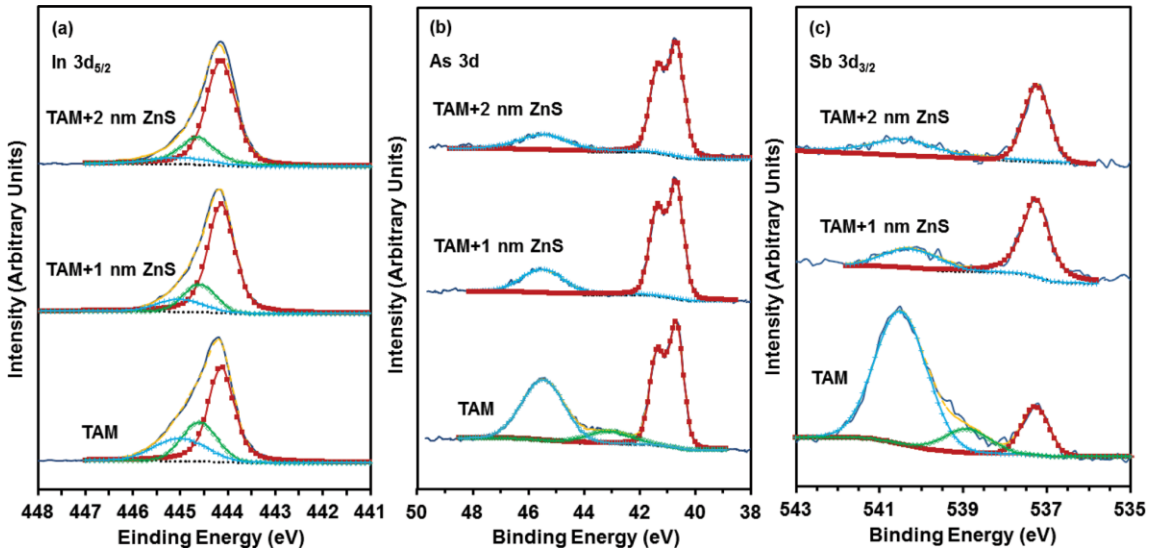

Figure. 44. (Color online) In $3d_{5/2}$ (a), As 3d (b), and Sb $3d_{3/2}$ (c) core scans of TAM-treated InAs/GaSb surfaces (bottom) and InAs/GaSb surfaces passivated with 1 (middle) and 2 (top) nm-thick ZnS following TAM treatment. All samples were loaded into high vacuum XPS chamber after 14 days of exposure to atmospheric air. XPS spectra were collected at 90 º take-off angle. Other ALD conditions are the same as those in Fig. 39.

			Intensity percentage (%)					
			Fresh passivation			After 14 days		
Peak	Component	Binding energy (eV)	TAM	TAM + 1 nm ZnS	TAM + 2 nm ZnS	TAM	TAM + 1 nm ZnS	TAM + 2 nm ZnS
In $3d_{5/2}$	In–As/Sb	444.1	91	72	68	61	74	76
	In–S	444.7	9	28	32	24	18	20
	In–O	445.0	0	0	0	15	8	4
As 3d	As–In	40.7	85	100	100	64	84	89
	As–S	42.9	15	0	0	6	0	0
	As–O	45.7	0	0	0	30	16	11
Sb $3d_{3/2}$	Sb–In	537.3	37	100	100	24	79	83
	Sb–S	538.8	63	0	0	11	0	0
	Sb–O	540.0	0	0	0	65	21	17

Table II. XPS results of passivated InAs/GaSb substrates immediately following treatment and after 14 days of exposure to atmospheric air.

b. Evolution of passivated InAs/GaSb surfaces in atmospheric air

To study the stability of chemical surface passivation over time and to investigate the effect of thicknesses on the related chemical passivation efficacy, the same samples (i.e., TAM-treated InAs/GaSb and TAM-treated InAs/GaSb capped with 1 and 2 nm-thick ALD ZnS) were left in the cleanroom atmosphere for 14 days exposed to atmospheric air before repeat XPS measurements were carried out.

In Fig. 44, new peaks centered at the higher binding energies of 445 for In (a), 45.7 for As (b), and 540 eV for Sb (c) are observed in the spectra of samples with and without a ZnS passivating film; they are indicative of the appearance of oxides resulting from the substrate oxidation by air. However, when compared to the TAM-treated sample [bottom graphs of Figs. 44(a)–44(c)], the TAM-treated InAs/GaSb with 1 nm-thick ZnS capping layer shows significantly less intense presence of oxides peaks (middle graphs of Figs. 44(a)–44(c) and Table II); this shows that 1 nm-thick ZnS significantly reduces the formation of oxides at the interface of the ZnS/TAM-treated InAs/GaSb substrates.

The dependence of passivation efficacy with the thickness of the capping film was studied with a thicker ZnS nanofilm on TAM-treated surfaces [top graphs of Figs. 44(a)–44(c)]. Comparisons between the XP spectra of TAM-treated samples passivated with 1 nm-thick ZnS and TAM-treated samples passivated with 2 nm-thick ZnS show noticeable reduction of all oxide features with increasing thickness of the ZnS film (Fig. 44, top and middle, and Table II); these show that the chemical stability of the passivated InAs/GaSb surfaces is dependent on the thickness of encapsulating film at the nanometer length scale,

while the additional passivation efficacy is not proportionate to the capping nanofilm thickness. The formation of oxides after passivation is likely due to the oxygen diffusion through the ultrathin sulfide film coupled with the interfacial chemistry; the thicker passivation film would extend the pathway for the diffusion of oxygen; thus reducing the formation of oxides during the long-term exposure to air investigated in this work.

E. Structure and surface morphology of as-deposited ZnS on TAM-treated GaSb(100)

The microstructure of encapsulating material is likely important in determining the long term chemical passivation of GaSb-based substrates. The structure of as-deposited ZnS nanofilms was investigated with GIXRD. Figure 45 shows the GIXRD pattern of 30 nm-thick ZnS film deposited on TAM treated GaSb at 200 ℃. The absence of crystalline peaks in the range of 25–45 °shows the amorphous structure of the resulting film. The surface morphology of thin films is also important in determining its physical characteristics. The surface morphology of as-deposited 30 nm-thick ZnS films was studied using the PSI mode of an optical surface profiler. PSI is a noncontact surface profilometry based on the interference of light to produce high-precision images of surfaces. Figure 46 shows the PSI image of ZnS film deposited at 200 ℃. The image of the resulting film manifests a smooth surface with a root mean square (rms) roughness of 0.71 nm.

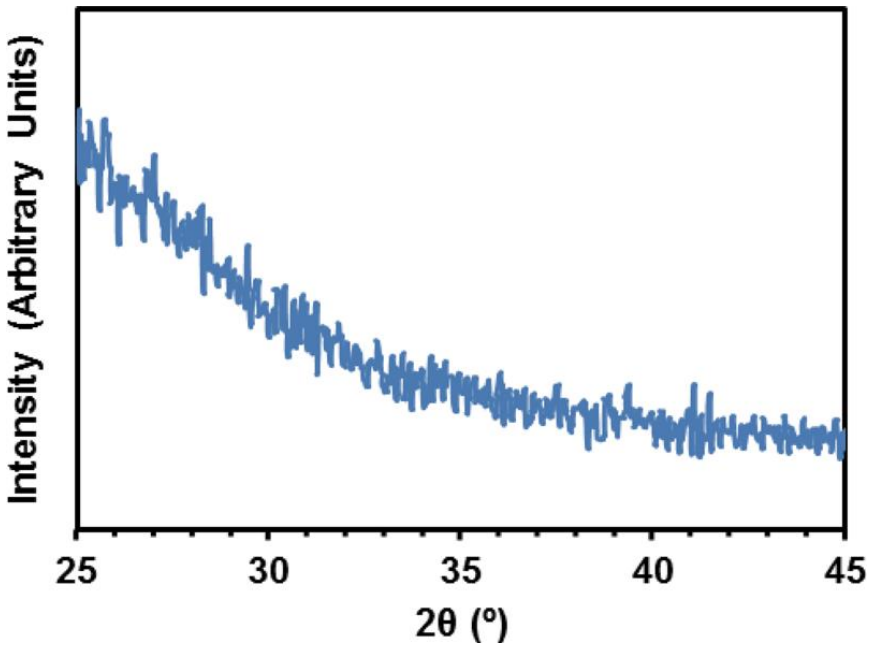

Figure 45. (Color online) GIXRD pattern of 30 nm-thick ZnS deposited on TAM-treated GaSb substrate at 200 ℃. Other ALD conditions are the same as those in Fig. 39.

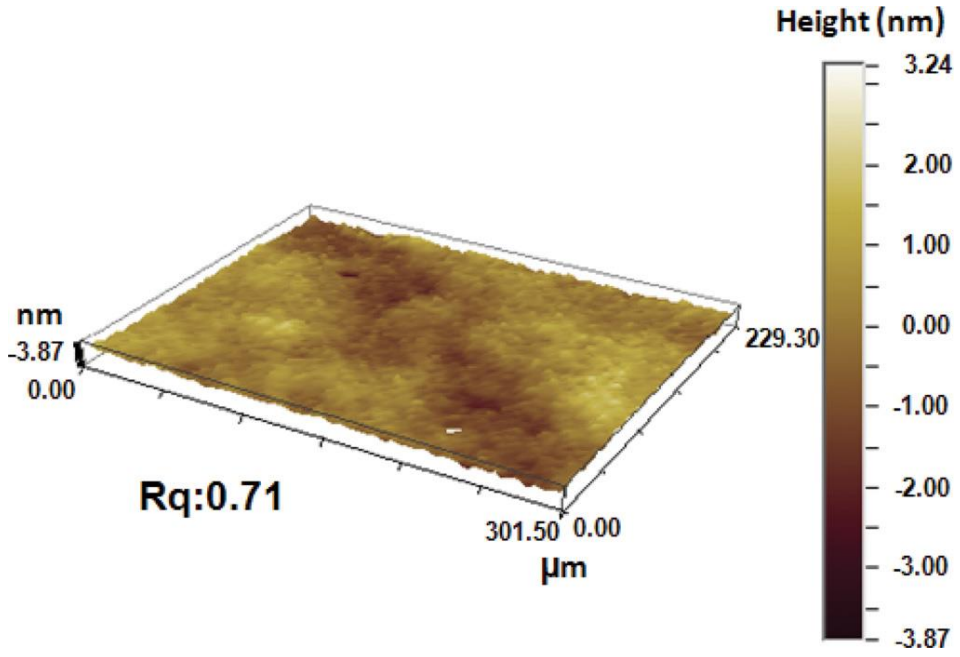

Figure 46. (Color online) PSI image of 30 nm-thick ZnS deposited on TAM-treated GaSb substrate at 200 ℃. Other ALD conditions were the same as those in Fig. 39.

4.3.4. Summary

ALD ZnS thin films were deposited on TAM-treated p-type GaSb-based substrates for the chemical passivation of GaSb-based surfaces. Linear growth behavior from the early stages of the ALD of ZnS was found. XPS data and elemental quantitative analyses of as-deposited ZnS films showed the resulting films to be stoichiometric with no evidence of other sulfur species such as elemental sulfur (164.0 eV), chemisorbed SO_2^{2-} (163–165.5 eV), sulfite SO_3^{2-} (166.4 eV), or sulfate SO_4^{2-} (168–170 eV). XPS studies of passivated GaSb substrates showed no elemental oxides could be found on the surfaces of TAM-treated GaSb and TAM-treated GaSb with a 1 nm-thick ZnS capping layer immediately following their corresponding processing. After samples were exposed to atmospheric air for 14 days, gallium and antimony oxides were found on both samples; the presence of these oxides on the ZnS capped TAM-treated GaSb; however, was found to be noticeably lower than that of samples treated only with TAM. This suggests that the 1 nm-thick ZnS chemical passivation film effectively reduced the extent of reoxidation of GaSb-based substrates in atmospheric air.

In addition, ZnS passivation film was used to enhance the chemical surface passivation of TAM-treated InAs/GaSb structures. The thicker ZnS film, i.e., 2 nm-thick, was found to provide a more effective protection against oxidation when exposed to atmospheric air; in fact, the observed increased chemical passivation effectiveness of GaSb-based surfaces with thicker ALD ZnS nanofilms suggests that oxygen diffusion through the ZnS nanofilms coupled with interfacial reaction engineering is the dominant process of GaSb-based substrate reoxidation. Also, the structure of 30 nm-thick ZnS

deposited on TAM-treated GaSb was investigated with GIXRD and it was found to be amorphous with a small rms.

4.4. Growth Characteristics and Properties of Yttrium Oxide Thin Films by Atomic Layer Deposition from Novel $Y(iPrCp)_3$ Precursor and O_3

4.4.1. Introduction

Yttrium oxide (Y_2O_3) is attractive for serving a wide range of potential applications due to its high melting point (~2439 ℃), good optical clarity (from 300 nm to ~ 11 μm), high refractive index (1.8), large band gap (~5.5 eV), and relatively high permittivity (i.e., 10-17) [146]. In particular, Y_2O_3 is important for enabling advanced electronics and electrochemical conversion devices, including complementary metal oxide semiconductor transistors [146], metal-insulator-metal capacitors [147], and solid oxide fuel cells [63]. In a recent study of MIM capacitors, Y_2O_3 served as an intermediate layer in a $TiO_2/Y_2O_3/TaN$ structure, which offered a high dielectric electrode band offset and possessed a high thermal stability against crystallization [147]. Also, Y_2O_3 has been investigated as a structural stabilizer in ZrO_2 thin films (80 nm-thick) and indeed enhanced oxygen ion conductivity of intermediate temperature SOFC [63].

In earlier studies, the deposition of Y_2O_3 has been investigated with several techniques, such as sputtering [147], molecular beam epitaxy [148], metal organic chemical vapor deposition [149], and atomic layer deposition [150, 151]. With recent developments in thin film technology, high quality films with functional nanostructures have attracted considerable interest in devices with 3-dimentional structures, such as SOFC with corrugated thin film electrolyte [63].

ALD is a powerful technique for deposition of various materials, including oxides, nitrides, metals, and sulfides. The self-limiting nature of ALD offers a wide range of possibilities and it meets challenging requirements, such as precise thickness control, excellent uniformity and conformality at all needed dimensions. In early ALD studies of Y_2O_3, the mainly employed yttrium precursor was tris(2,2,6,6, tetramethyl-3,5-heptanedione)yttrium, $Y(thd)_3$, and the growth rate was found to be ~ 0.02 nm/cycle [150]. For example, Gusev et al. have used $Y(thd)_3$ with ozone as oxidant and found that the resulting film has an oxygen-rich composition with a carbon content of 6% [151]. A higher growth rate (0.08 nm/cycle) was demonstrated by using tris(N,N'-disopropylacetamidinate)yttrium with water vapor as oxidant [146]. However, the resulting films were nonstoichiometric again. More recently, Cp ligand precursors, such as $Y(Cp)_3$, $Y(MeCp)_3$, and $Y(EtCp)_3$ were investigated with moisture oxidant and the resulting films were found to be stoichiometric with C content less than 0.5% [115, 152].

In the present work, a novel yttrium precursor with a melting point of 55 ℃, tris(isopropyl-cyclopentadienyl)yttrium [$Y(iPrCp)_3$], was used to deposit Y_2O_3 films on Si(100) substrate using a hybrid ALD/CVD reactor. The ALD growth characteristics were investigated and demonstrated by varying precursor dosage, reactor temperature, and number of deposition cycles. Upon optimization, a high growth rate of 0.17 ± 0.01 nm/cycle is achieved within the ALD window of 245 – 300 ℃. The resulting films are then analyzed using spectral ellipsometry and x-ray photoelectron spectroscopy (XPS), in order to determine stoichiometry, impurity, annealing behavior, and refractive index. The results of this work demonstrate the potential for introducing $Y(iPrCp)_3$ as a suitable

ALD precursor and Ar^+ beam as an effective means of removing surface $Y(OH)_3$ on Y_2O_3 films.

4.4.2. Experimentation

Y_2O_3 films were deposited using $Y(iPrCp)_3$ precursor and ozone as oxidant on P-type Si(100) substrates in a horizontal hot wall tubular ALD reactor. The reactor can be operated at a temperature up to 600 ℃ (custom-modified processing furnace, model 1043 Marshall, ThermCraft, Inc.). The base pressure of the ALD reactor was less than 20 mTorr. The oxidant was mixture of ozone and oxygen (1000 ppm ozone) generated with an oxygen (99.999% purity) flow through a UV lamp ozone generator. Argon (99.999% purity) was used as both precursor carrier gas and purge gas. The precursor bubbler was kept at 110 ℃, and the delivery line section from bubbler to reactor was maintained at 130 ℃. The depositions of Y_2O_3 films were carried out at a total pressure of 500 mTorr and studied in the temperature range of 200-350 ℃.

Prior to deposition, Si substrates were cleaned with a 1:1:5 $NH_4OH:H_2O_2:H_2O$ solution for 15 min to remove organic contaminants and particles, followed by 1% HF dip for 10 s (Radio Corporation of America standard cleaning, RCA SC-1). Each of these steps was followed by thorough deionized (DI) water rinse and drying by N_2 gas. This cleaning process was found to leave ~ 0.5 nm (as measured by ellipsometry) of native oxide on the substrate surface.

Thicknesses of as-deposited films were measured with spectral ellipsometry (J.A. Woollam Co., Inc., model M44). Post deposition annealing was carried out in a preheated quartz horizontal furnace (Lindberg Blue three-zone furnace) under N_2 atmosphere for 5 min between 600 and 800 ℃ at 1 atm. Chemical bonding and elemental analyses of Y_2O_3 films were probed with high resolution XPS (Kratos Analytical Ltd., Kratos AXIS-165) equipped with a monochromatic Al Kα (1486.6 eV) X-ray source operating at 15 kV and 10 mA. High resolution spectra were collected at a take-off angle 90 ° with pass energy of 20 eV, step size of 0.1 eV, and dwell time of 200 ms. The carbon 1s line (for hydrocarbon groups at 285 eV) was used to calibrate the binding-energy scale of all XPS spectra. Furthermore, Ar^+ beam sputtering, a gentle etching process, was carried out in XPS chamber to investigate the underlying composition of films.

4.4.3. Results and Discussion

A. Growth characteristics of Y_2O_3 thin films

Figure 47 shows the saturation curve for the deposition of Y_2O_3 using $Y(iPrCp)_3/O_3$ ALD process, studied at 270 ℃ with error bars representing standard deviation of film thickness across entire deposition area. During deposition, the amount of precursor dosage was controlled with the duration of the precursor pulse. The Ar gas purge time after $Y(iPrCp)_3$ pulse was fixed at 10 s. As seen, the growth rate of Y_2O_3 was found to initially increase with precursor pulse time and saturate after 7 s. Therefore, precursor pulse duration of 7 s is sufficient to achieve the maximum growth rate (0.17 ± 0.01 nm/cycle), whereas additional amount of precursor (resulting from longer pulse time) is effectively purged out of reactor prior to the oxidant pulse. This behavior indicates that

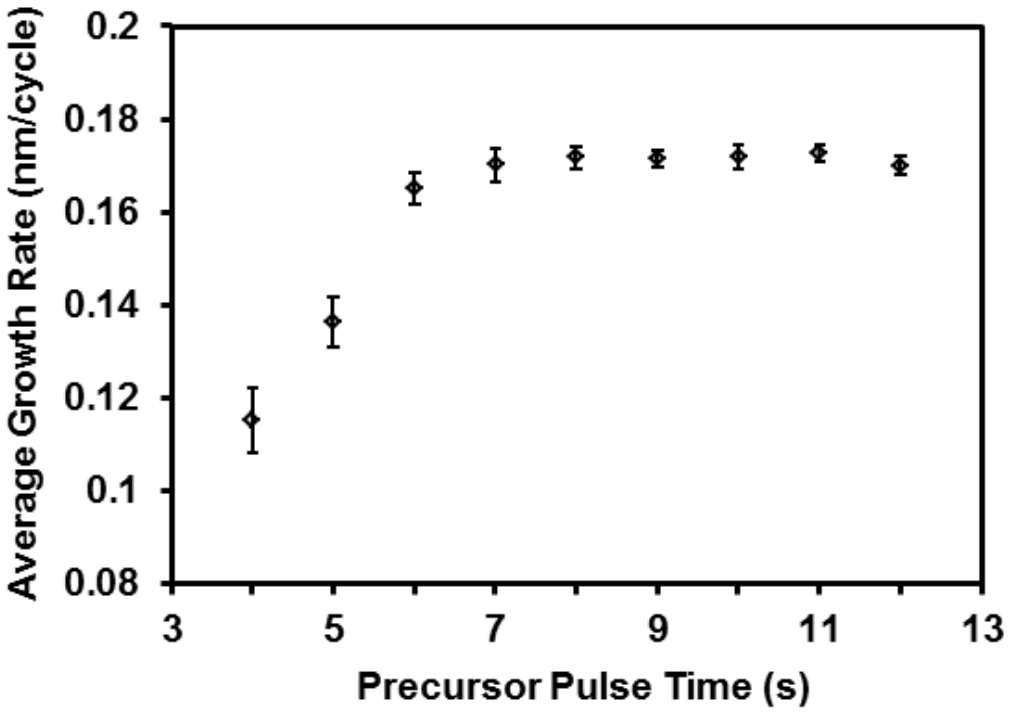

Figure 47. Growth rate of Y_2O_3 films on Si(100) substrates as a function of precursor pulse time at 270 ℃. The Y precursor was maintained at 110 ℃.

the $Y(iPrCp)_3/O_3$ ALD process in our system occurs through self-limiting growth kinetics. It is noted that the ozone concentration in here is at least two orders of magnitude lower than that typically used in ALD studies that include ozone as oxidant (e.g., (6)).

The deposition temperature dependence of growth rates is shown in Fig. 48. In there, all depositions were carried out with $Y(iPrCp)_3$ and O_3 pulse times of 9 and 1 s, respectively. Initially, relatively low growth rates are observed in the temperature region of 200 – 245 ℃, which is likely due to the insufficient deposition temperature impeding surface chemisorption and/or chemical reaction between the metal precursor and oxidant. On the other hand, the higher growth rates observed in the temperature region of 300 – 350 ℃ are typically attributed to thermal decomposition of multilayer precursors on the substrate. Compared with our earlier ALD study utilizing an $Y(EtCp)_3/H_2O$ process, a wider ALD temperature window in the range of 245 – 300 ℃ is observed with a growth rate of 0.17 ± 0.01 nm/cycle [115]. Figure 49 shows linear dependence of Y_2O_3 film thickness with the ALD cycle number. The apparent absence of incubation period at the early stage of ALD may be the result of the ultra-thin native oxide layer (~ 0.5 nm-thick) after the RCA-SC1 cleaning process.

B. Compositional analysis and Ar+ beam sputtering effect on removing surface $Y(OH)_3$

The chemical binding environment of as-deposited Y_2O_3 film was studied using high resolution XPS and shown in Fig. 50. As seen in the Y 3d core level spectrum of as-deposited film, a doublet peak at low binding energy of 157.2 eV with a spin-orbital

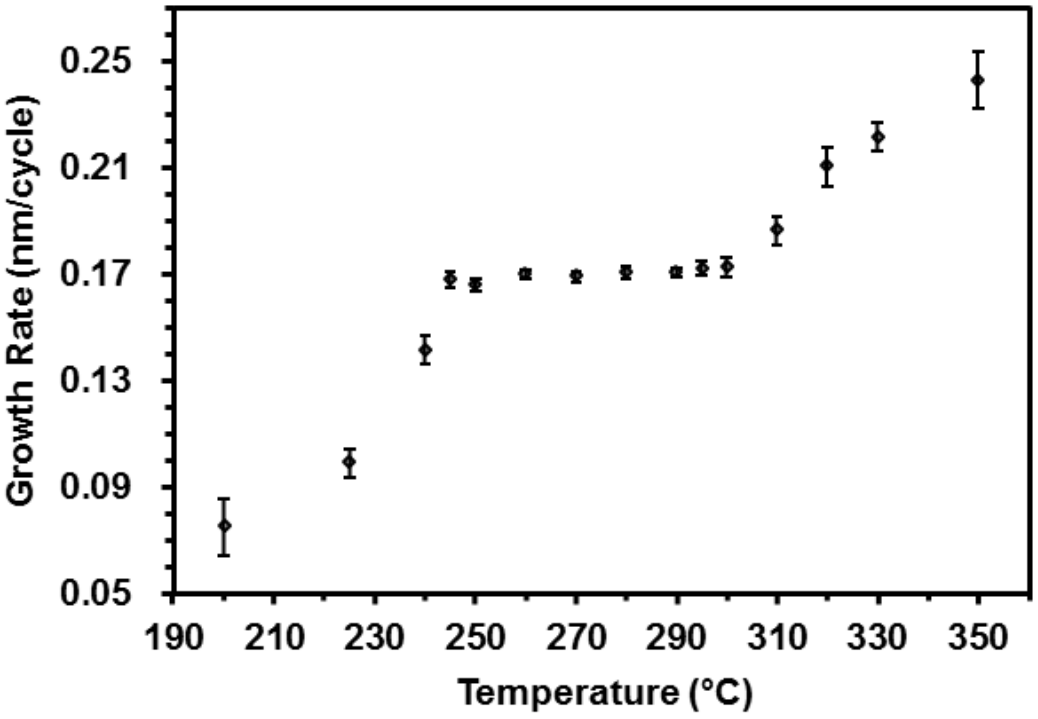

Figure 48. Y_2O_3 growth rate as a function of reactor temperature with 9 s $Y(iPrCp)_3$ pulse time. The other deposition conditions were the same as those in Fig. 47.

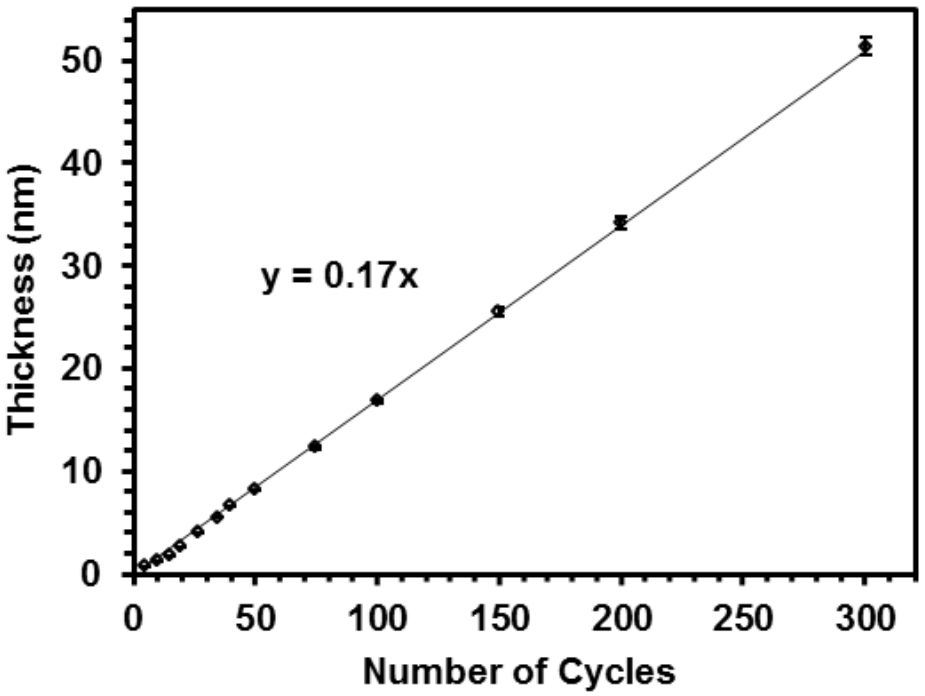

Figure 49. Thicknesses of Y_2O_3 as a function of ALD cycle number at 270 ℃. All other ALD conditions were the same as those in Fig. 48.

splitting (SOS) of 2.1 eV can be observed after deconvolution, and this is consistent with the signature peak of Y_2O_3 (Table III). The absence of any feature at 156 eV indicates no metallic Y is being incorporated into the film. However, the intense $Y3d_{5/2\text{-}3/2}$ peak fitted at 158.4 eV apparently demonstrates the formation of Y hydroxide on the film surface, possibly due to exposure to atmospheric ambient. The adsorption behavior of moisture on Y_2O_3 is not uncommon, because it has been reported that Y_2O_3 exhibits high reactivity toward water, inducing undesired $Y(OH)_3$ and adsorbs moisture on its surface [153]. The presence of Y hydroxide has also been observed with XPS in an earlier ALD study using $Y(iPr_2amd)_3/H_2O$ [146]. In our study, the formation of Y-OH in the as-deposited film is corroborated by O 1s spectrum, in which an intense Y-OH peak was deconvoluted into the 531.8 eV feature accompanied by a small peak at 533.1 eV for adsorbed moisture. Only a mall Y_2O_3 peak is fitted at 529.4 eV. Therefore, the surface of the as-deposited film consists of Y hydroxide and moisture. The atomic ratio of Y/O is found to be ~ 3.4.

In order to investigate the composition of the underlying Y_2O_3 film, Ar^+ beam sputtering was used and found to be an effective means of removing undesired surface species without sacrificing the bonding environment of Y_2O_3. The as-deposited Y_2O_3 film (14 nm-thick) was sputtered by 200 nA Ar^+ beam with varying duration from 0 to 50 min. As seen in the Y 3d spectra, the peak intensity of Y-OH is found to continuously decrease with increasing sputtering time, suggesting a reduced amount of Y hydroxide. On the contrary, the intensity of Y_2O_3 peak consistently increases with sputtering duration. During this process, within 20 min of sputtering, no new peak could be observed in the Y 3d spectra. This indicates that Ar^+ beam sputtering process can effectively reduce surface

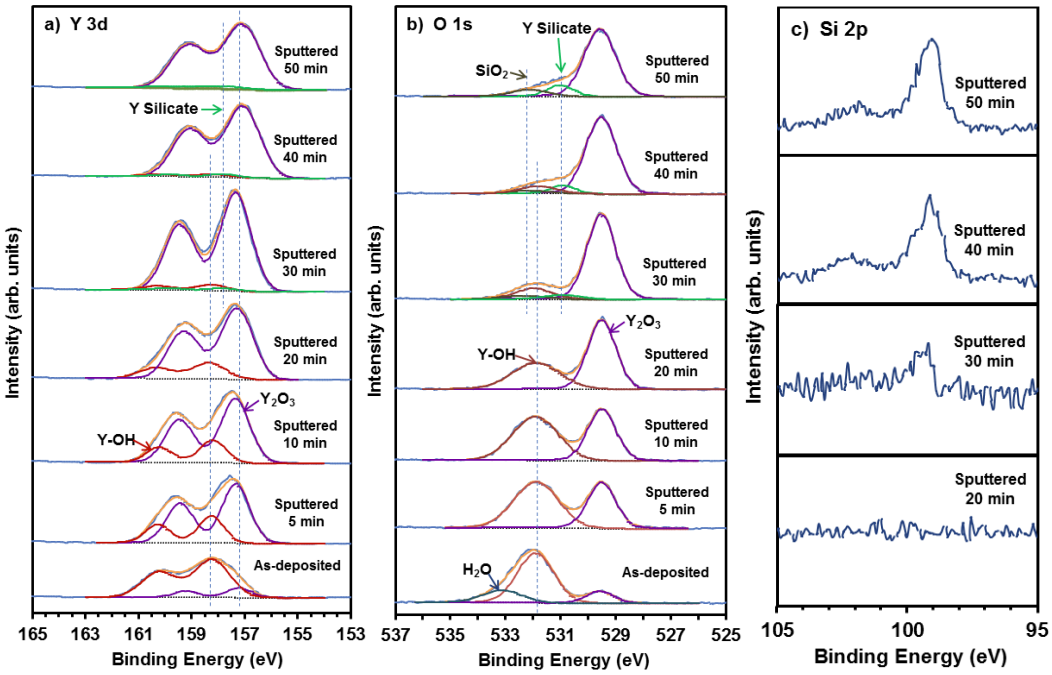

Figure 50. (Color line) Y 3d (a), O 1s (b), and Si 2p (c) core scans of 14 nm-thick as-deposited Y_2O_3 film before and after 200 nA Ar^+ beam sputtering. The film was deposited at 270 ℃; the gentle etching process was continuously carried out in the XPS chamber.

hydroxide of Y without forming suboxide or metallic Y (156.0 eV). After sputtering the surface for more than 30 min, a weak XPS feature appears at 157.8 eV accompanied by the presence of bulk Si peak at 99.3 eV in the Si 2p spectrum (Fig. 50c), which is apparently the result of the film thickness reduction throughout the sputtering process. Thus, the new feature located at 157.8 eV is attributed to Y silicate at the interface of the Y_2O_3/interface/Si system, in agreement with the interfacial study presented in the next section. Therefore, after 50 min sputtering, the Y_2O_3 binding state is observed to be the dominant one in the Y 3d spectrum with a trace amount of the Y silicate feature at 157.8 eV, whereas Y-OH is found to disappear.

The sputtering effect is indeed corroborated by the O 1s spectra. As seen in Fig. 50(b), surface moisture is sufficiently removed after 5 min of Ar^+ sputtering, and the Y-OH peak is seen to vanish in the O 1s spectrum after 50 min of sputtering. The presence of Y silicate and SiO_2 is consistent with the presence of bulk Si underneath the ALD film (Fig. 50c). Elemental composition with different sputtering duration was investigated using XPS peak fitting and shown in Fig 51. The atomic ratio of O/Y is found to decrease with increasing sputtering time. After sputtering for 50 min, the ratio of O/Y is found to be close to stoichiometric Y_2O_3. The sputtering effect on surface C contaminants is also shown in Fig. 52. After sputtering, the carbon content is lower than XPS detectable level, which is estimated to be less than 1 atom %. Thus, XPS analyses of as-deposited Y_2O_3 film indicate the underlying film is stoichiometric. Moreover, Ar^+ beam sputtering is an effective means of removing surface carbon contaminants and Y hydroxide. No suboxide and metallic Y are found after sputtering.

	Y $3d_{5/2}$ (eV)	Y $3d_{3/2}$ (eV)	O 1s (eV)	Si 2p (eV)
Y_2O_3	157.2	159.3	529.4	---
Y-OH	158.4	160.5	531.8	---
Y silicate	157.8	159.9	530.9	102.1
SiO_2	---	---	532.2	103.3
H_2O	---	---	533.2	---

Table III. Photoelectron binding energies of Y 3d, O 1s, and Si 2p peaks.

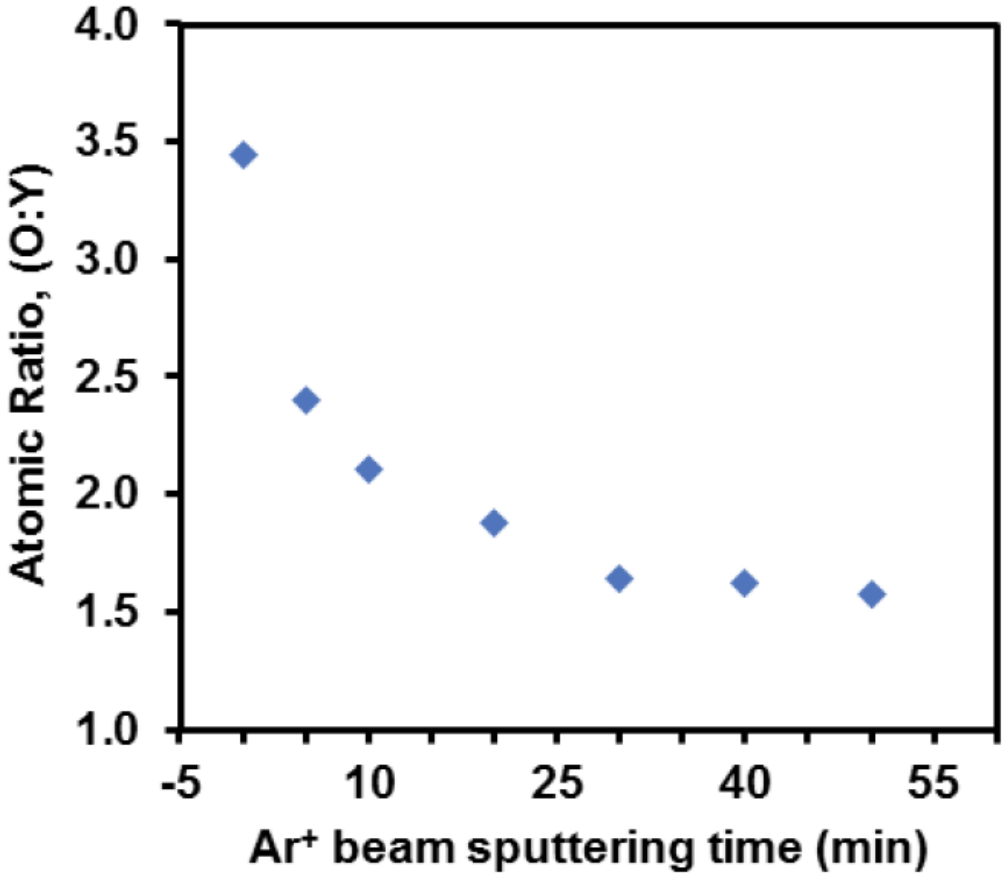

Figure 51. Atomic ratio of O/Y as a function of Ar+ beam sputtering duration. The sputtering was operated at 4 kV.

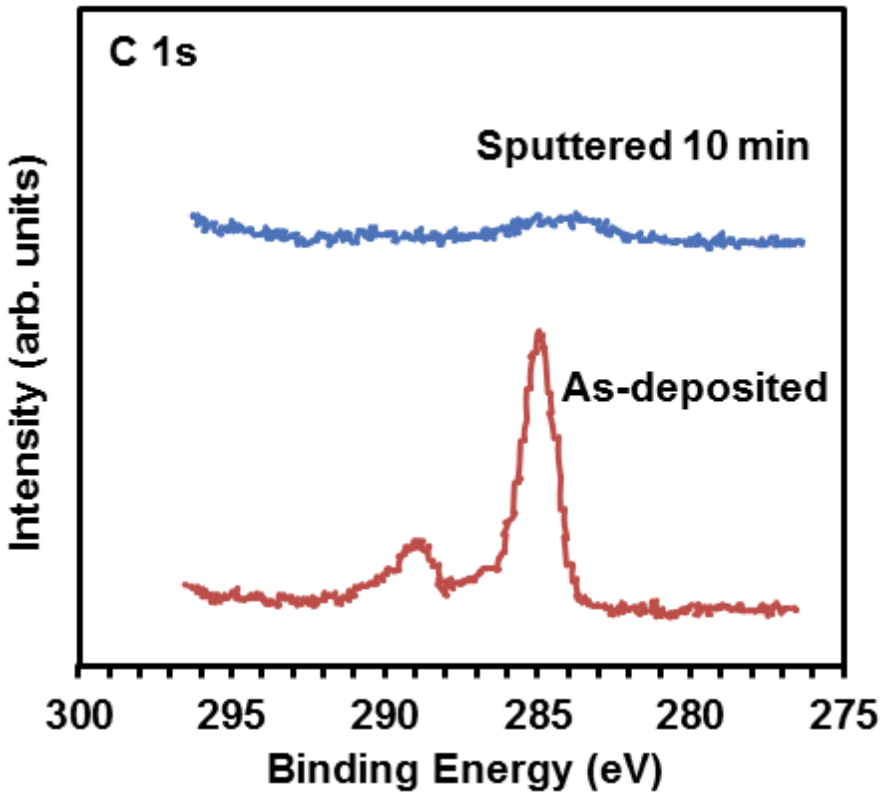

Figure 52. Sputtering effect on removing surface carbon contaminants. The Ar^+ beam sputtering conditions are the same as those in Fig. 51.

C. Annealing behavior at interface

The chemical stability of the thin film in contact with Si is important for metal-insulator- semiconductor and SOFC devices. In this study, the thermal behavior of Y_2O_3 film on a Si substrate was therefore investigated using XPS and shown in Fig. 53. For the structure of as-deposited Y_2O_3 on Si, two symmetric peaks were observed at 102.1 and 103.3 eV assigned to Y silicate and SiO_2, respectively. Thus, the interface is found to be a mixture of Y silicate and SiO_2 after deposition using our $Y(iPrCp)_3/O_3$ ALD process. Upon annealing in nitrogen, the peak intensities of Y silicate and SiO_2 are observed to continuously increase with annealing temperature, indicating increased formation of these species at the interface. This annealing behavior could be explained with interdiffusion between Y_2O_3 and the Si substrate and/or the high reduction tendency of SiO_2 by Y [154]. Such an increased formation of interfacial species seems to be in agreement with an earlier study on the interface of Y_2O_3/Y silicate/Si resulting from Y metal on chemical silicon oxide being annealed in O_2 [154].

D. Refractive index studies

The high refractive index of Y_2O_3 enables its optical applications, such as optical waveguides. The index of refraction is dependent on deposition route and thermal processing. In this study, refractive index measurements were carried out on both as-deposited and annealed Y_2O_3 films deposited with our $Y(iPrCp)_3/O_3$ ALD process.

The refractive index value of all films is consistent over the wavelength range investigated from 400 to 750 nm. As seen in Fig. 54, the refractive index is dependent on

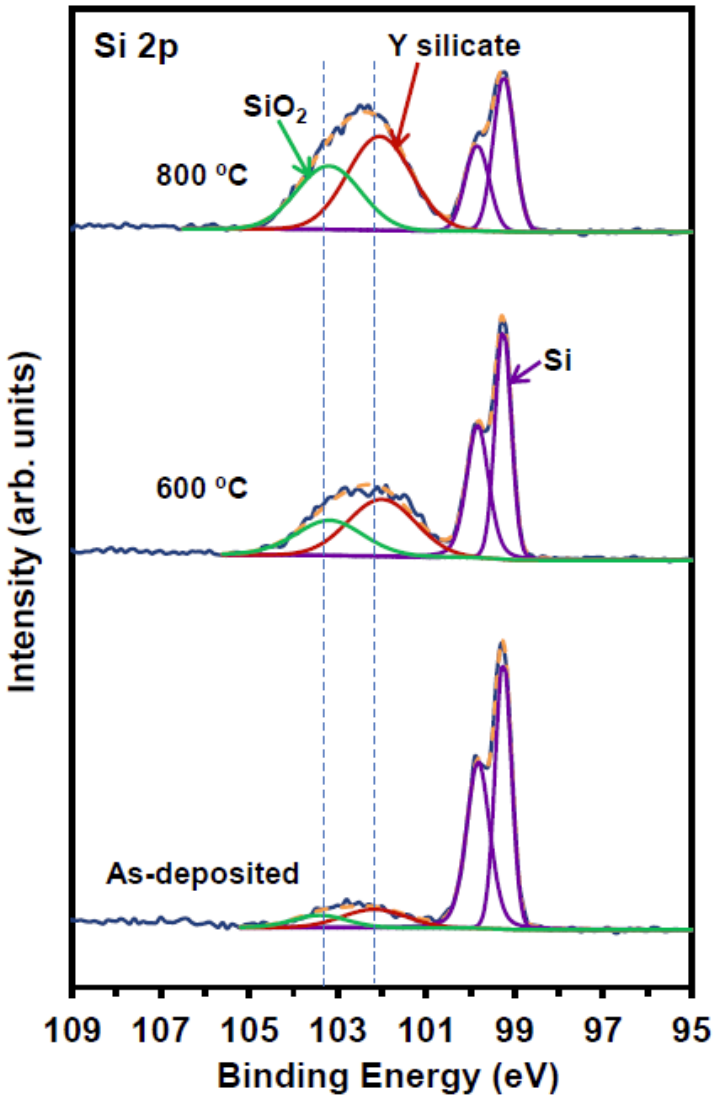

Figure 53. Annealing behavior of Y_2O_3 and Si interface. The annealing process was carried out at 600 and 800 ℃ in N_2 atmosphere for 5 min. The thickness of films is 3.5 nm.

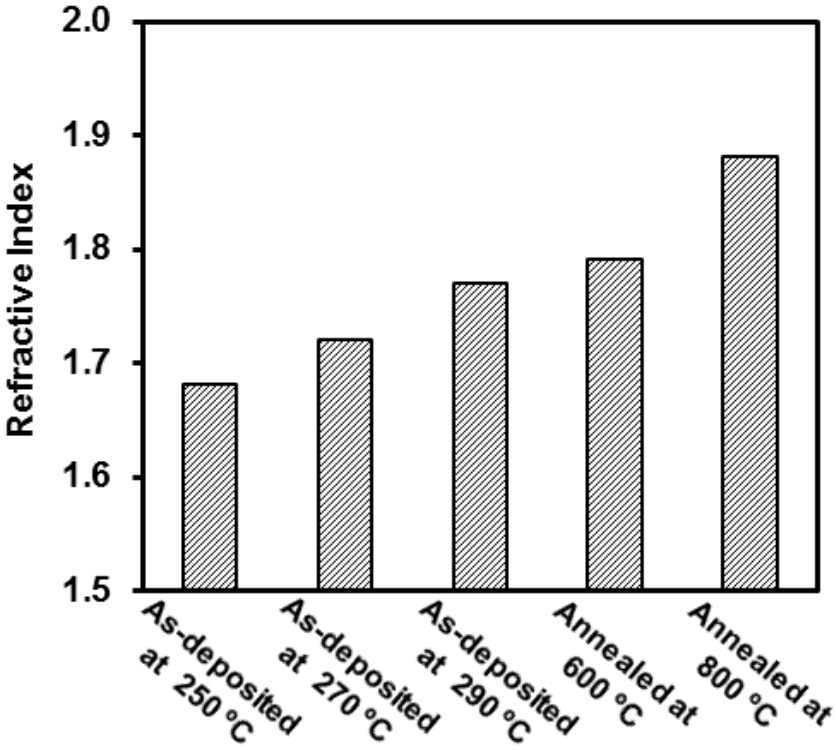

Figure 54. Refractive index of as-deposited and annealed Y_2O_3 films. Refractive index was measured at wavelengths from 400 to 750 nm.

the deposition and post-deposition processing temperatures. The refractive index values of as-deposited films are found to continuously increase with deposition temperature in the entire ALD window. The highest refractive index value of as-deposited film is found to be 1.77, which is less than 1.9 of bulk Y_2O_3. Moreover, it has been reported that high temperature annealing might enhance releasing of vacancies and movement of atoms thereby improving packing density and leading to higher refractive index [155]. Upon post deposition annealing of our samples, the refractive index of films annealed at 600 and 800 ℃ were found to be 1.79 and 1.88, respectively, which are slightly higher than that of films deposited through the $Y(iPr_2amd)_3/H_2O$ ALD process at 330 ℃ [146]. Further structural studies of Y_2O_3 deposited from $Y(iPrCp)_3/O_3$ process could be helpful in revealing the effect of structural changes on optical and electrical properties.

4.4.4. Summary

A novel ALD route for deposition of Y_2O_3 thin film was developed and demonstrated utilizing the $Y(iPrCp)_3/O_3$ process. The ALD growth characteristics were obtained by varying precursor dosage, reactor temperature, and number of deposition cycles. The growth rate of Y_2O_3 is found to be 0.17 ± 0.01 nm/cycle within the wide ALD temperature window of 245 - 300 ℃. The ozone concentration used is at least two orders of magnitude lower than that typically reported in the ALD of materials utilizing ozone as the oxidant. XPS analyses of as-deposited Y_2O_3 film indicate the underlying film to be stoichiometric. Ar^+ beam sputtering is used as an effective means of removing undesired surface carbon contaminants and Y hydroxide. No suboxide or metallic Y is present after post-deposition sputtering. An increased formation of interfacial species

between Y_2O_3 and Si is observed after post-deposition annealing. In addition, a high refractive index of ~1.9 is achieved after thermal processing at 800 ℃.

4.5. Atomic Layer Deposition and Characterizations of Yttria-doped Zirconia Ultra-thin Films

4.5.1. Introduction

Thin structure of yttria-stabilized zirconia is important for empowering a wide range of future devices, especially solid oxide fuel cells [59, 156, 157]. Because, the doping of zirconia with yttria can induce a considerable amount of oxygen vacancies while simultaneously enhancing the film crystallinity, which match the requirements for electrolyte in SOFCs, such as high oxygen ion conductivity as well as good thermal stability [30, 59]. So far, 8 mol% YSZ, as the state-of-the-art electrolyte material in SOFCs, has gained much interests and attentions [59]. However, YSZ films have been typically fabricated with physical deposition techniques in few tens of micron scale, and such thick films of YSZ require very high temperatures (e.g., 800-1000 ℃) for efficient O^{2-} transport due to its low ionic conductivity below 800 ℃ [32, 156]. The high operating temperatures often cause unnegligible thermal stresses, reduce cell lifetime, and restrict the potential use of SOFCs in low- and intermediate-temperature applications [30, 156]. Thereby, to overcome the drawbacks, one of the currently demanding challenges is enhancing the ionic conductivity of YSZ electrolyte in the low- and intermediate-temperature regimes by reducing the thickness of YSZ film without sacrificing electron leakage current [31].

Recently, the implementation of ultra-thin YSZ films, in nanometer scale, has been considered as an effective means of improving the ionic conductivity of electrolyte. Additional fabrication criteria, such as fully coverage of three-dimensional features, also

need to be satisfied for the enhancement in energy conversion efficiency of SOFCs [59]. Compared with physical deposition techniques, atomic layer deposition is a powerful deposition technique for producing highly dense ultra-thin films for all needed dimensions [38]. ALD is currently under investigation for the purpose of developing high efficient and low working temperature SOFCs [31]. YSZ as electrolyte material was first deposited with ALD on soda lime glass and silicon as well as Ni-YSZ cermet, and the mainly employed metal precursors were chloride, β-diketonates, and cyclopentadiene-ligand precursors with moisture and ozone as oxidant [61, 62]. Shim et al. reported a free-standing structure made use of 60 nm-thick ALD YSZ film sandwiched with 80 nm-thick sputtered Pt, which yielded a maximum power density of 270 mW/cm^2 at 350 ℃ due to its thin electrolyte [32]. More recently, Su et al. reported a three-dimensional free-standing structure, consisting of 70 nm-thick ALD YSZ as electrolyte and 120 nm-thick sputtered Pt as electrode, for low-temperature SOFC application, which showed an enhanced maximum power density of 677 mW/cm^2 at 400 ℃ [63]. Ultra-large free-standing structure, in cm scale, was achieved last year, by using ALD YSZ and 1.5 μm-thick Pt grid [64]. Decreasing the thickness of YSZ films to several tens of nanometers is therefore confirmed as an effective route for enhancing O^{2-} transport. However, it is of importance to further understand the compromising of electrolyte thickness, leakage current, and working temperature, which can be applied for optimizing the construction and working conditions of SOFCs.

In this study, a new ALD route for YSZ film is first demonstrated by utilizing cyclopentadiene-ligand metal precursors and ozone. The composition tenability and

chemical binding environment as well as crystal structure of resulting YSZ structures were extensively investigated with high-resolution x-ray photoelectron spectroscopy and glancing incident x-ray diffraction. In addition, this work will present the dependence of the electrical leakage behavior of YSZ nanofilms on its thicknesses and working temperatures.

4.5.2. Experimentation

Y_2O_3 and ZrO_2 thin films are deposited using tris(isopropylcyclopentadienyl) yttrium [$(iPrCp)_3Y$], and cyclopentadienyltris(dimethylamido) zirconium [$CpZr(NMe_2)_3$] respectively, with ozone (1000 ppm) as oxidant. The deposition is carried out at 500 mtorr in a horizontal hot wall tubular ALD reactor. The base pressure of the ALD reactor is less than 20 mTorr. Argon (99.999% purity) is used as both carrier gas for devilering metal precursors and purge gas for cleaning reactor chamber. The precursor bubblers are kept at 50 ℃ for $CpZr(NMe_2)_3$ and 110 ℃ for $(iPrCp)_3Y$, while the delivery line section from the bubbler to the reactor is maintained 20-30 ℃ higher than bubblers to prevent condensation of precursors during delivery.

Thin films are deposited on p-type Si (100) substrates (15 mm × 20 mm). Prior to deposition, Si (100) substrates are cleaned with a 1:1:5 $NH_4OH:H_2O_2:H_2O$ solution for 15 min to remove organic contaminants and particles, followed by 1% HF dip for 10 s. Each of the steps is followed by thorough rinsing in deionized (DI) water and drying by N_2 gas. This cleaning is found to leave ~0.7 nm (as measured by ellipsometer) of native oxide on the silicon substrate surface.

Thicknesses of as-deposited films are measured with a spectral ellipsometer (model M44, J.A. Woollam Co., Inc.); for each thickness determination, three measurements across the entire deposition area are performed with mean values representing film thickness and standard deviation indicating thickness variation. Chemical bonding states of resulting films are probed with a high resolution XPS (Kratos AXIS-165, Kratos Analytical Ltd.) equipped with a monochromatic Al Kα (1486.6 eV) X-ray source operating at 15 kV and 10 mA. XPS spectra of the elements-of-interest are collected using pass energy of 20 eV, step size of 0.1 eV, and dwell time of 200 ms. The Carbon 1s line at 285 eV is used to calibrate the binding energy scale of the XPS spectra. The analyses of XPS spectra are performed through XPS spectral peak-fitting, where peaks are subtracted from Shirley-type backgrounds and deconvoluted using Gaussian-Lorentzian peak shape functions.

An x-ray diffractometer (X'pert, PANalytical B.N. Co.) is used to obtain glancing incidence x-ray diffraction (GIXRD) patterns of as-deposited and RTP-treated films. The overall diffraction angle (2θ) resolution is 0.15 º. GIXRD diffractograms are collected at an incident angle of 1 ºto enhance diffraction sensitivity within the film and to minimize interference from the single crystal Si (100) substrate. The crystalline features are identified using the International Center for Diffraction Data (ICDD) database of diffraction pattern Powder Diffraction Files (PDF).

4.5.3. Results and Discussion

A. Growth behavior of Y_2O_3 and ZrO_2 thin films

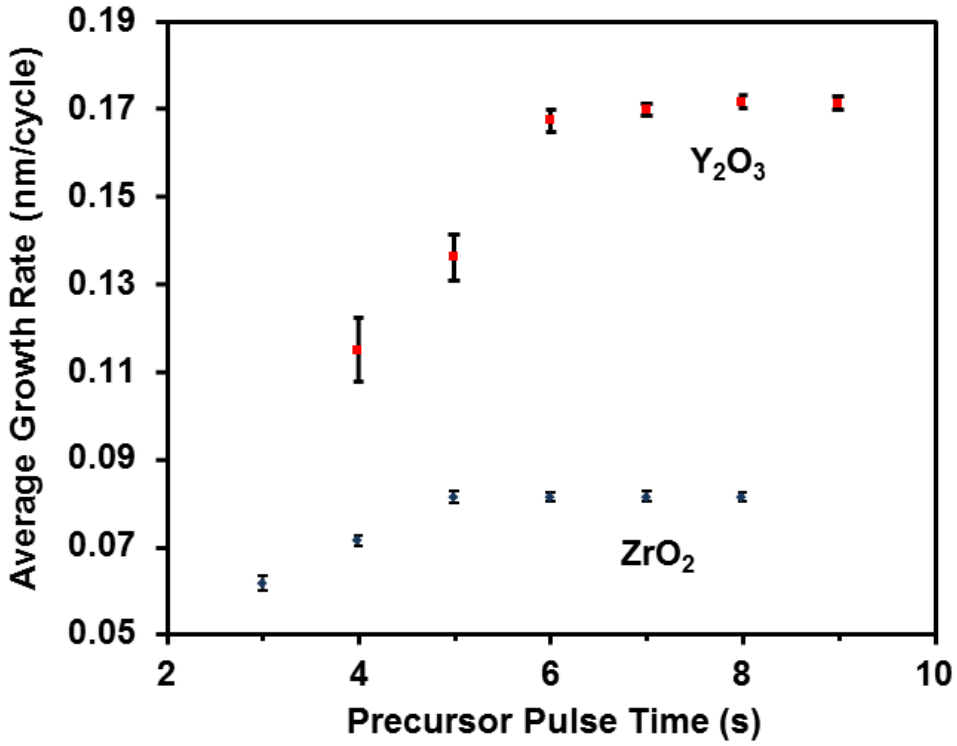

Figure 55. Growth rates of Y_2O_3 and ZrO_2 films on Si(100) substrates as a function of metal precursor pulse time at 270 ℃. The precursor bubblers are kept at 50 ℃ for $CpZr(NMe_2)_3$ and 110 ℃ for $(iPrCp)_3Y$.

Figure 55 shows the saturation curves for the deposition of Y_2O_3 and ZrO_2 using $Y(iPrCp)_3/O_3$ and $CpZr(NMe_2)_3/O_3$ ALD processes, respectively. The deposition processes are studied at 270 ℃ with error bars representing standard deviation of film thickness across entire deposition area. During deposition, the amount of precursor dosage is controlled with the duration of the precursor pulse. The Ar gas purge time is fixed at 10 s following $Y(iPrCp)_3$ or $CpZr(NMe_2)_3$ pulse. As seen, the growth rates are found to initially increase with precursor pulse time and saturate after 7 s for Y_2O_3 and 5 s for ZrO_2. Compared with Y_2O_3 ALD process, the slightly faster precursor saturation for ZrO_2 process is attributed to the nature of $CpZr(NMe_2)_3$, including a lower sublimation temperature and the combination of both alkylamido- and cyclopentadiengyl- ligands. The precursor pulse durations used are found to sufficiently achieve the maximum growth rate, 0.17 ± 0.01 nm/cycle for Y_2O_3 deposition and 0.081 ± 0.002 nm/cycle for ZrO_2, whereas additional amount of precursors can be effectively purged out of reactor prior to O_3 pulse. The saturation behavior indicates that both $Y(iPrCp)_3/O_3$ and $CpZr(NMe_2)_3/O_3$ ALD routes applied in our system occurs through self-limiting growth kinetics of ALD.

In the deposition of ternary thin films, a sufficient overlap of ALD temperature windows is desirable for constituent binary ALD processes; this overlap could effectively improve reproducibility and compositional tunability of resulting ternary films. Figure 56 shows the temperature dependence of growth rates of both Y_2O_3 and ZrO_2. Initially, in relatively low temperature region for each process, the low growth rates of Y_2O_3 could be attributed to the insufficient deposition temperatures impeding surface chemisorption

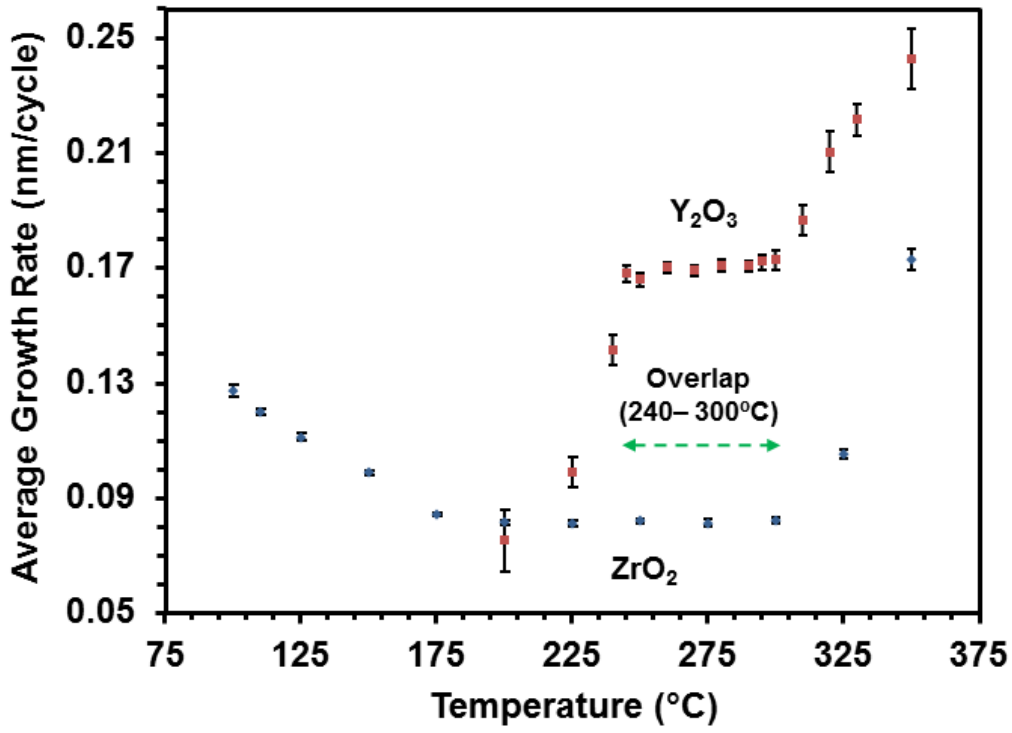

Figure 56. Dependence of growth rates of Y_2O_3 and ZrO_2 films on ALD reactor temperatures. Other ALD conditions were the same as those in Fig. 55.

and/or chemical reaction between $Y(iPrCp)_3$ and O_3, whereas the very high growth rate of ZrO_2 is most likely due to the multilayer condensation of $CpZr(NMe_2)_3$. In the relatively high temperature region, the rapid increase in the growth rates are observed for both Y_2O_3 and ZrO_2 processes; these indicate a non self-limiting growth behavior resulting from precursor decomposition during precursor pulsing. The temperature region where the growth rate is found to be independent of deposition temperature is taken as the ALD temperature window for each oxide deposition process. In contrast to the finding of ZrO_2 ALD window in this study, an earlier ALD study of ZrO_2 showed slightly increasing growth rates in the temperature region of 250-300 ℃ using the same ALD process of $CpZr(NMe_2)_3/O_3$ [158]. In this system, a sufficiently overlapping temperature window of the binary oxide processes is found to be between 240 and 300 ℃, which, as a result, offers a suitable temperature range for co-depositing Y_2O_3 and ZrO_2. Therefore, the deposition temperature of each metal oxide as well as of YSZ films in this study is maintained within the overlapping temperature window (i.e., 270 ℃).

Figure 57 shows the dependence of film thicknesses of Y_2O_3 and ZrO_2 on the total number of ALD cycles, which corroborates the precise thickness control of self-limiting ALD processes. For the ALD processes used, linear regression analyses yield growth rates of 0.17 nm/cycle for Y_2O_3 and 0.081 nm/cycle for ZrO_2. The growth rate of Y_2O_3 is found to be the same as that of $Y(EtCp)_3/H_2O$ ALD process reported in our earlier ALD study in a different ALD reactor [115], but slightly higher than the growth rates of 0.16 nm/cycle for $Y(Cp)_3/H_2O$ process and 0.12 nm/cycle for $Y(MeCp)_3/H_2O$ process [152].

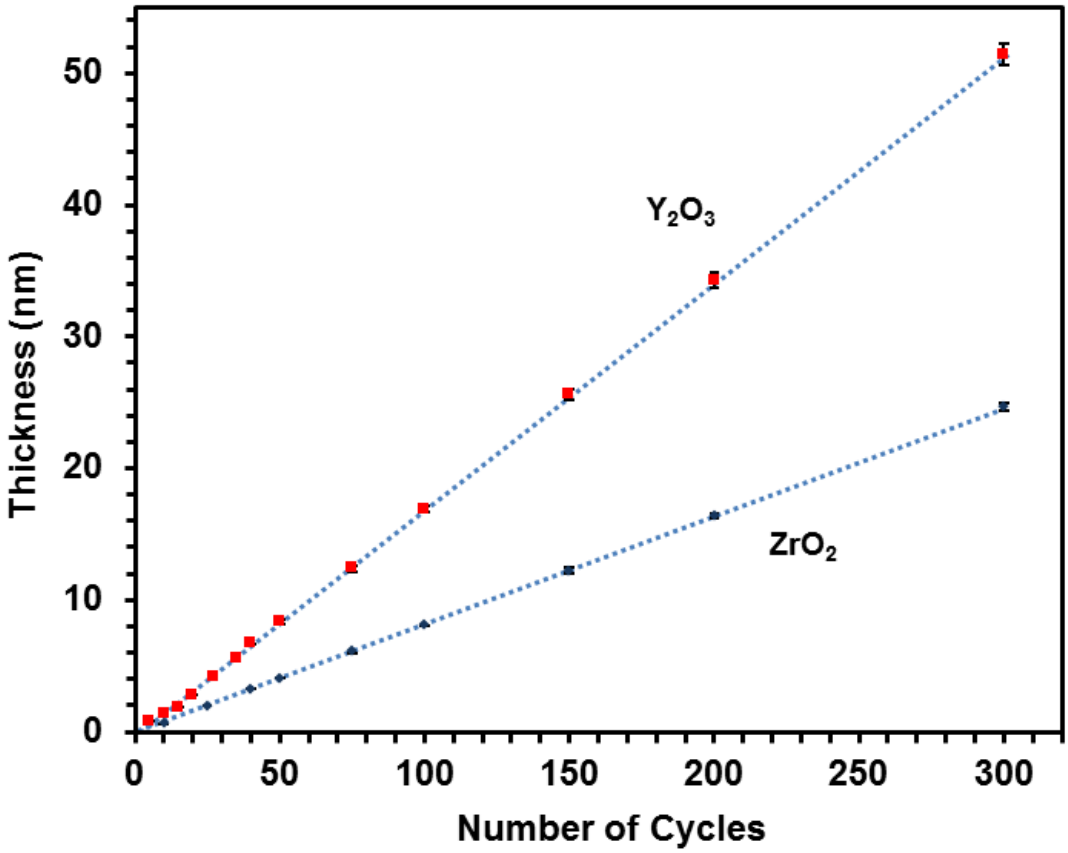

Figure 57. Thicknesses of Y_2O_3 and ZrO_2 films as functions of ALD cycle number. All films were deposited at 270 ℃. Other ALD conditions were the same as those in Fig. 56.

The growth rate of ZrO_2 films is consistent with that reported by Niinisto et al. using the same Zr precursor with ozone (4 mol% of ozone in oxygen) as oxidant at the deposition temperature of 270 ℃ [158]. The apparent absence of incubation period at the early stage of ALD could be the result of an ultra-thin native oxide layer (~ 0.7 nm-thick) on Si substrate after the RCA-SC1 cleaning process.

B. Composition tenability and chemical binding environment

To study the composition tunability of YSZ films deposited with the binary ALD processes of $Y(iPrCp)_3/O_3$ and $CpZr(NMe_2)_3/O_3$, a series of depositions is carried out by varying ALD cycle ratio (ALDCR, Y_2O_3/ZrO_2). For example, for a normalized cycle ratio $[Y_2O_3/(Y_2O_3+ZrO_2)]$ of 0.1, one cycle of Y_2O_3 deposition alternates with nine cycles of ZrO_2 deposition. Figure 58 shows the effect of normalized cycle ratio $[Y_2O_3/(Y_2O_3+ZrO_2)]$ on atomic composition [Y/(Y+Zr)] of 15 nm-thick as-deposited YSZ films, as determined from quantitative analyses of XPS spectra. The atomic ratio of Y/(Y+Zr) in YSZ films is found to monotonically increase linearly with increasing normalized cycle ratio $[Y_2O_3/(Y_2O_3+ZrO_2)]$. This shows that the Y content in the resulting films can be well controlled by varying the ALDCR of Y_2O_3 and ZrO_2. Similar effective tunability for atomic composition was also reported in our earlier ALD studies of other composite metal oxides, such as Y_2O_3-doped HfO_2 and Er_2O_3-doped TiO_2 [129, 159, 160].

The binding environment of YSZ films is investigated with high-resolution XPS. Figure 59 shows the XPS core level spectra of Y 3d and Zr 3d obtained from YSZ films

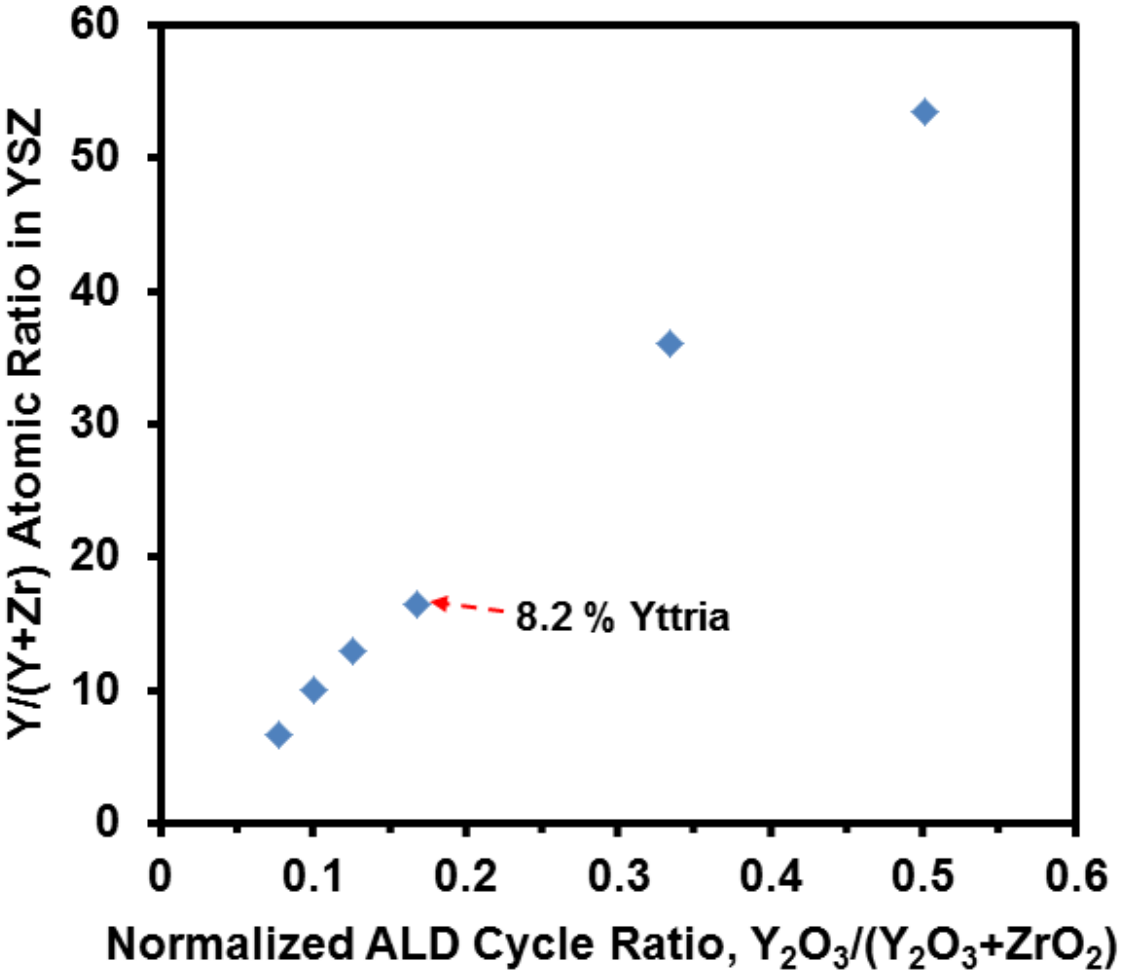

Figure 58. YSZ (15 nm-thick) film composition evaluated using XPS as a function of normalized cycle ratio of $Y_2O_3/(Y_2O_3+ZrO_2)$. Other ALD conditions were the same as those in Fig. 57.

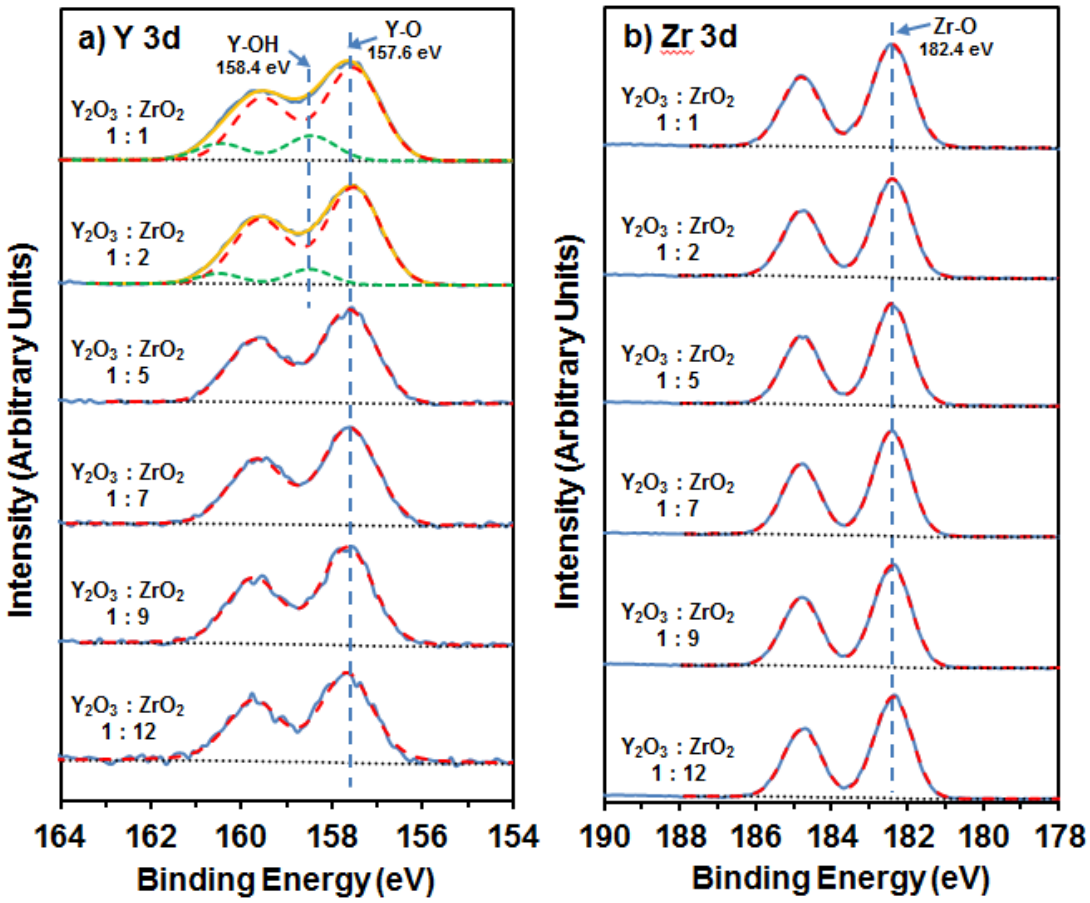

Figure 59. Y 3d (a) and Zr 3d (b) core level XP spectra of as-deposited 15 nm-thick YSZ films with variable ALDCR. The YSZ films are deposited at at 270 ℃ with ALDCR of 1:1, 1:2, 1:5, 1:7, 1:9, and 1:12. Other ALD conditions were the same as those in Fig. 57.

deposited with variable ALDCR from 1:1 to 1:12. As seen in the Y 3d core level spectrum (Fig. 59a) of YSZ film with ALDCR of 1:1, a doublet peak at low binding energy of 157.2 eV with a spin-orbital splitting (SOS) of 2.1 eV could be observed after deconvolution, which is the signature peak of Y_2O_3. The absence of any feature at 156 eV indicates that no metallic Y is being incorporated into the film. However, a small $Y3d_{5/2-3/2}$ peak fitted at 158.4 eV apparently demonstrates the formation of Y hydroxide on the film surface, due to the exposure of Y_2O_3 to atmospheric ambient. The finding of $Y(OH)_3$ confirms an earlier study, showing that Y_2O_3 exhibits high reactivity toward water and forms $Y(OH)_3$ and, as a result, adsorbs moisture on its surface [153]. However, $Y(OH)_3$ peak is found to rapid decrease in intensity with ALDCR decrease to 1:2. This indicates that the increased coverage of ZrO_2 on Y_2O_3 could reduce the formation of $Y(OH)_3$ by insulating Y_2O_3 from contacting with atmospheric moisture. As the ALDCR decrease, the disappearance of $Y(OH)_3$ in the YSZ films, deposited with ALDCR of 1:5 or lower, is observed and demonstrates two facts. On the one hand, $Y(iPrCp)_3/O_3$ ALD route produces pure stoichiometric Y_2O_3 without any formation of $Y(OH)_3$ in bulk film. On the other hand, atmospheric gaseous moisture can not penetrate and/or diffuse through 5 cycles of ZrO_2. This suggests that 5 cycles of ZrO_2 is beyond at least one monolayer and gas impenetrable, which meets one of the basic requirements for electrolyte in SOFCs. Figure 59(b) shows the core-level spectra of Zr 3d obtained from YSZ films deposited with variable ALDCR. The Zr 3d spectrum only consist of two peaks at 182.5 and 184.9eV for Zr $3d_{5/2}$ and $3d_{3/2}$, respectively, indicating the oxidization state of Zr^{4+} in all YSZ films without any other Zr compound.

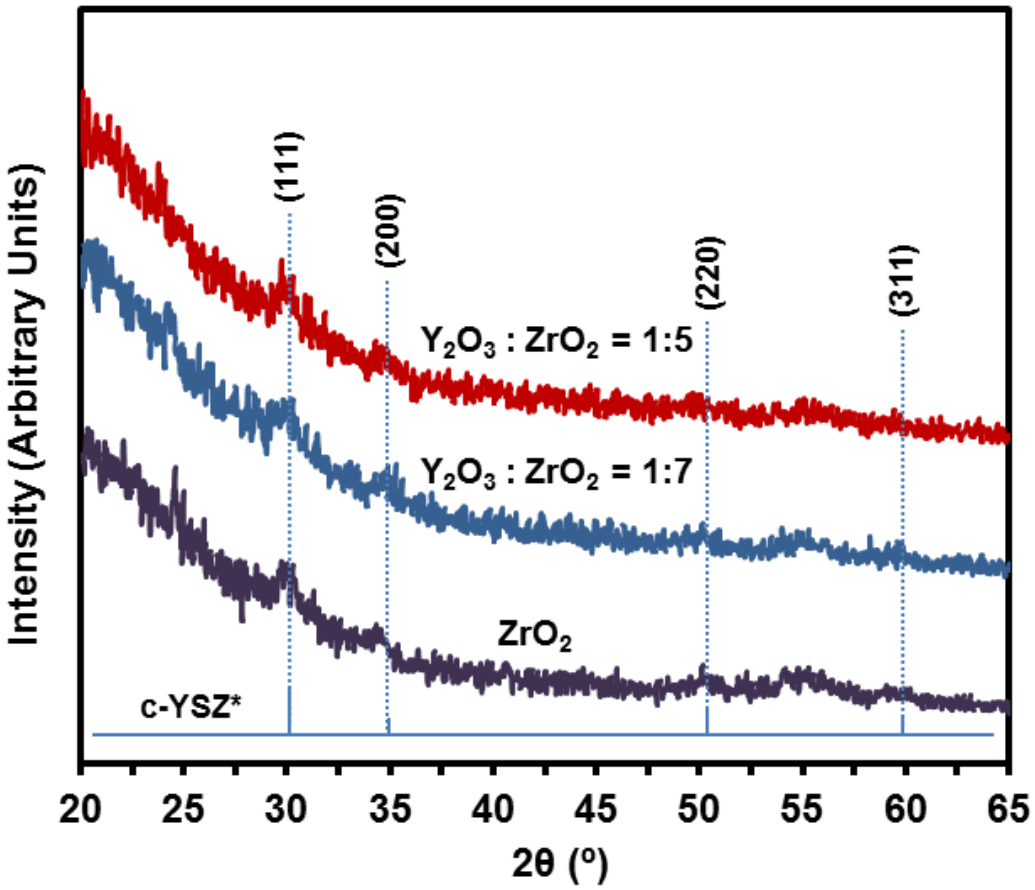

Figure 60. GIXRD patterns of as-deposited ZrO_2 and YSZ films with ALDCR of 1:5 and 1:7. GIXRD characterizations are collected at an incident angle of 1 º. All deposition and RTP treatment conditions are the same with those in Fig. 57. Cubic YSZ reference: International Centre for Diffraction Database, PDF Card No. 30-1468.

C. Effect of post-deposition annealing on the structure of YSZ films

Structure of thin films is important in determining their thermal stability and electrical properties for almost all SOFC applications. For example, during temperature variation, the changes in volume and electrical properties due to the phase transformations (e.g., monoclinic/tetragonal) often restrict the use of ZrO_2 in SOFCs [62]. Therefore, Y_2O_3 is required, as a structure stabilizer in ZrO_2, to maintain highly ion-conductive cubic structure during SOFCs operation. In the present study, YSZ films before and after post-deposition annealing are investigated using GIXRD, to determine the structure of films based on the ALD and annealing conditions used. All films were 40 nm-thick as measured with spectroscopic ellipsometry. The corresponding lattice structures of diffraction peaks are identified and labeled as indicated in Fig. 60 and 61.

Figure 60 shows the diffraction patterns of as-deposited ZrO_2 and YSZ films. All the films after deposition are found to be mostly amorphous with trace amount of diffraction features observed at ~30.1 and ~34.9 °in their XRD patterns, indicating the onsite of film crystallization during ALD at 270 ℃. Nam et al. reported that the ZrO_2 films deposited on Si(100) utilizing $ZrCl_2[N(SiMe_3)_2]_2/H_2O$ ALD process at 250 ℃ is amorphous due to the lack of any crystalline peak in its XRD pattern, which suggests a higher crystallization temperature base on their ALD condition used [161]. On the contrary, both cubic and monoclinic structures were observed in as-deposited ZrO_2 film grown with $Zr(NEtMe)_4/O_3$ ALD process at 275 ℃ [158]. For as-deposited YSZ films, a lower onset of YSZ crystallization temperature (e.g., 200 ℃) in the cubic phase was observed and reported by Shim et al. in the ALD study utilizing the $Zr(NMe_2)_4/H_2O$ and

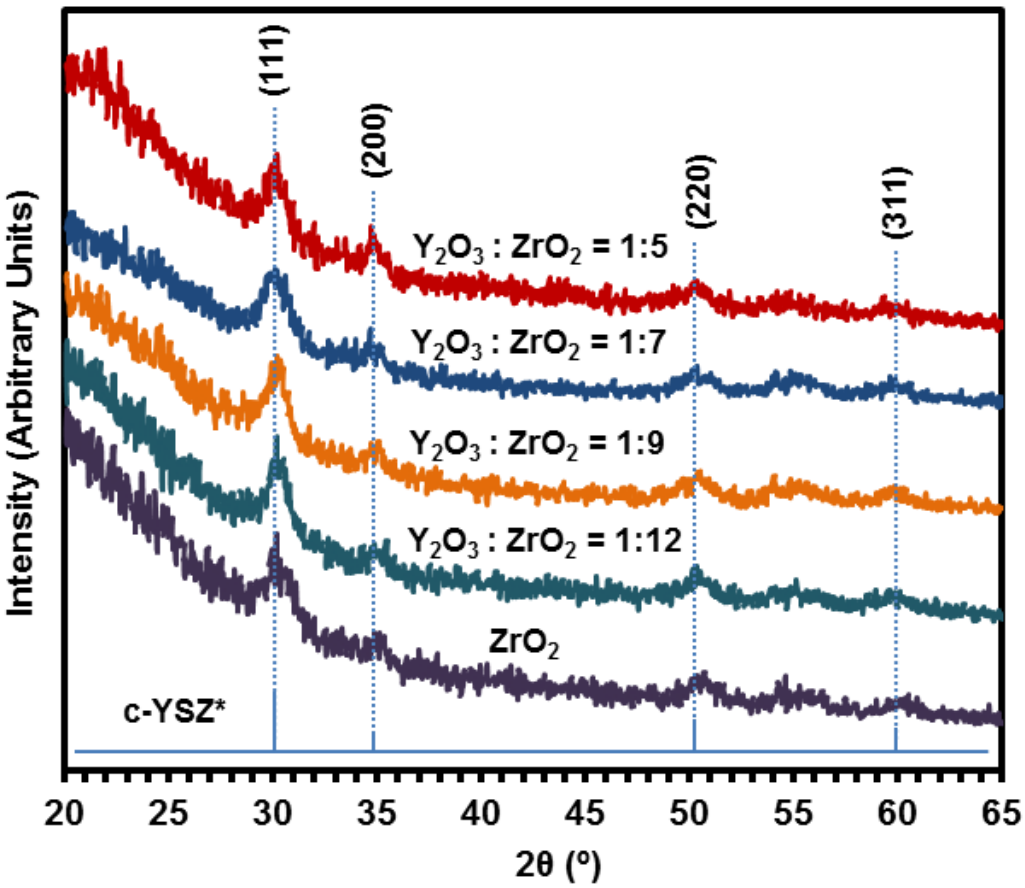

Figure 61. GIXRD patterns of post-deposition annealed ZrO_2 and YSZ films. The YSZ films are deposited at 270 ℃ with ALDCR of 1:1, 1:2, 1:5, 1:7, 1:9, and 1:12. All the films are post-deposition annealed at 800 ℃ in N_2 for 5 min. GIXRD characterizations are collected at an incident angle of 1°. All deposition and RTP treatment conditions are the same with those in Fig. 57. Cubic YSZ reference: International Centre for Diffraction Database, PDF Card No. 30-1468.

$Y(MeCp)_3/H_2O$ processes [32]. These indicate the precursor employed in ALD process could be an important contributing factor to the as-deposited film structure.

To investigate the effect of annealing on the structure of films, the as-deposited ZrO_2 and YSZ films are post-deposition annealed at 800 ℃ in N_2 for 5 min, and their diffraction patterns are shown in Fig. 61. After post-deposition annealing process, sharp increase in the intensity of diffraction peaks with (111) orientation at ~30.1 ° and (200) orientation at ~34.9 ° is observed, along with the appearance of features at ~50.2 and ~59.6 °that are assigned to (220) and (311) orientations, respectively; these are indicative of apparently cubic structure of both ZrO_2 and YSZ films after annealing. The average lattice constant (calibrated by Jade 9.0 software calculation of fitted peaks) is found to be about 0.5140 nm for post-deposition annealed YSZ films, which is closed to that of bulk YSZ (a = 0.5139 nm) formed with annealing of Y_2O_3 and ZrO_2 at 1400 ℃ for 6 days (International Centre for Diffraction Database, PDF Card No. 30-1468). The grain size of annealed YSZ films at 800 ℃ is 8.2 nm, calculated by applying Scherrer's relation to the XRD (111), (200) and (220) peaks. The formation of cubic structure without other crystalline structure in annealed ZrO_2 film is in agreement with an earlier study of ALD ZrO_2 annealed at the same temperature in Ar [161]. For annealed YSZ films, the absence of monoclinic and tetragonal peaks in its XRD patterns is, as expected, consistent with an earlier report of ALD YSZ films after post-deposition annealed at 800 ℃ [32]. This indeed corroborates that the incorporation of Y_2O_3 into ZrO_2 could effectively maintain the thermally stable cubic structure. As the higher intensity shown after post-deposition annealing, the crystallinity of YSZ films, in this study, is seemed to increase, which is in

contrast with the earlier study reporting that no significant change in crystallinity of YSZ films on Si_3N_4 after high-temperature annealing at 800 ℃ [32]. Therefore, in addition to ALD conditions used, the nature of substrate could be another possible factor influencing the structure of thin film during annealing.

4.5.4. Summary

$Y(iPrCp)_3$ and $CpZr(NMe_2)_3$ with O_3 are used for ALD of Y_2O_3, ZrO_2, and YSZ films on Si. The growth rates of Y_2O_3 and ZrO_2 with temperature-optimized ALD conditions are found to be 0.17 and 0.081 nm/cycle, respectively. A sufficient overlapping temperature window of $Y(iPrCp)_3/O_3$ and $CpZr(NMe_2)_3/O_3$ processes is obtained between 240 and 300 ℃. The atomic ratio of Y/(Y+Zr) in YSZ films is found to increase monotonically with increasing normalized cycle ratio of $Y_2O_3/(Y_2O_3+ZrO_2)$, showing excellent tunability of the YSZ film composition. 8 mol% Y_2O_3 stabilized ZrO_2 is approached with ALDCR of 1:5. Chemical binding environment analyses using surface sensitive XPS suggests that $Y(iPrCp)_3/O_3$ ALD route produces pure stoichiometric Y_2O_3, and YSZ films deposited with ALDCR of 1:5 can effectively prevent the formation of $Y(OH)_3$ during exposure in atmospheric air. The as-deposited ZrO_2 and YSZ films with variable ALDCR are found to be mostly amorphous as determined with GIXRD, suggesting the onset of film crystallization under the ALD conditions used. After annealing in N_2 at 800 ℃ for 5 min, the cubic structure is apparently observed in both ZrO_2 and YSZ films with (1 1 1) orientation dominance, and no other crystal structure could be found. The average lattice constant and grain size of post-deposition annealed YSZ films are found to be 0.5140 and 8.2 nm, respectively.

4.6. Nucleation Behavior-Morphology-Resistivity of Atomic Layer Deposited Pt on Yttria-Stabilized Zirconia Films

4.6.1. Introduction

Atomic layer deposited metals have attracted considerable interest for a wide range of applications, including microelectronics, catalysis, and renewable energy [31, 162, 163]. As the recent input of atomic layer deposition (ALD) in energy conversion, platinum is a highly desirable electrode material offering extremely low resistivity and high catalytic activity capable of sandwich nanostructure (i.e., Pt/yttria-stabilized zirconia (YSZ)/Pt) for intermediate-temperature solid oxide fuel cells (ITSOFCs) [59]. However, the Pt electrodes deposited on YSZ electrolyte must have an interconnected porous structure to allow gaseous fuel and oxidant to penetrate through the electrodes and efficiently contact the YSZ electrolyte. In this study, the nucleation behavior and resulting physical properties of ALD Pt are examined on different ALD YSZ films prepared within the same reactor as a potential means of controlling the nanodimensional morphology of thin ALD Pt structures (i.e., nanoparticles, porous or dense film) of importance in ITSOFCs.

ALD utilizes gas-solid chemisorption equilibria of precursors on substrate surface to achieve its unique self-limiting growth kinetics which crucially depends on the interaction between metal precursor and reactive species such as hydroxyl surface sites [38]. It is known that a polar, hydrophilic surface often offers reactive sites which enhance nucleation of ALD [164]. Thus, the surface properties of a substrate are important factors in determining the nucleation rate and morphology of the material being

deposited. So far, the common method of modifying the ALD nucleation behavior is through chemical routes, for example by controlling hydroxyl groups on substrate surfaces [165]. However, the chemical approach requires chemical handling ex-situ the process reactor [137], which may not be desirable for a chemically and/or physically sensitive substrate materials such as the oxide electrolyte in ITSOFCs. An alternate and more process-efficient approach to modify the nucleation behavior of an ALD process is based on the surface property optimization of a substrate by means of physical treatment, such as annealing or sputtering. In an earlier study, Pt has been atomic layer deposited on rf (radio frequency)-sputtered YSZ films for ITSOFC applications; the sputtering and ALD were done in two different systems [65]. The as-deposited Pt with a thickness of 10 nm was found to start coalescing on the rf-sputtered YSZ films, and 30 nm-thick ALD Pt was reported to show a continuous film [65]. The coalescent Pt structure was reported to exhibit a higher power density (50 mW/cm^2) at 350 ℃ which is most likely due to the nanoscale porosity of the Pt structure. However, there are little specifics on factors contributing to Pt nucleation behavior and resulting properties on the YSZ substrate. Thus, to explore the factors affecting nucleation and properties of ALD Pt on ALD YSZ surfaces, this study examines ALD Pt properties resulting from films on ALD YSZ with variable surface characteristics (i.e., hydrophilicity, roughness, and structure). The ALD nucleation is especially important in ALD Pt on ALD YSZ as it is necessary to evaluate optimization between desirable Pt film mesoporous morphology and efficient use of Pt metal, for example, in terms of fast nucleation. The use of ALD for all elements of an IT-SOFC also minimizes/eliminates possible contamination from sample transfer from one

system into another; such contamination is of paramount importance at the length scale of these SOFCs.

This work reports the influence of ALD YSZ properties, in terms of hydrophilicity, roughness, and structure on the nucleation behavior, morphology, and resistivity of ALD Pt. A simple thermal annealing strategy performed on ALD YSZ film is suggested to yield continuous mesoporous Pt film on YSZ desirable for ITSOFCs using minimal consumption of Pt metal.

4.6.2. Experimentation

Prior to ALD of Pt, 45 nm-thick YSZ films were first deposited on 2×2 cm^2 sections of Si(100) substrates (Resistivity: 1-10 Ω·cm) using a different ALD process but in the same reactor used for Pt ALD. The deposition of YSZ films was performed in a custom-designed, hot-wall, tubular ALD reactor at 270 ℃ capable of delivering multiple precursors to the reactor. The ALD was performed using tris(isopropyl-cyclopentadienyl)yttrium [$Y(iPrCp)_3$] as yttrium precursor, tris(dimethylamino)cyclopentadienyl zirconium [$ZrCp(NMe_2)_3$] as zirconium precursor, and ozone (1000 ppm O_3 in oxygen) as oxidant. Successive ALD cycle ratios were varied to control the Y:Zr atomic composition. For example, an ALD cycle ratio (i.e., Y_2O_3: ZrO_2) of 1:5 was applied to achieve 8 mol% of Yttria in all YSZ films. The composition of YSZ was determined with high-resolution x-ray photoelectron spectroscopy (Kratos AXIS-165, Kratos Analytical Ltd.) equipped with a monochromatic Al Kα (1486.6 eV) x-ray source operating at 15 kV and 10 mA. The thickness of films was measured with a

spectral ellipsometer (model M44, J.A. Woollam Co. Inc.). For comparison purposes, some ALD YSZ on Si samples were left as-deposited for Pt deposition while the remaining were annealed after YSZ ALD at 800 ℃ in a preheated quartz horizontal furnace (Lindberg Blue three-zone furnace) in N_2 ambient for 5 min. The structure of annealed YSZ was determined with a glancing incidence x-ray diffractometer (X'pert, PANalytical B.N. Co.) and an incident angle of 1 º to enhance diffraction sensitivity within the film and to minimize interference from the underlying single crystal Si(100) substrate. The crystalline features were identified using the International Center for Diffraction Data database of diffraction pattern Powder Diffraction Files. Thus, two kinds of 45 nm-thick YSZ films (i.e., as-deposited and annealed) were employed as substrates for further ALD of Pt.

The ALD of Pt was done with trimethyl(methylcyclopentadienyl)platinum [$PtMe_3$(MeCp)] as Pt precursor and oxygen. The deposition was carried out at 300 ℃ while the Pt precursor reservoir was maintained at 40 ℃. In order to evaluate the effects of YSZ surface properties on ALD Pt, a series of Pt ALD cycles were performed on both as-deposited and annealed ALD YSZ films. A field emission scanning electron microscope (FE-SEM 4800, Hitachi Ltd.) was employed for the structural and morphological characterization of the resulting Pt structures. The resistivity of Pt was calculated from the thickness and sheet resistance measured by a linear 4-point probe modified for nanometer scale structures (Fig. 62) [166]. Prior to the measurement of resistivity, silver paint was applied between the probe and thin Pt structure in order to

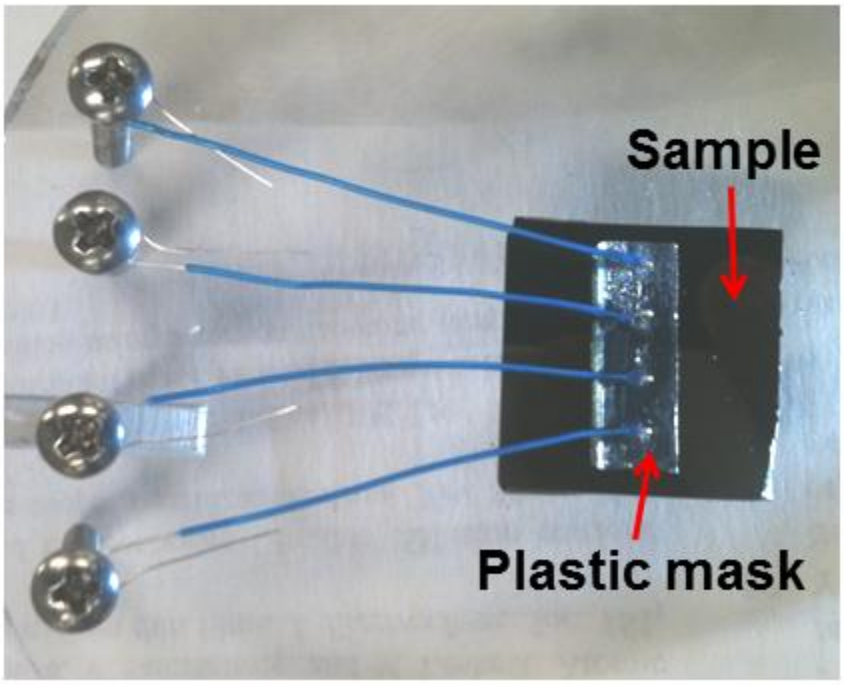

Figure 62. Photograph of four-point probe arrangement.

prevent the probe penetrating the thin Pt structure, and the silver paint was patterned with a plastic mask having four ~0.8 mm diameter holes equispaced 2.5 mm apart (Fig. 62).

4.6.3. Results and Discussion

Pt ALD cycle consists of sequential precursor pulse of 1.5 s (Fig. 63a), precursor Ar purge of 10 s, oxygen pulse of 1 s (Fig. 63b), and Ar purge of 10 s. The growth rate is found to saturate after 1.5 s pulse of MeCpPtMe3 (Fig. 63a). The temperature window of ALD Pt is found to be between 300-325 ℃ (Fig. 63c). The Pt growth rate is 0.056 nm/cycle (Fig. 64).

Figure 65 shows top-view SEM images of ALD Pt on as-deposited and post-deposition annealed ALD YSZ films. On the as-deposited YSZ film, 40 ALD cycles of Pt resulted in only Pt nanoparticles with size of 2-6 nm (Fig. 65a) with the low Pt nanoparticle density of ~3300/μm^2 and a small Pt coverage of 7%. These results indicate a low density of nucleation sites and a slow nucleation process for ALD Pt on as-deposited YSZ film. After 80 ALD cycles of Pt, larger Pt nanoparticles with size of 5-14 nm and a larger nanoparticle density of ~6100/μm^2 were obtained (Fig. 65b), yielding a Pt coverage of 22%. Even after 80 ALD cycles, a noncontinuous Pt nanoparticle morphology (Fig. 65b) was obtained, and these results corroborated the rather low Pt nucleation rate on as-deposited YSZ surface.

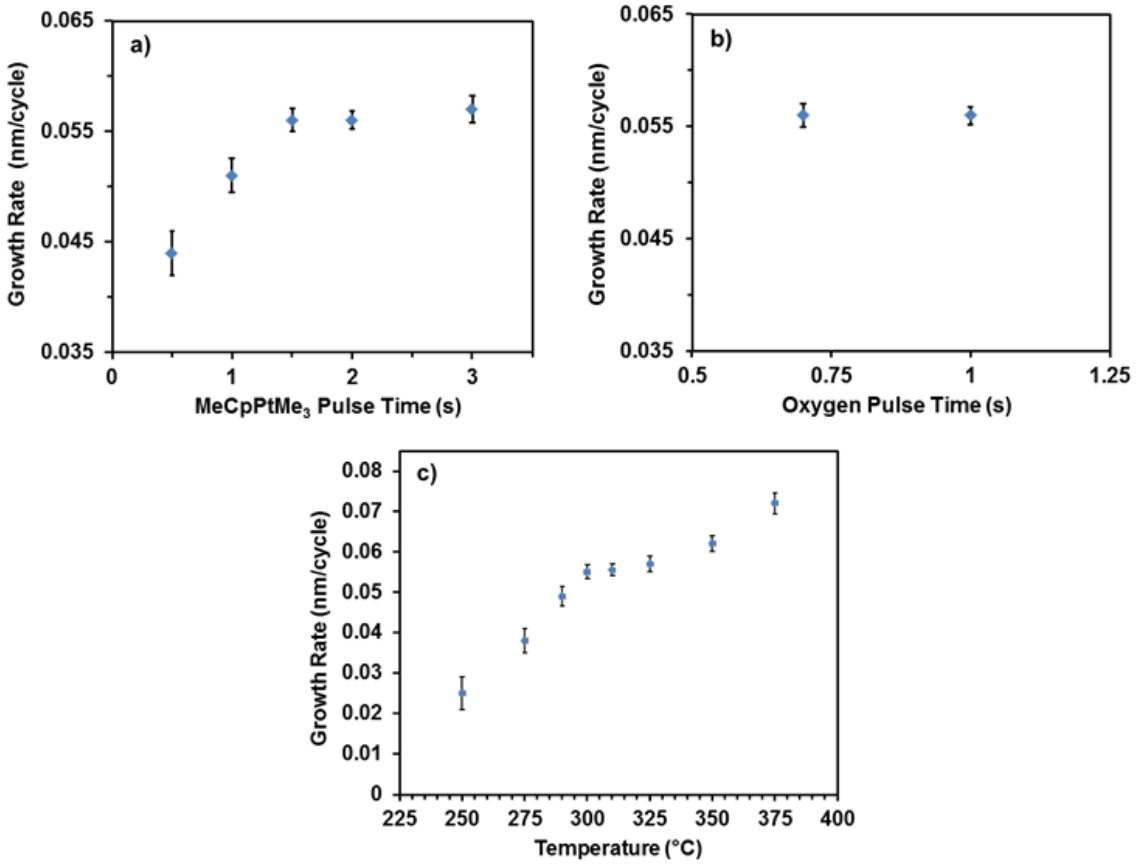

Figure 63. Pt precursor pulse (a) and oxygen pulse (b) dependence of ALD Pt growth rate at 300 ℃. Deposition temperature dependence of ALD Pt growth rate (c). The Pt precursor bubbler was maintained at 40 ℃ and the chamber pressure was kept at 0.5 torr. Precursor pulse of 1.5 s, precursor Ar purge of 10 s, oxygen pulse of 1 s, and Ar purge of 10 s were used.

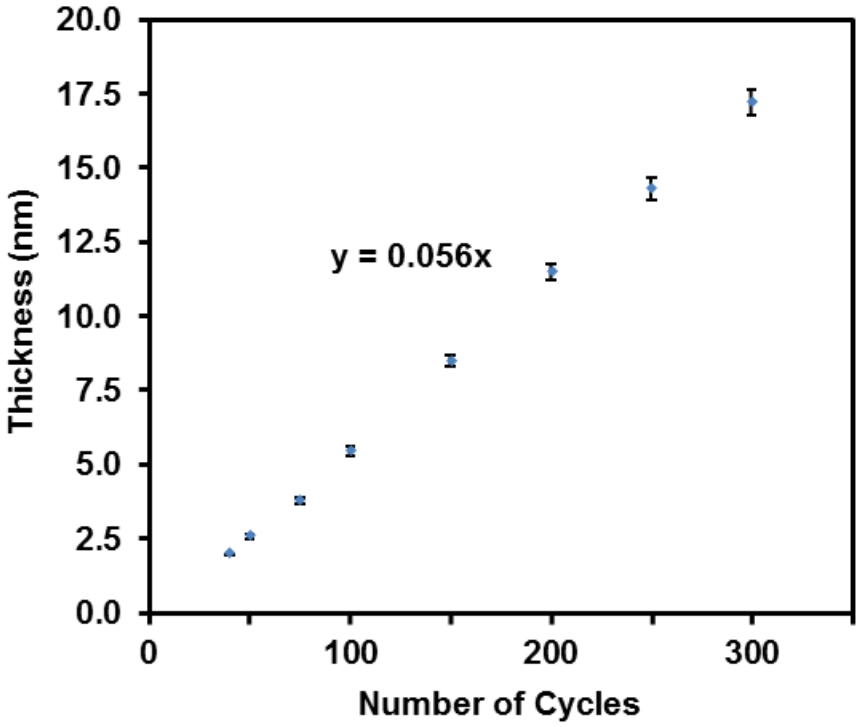

Figure 64. Thickness of ALD Pt as a function of the number of ALD cycles at 300 ℃. The other ALD conditions are the same as those in Fig.63.

The top-view SEM images of samples with 15, 40, 80, and 400 ALD cycles of Pt deposited on post-deposition annealed ALD YSZ films are shown in Figs. 65c, 65d, 65e, and 65f, respectively. In contrast to ALD Pt on as-deposited YSZ surface, post-deposition annealed YSZ samples yielded a faster nucleation rate of Pt ALD on them. As seen in Fig. 65c, 15 ALD cycles of Pt on annealed YSZ film yielded relatively small Pt nanoparticles, 2-4 nm in size, but a Pt nanoparticle density of ~13000/μm^2 (and a Pt coverage of 27%), which is fourfold and twice the nanoparticle densities of 40 and 80 cycles, respectively, for Pt deposited on as-deposited YSZ surface. The small size of nanoparticles may be attributed to the low number of ALD cycles (i.e., 15 cycles). On the other hand, the high Pt nanoparticle density (~13000/μm^2) with coverage of 27% suggests a large density of nucleation sites on the annealed YSZ surface which facilitates the adsorption of Pt precursor. After 40 ALD cycles, a Pt film thickness of ~2.5 nm thick on annealed YSZ film was measured with ellipsometry while Pt nanoparticles began coalescing (Fig. 65d), resulting in an improved Pt coverage of 65%. In contrast, Jiang et al. reported that 10 nm-thick ALD Pt start to coalesce on rf-sputtered YSZ film [65]. As shown in Fig. 65e, continuous mesoporous Pt film is obtained with pore size of 4-11 nm after 80 cycles of Pt deposited on annealed YSZ film with a significantly increased Pt coverage of 82%. Thus, in comparison to as-deposited YSZ surface, the annealed YSZ surface is found to provide a much larger number of nucleation sites for Pt ALD (Fig. 65c) yielding significantly higher Pt coverage with lesser Pt ALD cycles. The SEM image of 400 cycles of Pt on annealed YSZ film is shown in Fig. 65f, the surface is now found to be fully covered with Pt, and grain boundaries observed illustrate grain sizes of Pt to be between 13 and 25 nm.

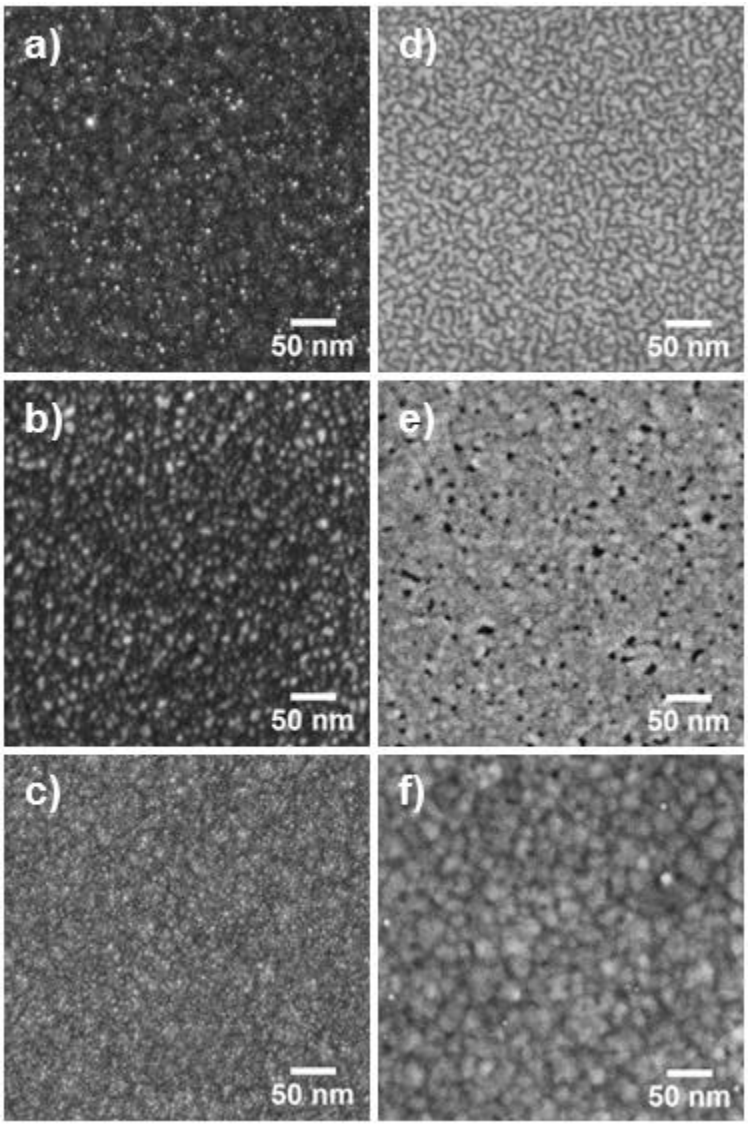

Figure 65. SEM images of Pt deposited with 40 (a) and 80 (b) Pt ALD cycles on as-deposited YSZ films. SEM images of Pt deposited with 15 (c), 40 (d), 80 (e), and 400 (f) cycles on post-deposition annealed YSZ films. The thickness of all ALD YSZ films deposited within the same reactor is 45 nm. The deposition was carried out at 270 ℃ under a pressure of 0.5 torr.

XANES analysis suggests the Pt film is metallic in bulk. These results suggest a means of controlling ALD Pt physical properties via thermal annealing of YSZ surface prior to ALD Pt. Such enhancement of nucleation rate may also offer more cost-effective use of Pt metal.

To explore the ALD YSZ surface properties affecting the ALD Pt nucleation, as-deposited and annealed YSZ films were investigated in terms of their surface hydrophilicity, roughness, and structure. At first, the surface hydrophilicity should be considered as an important factor in determining the nucleation behavior of Pt, because a hydrophilic surface generally offers more nucleation sites for ALD processes [165]. For example, as seen in Fig 66., the Pt ALD performed on Si shows that the hydrophilic OH-terminated Si having better Pt coverage, compared with that of hydrophobic H-terminated Si treated with 2% HF. This is in agreement with an earlier ALD study of Pt on Si [165]. For the YSZ surfaces, Fig. 67 (inset) shows the contact angles of DI water on YSZ films treated before and after post-deposition annealing, which are found to be ~75 º and ~5 º, respectively demonstrating the higher hydrophilicity of YSZ after annealing. The very low contact angle of annealed-YSZ film is likely attributed to an increased surface roughness induced by post-deposition annealing.

The hydrophilic surface of annealed YSZ is observed to yield a much higher density of Pt nanoparticles (~13000/μm^2) and a faster nucleation rate in term of Pt coverage (i.e., 82 % after 80 cycles of Pt) (Fig. 65). Thus, annealing ALD YSZ prior to Pt ALD can be an effective method to control density of YSZ nucleation sites for

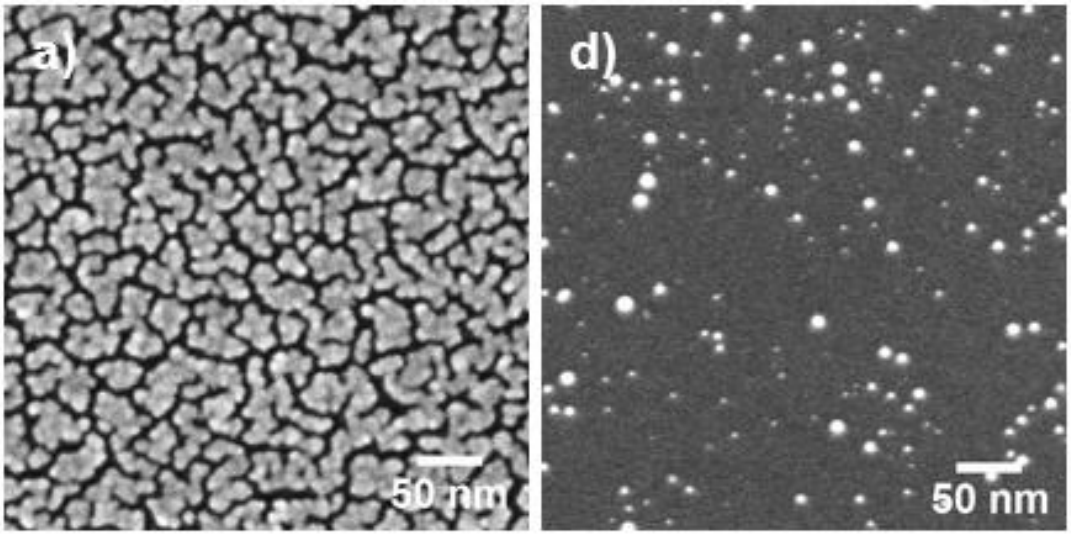

Figure 66. SEM images of Pt deposited with 80 Pt ALD cycles on OH- (a) and H- (b) terminated Si substrates. The H-terminated Si is formed by 2% hydrofluoric acid dip for 20 s.

$MeCpPtMe_3$ adsorption (e.g., Fig. 65c) and in turn control porous morphology of subsequently ALD Pt films.

The surface roughness of YSZ films is an important factor in determining the Pt nucleation, since the effective surface area of a film typically increases with surface roughness, which could increase the density of active sites on YSZ surface for Pt precursor adsorption. The root mean square (rms) roughness of as-deposited and annealed YSZ surfaces are found to be ~0.6 and ~1.5 nm, respectively. The increased rms roughness of YSZ film after post-deposition annealing is attributed to the phase transition of YSZ from mostly amorphous to polycrystalline cubic (Fig. 67 (main)). The surface roughness dependence on phase transition of YSZ films is found to be consistent with early studies of HfO_2, TiO_2, and Er_2O_3 [48, 66]. Besides the surface wettability and roughness, the polycrystalline cubic structures of YSZ films exhibit grain boundaries likely yielding more surface defects [167], which may facilitate the Pt nucleation process.

For ultra-thin Pt structures, the resistivity is influenced by the Pt morphology. In this study, the resistivity of Pt deposited on YSZ films is investigated by using four point probe measurement at room temperature with the modified system shown in Fig.62. The Pt nanoparticles shown in Fig. 65 (a, b and c) were not conductive due to their noncontinuous morphology. The resistivity of coalescent Pt nanoparticles (Fig. 65d), interconnected mesoporous Pt (Fig. 65e), and bulk Pt film (Fig. 65f) is shown in Fig. 68 with their morphologies labeled. The coalescent Pt nanoparticles exhibit a large resistivity of ~64 μΩ·cm and the interconnected mesoporous Pt shows a much lower

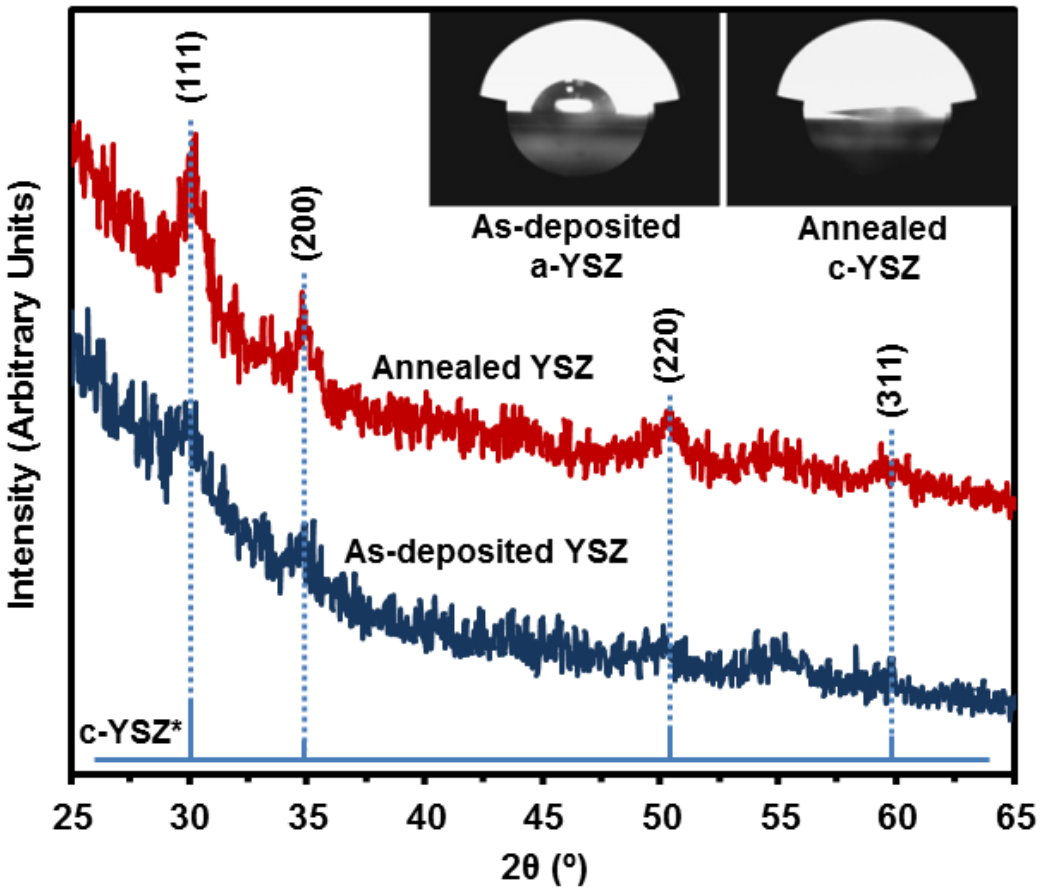

Figure 67. GIXRD patterns of as-deposited YSZ film and post-deposition annealed YSZ film (mian); wettability of as-deposited YSZ film and post-deposition annealed YSZ film (inset). The thickness of all YSZ films is 45 nm.

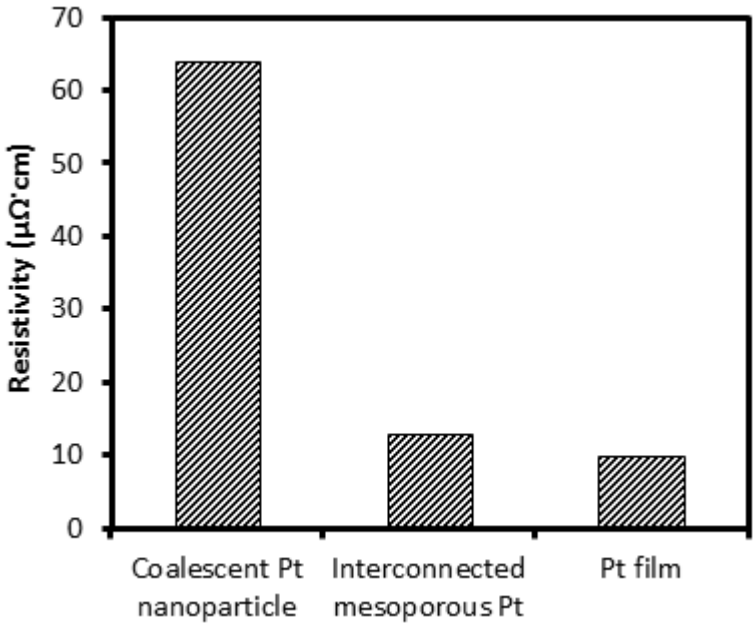

Figure 68. Resistivity of ALD Pt dependence of Pt morphology. The resistivity of coalescent Pt nanoparticles (after 40 cycles, Fig. 65d), interconnected mesoporous Pt (after 80 cycles, Fig. 65e), and bulk Pt film (after 400 cycles, Fig. 65f) are labeled in this figure. The measurement is carried out at room temperature using linear 4-point probe.

and bulk-like resistivity (~13 μΩ·cm), which is attributed to the interconnected morphology of Pt. Such a low resistivity is consistent with that of 50 nm thick ALD Pt on Al_2O_3 surface, reported in an earlier study, using $MeCpPtMe_3$/Air ALD process at the same temperature (300 ℃) [168]. Compared with the resistivity of chemical vapor deposited Pt (13-25 μΩ·cm) [169], the resistivity of the continuous ALD Pt film, in this study, is found to be ~11 μΩ·cm, which is practically the bulk Pt resistivity (10.8 μΩ·cm).

4.6.4. Summary

The nucleation behavior, morphology and other properties of ALD Pt on ALD YSZ films have been investigated with emphasis on the influence of surface properties of YSZ on Pt ALD, including factors of the resulting YSZ such as its hydrophilicity, roughness, and structure. Compared with the mostly amorphous as-deposited YSZ film, the post-deposition annealed YSZ film is found to be polycrystalline in cubic structure with hydrophilic and rough surface yielding a multifold higher Pt nucleation site density (e.g., ~13000/μm^2 after 15 ALD cycles), a faster Pt nucleation rate (coalescing after 40 cycles), and a larger surface coverage. These results demonstrate that annealing of ALD YSZ substrate can effectively modify the ALD Pt nucleation through varying the surface oxide properties of substrate, particularly when all processing is done within the same system. In this study, the interconnected mesoporous Pt films yielded near-bulk low resistivity (~13 μΩ·cm) with only 80 ALD cycles of Pt. Such mesoporous Pt films on YSZ offer new potential avenue in exploring nanoscale ITSOFCs in the future.

5. CONCLUSIONS

5.1. Atomic Layer Deposition of Amorphous $Er_xTi_{1-x}O_y$ Dielectric Thin Films

$Er_xTi_{1-x}O_y$ dielectric thin films were deposited on Si(100) substrates by ALD using $(CpMe)_3Er$ and TDEAT as metal precursors, and O_3 as oxidant. Compositional tunability of $Er_xTi_{1-x}O_y$ films was obtained through deposition process control. $Er_xTi_{1-x}O_y$ films with ALD cycle ratios (Er_2O_3/TiO_2) of 1:8 or higher are found to have good thermal stability and remain amorphous with unchanged surface roughness after post-deposition RTP at 700 ℃ in O_2. The good thermal stability is attributed to the incorporation of ions with radii much larger than Ti, and these impurity atoms could significantly distort the original TiO_2 structure and enhance the entropy for the crystallization process. Electrical measurements showed that optimized amorphous $Er_xTi_{1-x}O_y$ films, without grain boundaries, after RTP exhibited a dielectric constant of ~36, a hysteresis voltage of less than 10 mV, and a low leakage current density of 10^{-8} A/cm^2 at −1 MV/cm. The sizable reduction of leakage current density of $Er_xTi_{1-x}O_y$ found in our study suggests that amorphous $Er_xTi_{1-x}O_y$ thin films are promising future dielectrics in Si integrated circuit technology.

5.2. Chemical Passivation of III-V Semiconductor Surfaces by ALD ZnS

The ALD of amorphous and pinhole free ZnS passivation nanofilms was developed and studied in the long-term chemical passivation of III-V semiconductor-based surfaces. TAM-treated III-V semiconductor surfaces passivated without or with 1 and 2 nm-thick ZnS capping layer were investigated to evaluate changes at the surface/interface of passivated GaSb surfaces over time. The 2 nm-thicker ZnS film was

found to provide good protection against oxidation by air as evidenced by the reduction of the corresponding oxide formation; these results indicated that oxygen diffusion through the ZnS is an important step in the long-term chemical passivation of III-V semiconductor-based nanostructures. In addition, the ALD amorphous thin insulator films without pinhole are suggested to be efficient in the passivation of III-V semiconductor-based structures.

5.3. Growth Characteristics and Properties of ALD Yttrium Oxide Thin Films

A novel ALD route of Y_2O_3 thin films was developed and demonstrated utilizing $Y(iPrCp)_3$ and O_3. The ALD growth characteristics were investigated by varying precursor dosage, reactor temperature, and number of deposition cycles. The growth rate of Y_2O_3 was found to be 0.17 ± 0.01 nm/cycle within the ALD temperature window of 245 – 300 ℃. The composition of ALD Y_2O_3 was extensively investigated with XPS coupled with Ar^+ beam sputtering. The resulting bulk films were found to be stoichiometric Y_2O_3 with $Y(OH)_3$ formed on the surface because of the absorbance of moisture. The results of this work demonstrate the potential for suggesting $Y(iPrCp)_3$ as a suitable ALD precursor and Ar^+ beam as an effective means of removing surface $Y(OH)_3$ on Y_2O_3 films.

5.4. Atomic Layer Deposition of Yttria-doped Zirconia Thin Films

YSZ thin films were deposited using $Y(iPrCp)_3$ and $CpZr(NMe_2)_3$ as metal precursors with O_3 as oxidant on Si. A sufficient overlapping temperature window of $Y(iPrCp)_3/O_3$ and $CpZr(NMe_2)_3/O_3$ processes was obtained between 240 and 300 ℃,

which enables the co-ALD of Y_2O_3 and ZrO_2. The atomic ratio of Y/(Y+Zr) in YSZ films was found to increase monotonically with increasing normalized ALD cycle ratio of $Y_2O_3/(Y_2O_3+ZrO_2)$, indicating excellent composition tunability of YSZ film. 8 mol% Y_2O_3 stabilized ZrO_2 was obtained with ALDCR of 1:5. XPS analyses suggest that YSZ films deposited with ALDCR of 1:5 was found to effectively prevent the formation of $Y(OH)_3$ during exposure in atmospheric air. The as-deposited ZrO_2 and YSZ films with variable ALDCR were found to be mostly amorphous, indicating the onset of film crystallization under the ALD conditions used. After post-deposition annealing in N_2 at 800 ℃ for 5 min, ZrO_2 and YSZ films were observed to crystallize in cubic structure with (1 1 1) orientation dominance. The average lattice constant and grain size of post-deposition annealed YSZ films were found to be 0.5140 and 8.2 nm, respectively.

5.5. Nucleation Behavior-Morphology-Resistivity of Atomic Layer Deposited Pt on Atomic Layer Deposited Yttria-Stabilized Zirconia Films

The nucleation behavior, morphology and other properties of ALD Pt on ALD YSZ films have been investigated with emphasis on the influence of surface properties of YSZ on Pt ALD, including factors of the resulting YSZ such as its hydrophilicity, roughness, and structure. Compared with the mostly amorphous as-deposited YSZ film, the post-deposition annealed YSZ film is found to be polycrystalline in cubic structure with hydrophilic and rough surface yielding a multifold higher Pt nucleation site density (e.g., ~13000/μm^2 after 15 ALD cycles), a faster Pt nucleation rate (coalescing after 40 cycles), and a larger surface coverage. These results demonstrate that annealing of ALD YSZ substrate can effectively modify the ALD Pt nucleation through varying the surface

oxide properties of substrate, particularly when all processing is done within the same system. In this study, the interconnected mesoporous Pt films yielded near-bulk low resistivity (~13 μΩ·cm) with only 80 ALD cycles of Pt. Such mesoporous Pt films on YSZ offer new potential avenue in exploring nanoscale ITSOFCs in the future.

6. FUTURE WORK

6.1. Atomic Layer Deposition of High-κ Dielectric on Passivated III-V Semiconductor

In my PhD studies, high-κ dielectrics have been atomic layer deposited for Si integrated circuit technology, and the resulting Si-based MOS structures show high dielectric constant and low leakage current. Compared with the traditional Si-based device, III-V semiconductors would be more promising because of their very high mobility, which could enhanced the performance of future advanced semiconductor devices, especially high-speed electronics. However, the native oxide of III-V semiconductors can be easily formed during the fabrication of upper layer oxide dielectrics. The native oxide at the interface between III-V semiconductor substrate and dielectric film often induces non-negligible leakage current and, as a result, limits the device performance. Thus, a major challenge for improving the performance of III-V semiconductor-based devices is fabrication of high-κ metal oxide on passivated III-V semiconductors without forming native oxide on semiconductor surface. The future work would be focused on ALD of high-κ metal oxides on III-V group semiconductors passivated with aqueous solution and/or ALD thin film.

6.2. Annealing Behavior and Electrical Properties of Atomic Layer Deposited Pt

In my previous work, the thin structure of Pt/yttria-stabilized zirconia has been successfully atomic layer deposited. The nucleation behavior and morphology of ALD Pt on YSZ have been investigated, and the morphology of Pt is found to depend on ALD cycles number of Pt and the surface properties of YSZ. Since the resistivity of Pt is

important for electrode application, the Pt resistivity dependence of morphology should be studied to evaluate the compromise between mesoporous morphology and resistivity of resulting ALD Pt. In addition, the morphology of Pt could be a function of annealing temperature, and the resistivity of ultra-thin Pt could dependent on the annealing environment, such as hydrogen and nitrogen environment. Understanding the annealing behavior-morphology-resistivity of Pt would be important in the design and fabrication of ITSOFCs.

CITED LITERATURE

1. J. E. Lilienfeld, U.S. Patent, 1745175 (1926).
2. C.-T. Sah, Proc. of the IEEE, 76, 1280 (1988).
3. J. Bardeen and W. H. Brattain, U.S. Patent, 2524035 (1948).
4. J. Bardeen and W. H. Brattain, Phys. Rev., 74, 230 (1948).
5. G. C. Dacey and I. M. Ross, Proc. IRE, 41, 970 (1953).
6. J. S. Kilby, IEEE Trans. Electron Dev., 23, 648 (1976).
7. G. E. Moore, Electronics, 38, 114 (1965).
8. S. Borkar and A. A. Chien, Comm. of the ACM, 54, 67 (2011).
9. R. H. Dennard, F. H. Gaensslen, V. L. Rideout, E. Bassous, and A. R. LeBlanc, J. Solid-State Circuits, 9, 256 (1974).
10. P. Barry and P. Crowley, Modern Embedded Computing: Designing Connected, Pervasive, Media-Rich Systems, Morgan Kaufmann (2012).
11. G. D. Wilk, R. M. Wallace, and J. M. Anthony, J. Appl. Phys., 89, 5243 (2001).
12. S. Guha and V. Narayanan, Annu. Rev. Mater. Res., 39, 181 (2009).
13. J. Robertson, Eur. Phys. J. Appl. Phys., 28, 265 (2004).
14. M. Bohr, R. Chau, T. Ghani, and K. Mistry, IEEE Spectrum, 44, 29 (2007).
15. B. M. Borg, K. A. Dick, B. Ganjipour, M.-E. Pistol, L.-E. Wernersson, and C. Thelander, Nano Lett., 10, 4080 (2010).
16. I. Jahangir, S. Jahangir, and Q. D. Khosru, ECS Trans., 35, 121 (2011).
17. V. M. Andreev, S. V. Sorokina, N. K. Timoshina, V. P. Khvostikov, and M. Z. Shvarts, Semiconductors, 43, 668 (2009).

18. S. Luca, J. L. Santailler, J. Rothman, J. P. Belle, C. Calvat, G. Basset, A. Passero, V. P. Khvostikov, N. S. Potapovich, and R. V. Levin, J. Solar Energy Eng., 129, 304 (2007).

19. R. B. Laghumavarapu, A. Moscho, A. Khoshakhlagh, M. El-Emawy, L. F. Lester, and D. L. Huffaker, Appl. Phys. Lett., 90, 173125 (2007).

20. P. V. V. Jayaweera, S. G. Matsik, A. G. U. Perera, Y. Paltiel, A. Sher, A. Raizman, H. Luo, and H. C. Liu, Appl. Phys. Lett., 90, 111109 (2007).

21. F. M. Mohammedy and M. J. Deen, J. Mater. Sci.: Mater. Electron., 20, 1039 (2009).

22. V. N. Bessolov and M. V. Lebedev, Semiconductors, 32, 1141 (1998).

23. G. P. Schwartz, G. J. Gualtieri, J. E. Griffiths, C. D. Thurmond, and B. Schwartz, J. Electrochem. Soc., 127, 2488 (1980).

24. Z. Y. Liu, T. F. Kuech, and D. A. Saulys, Appl. Phys. Lett., 83, 2587 (2003).

25. K. Banerjee, S. Ghosh, S. Mallick, E. Plis, and S. S. Krishna, J. Electron. Mater., 38, 1944 (2009).

26. K. Banerjee, S. Ghosh, E. Plis, and S. Krishna, J. Electron. Mater., 39, 2210 (2010).

27. R. Stine, E. H. Aifer, L. J. Whitman, and D. Y. Petrovykh, Appl. Surf. Sci., 255, 7121 (2009).

28. M. Liehr and H. Lueth, J. Vac. Sci. Technol., 16, 1200 (1979).

29. S. Weiguo, Appl. Phys. A, 52, 75 (1991).

30. A. B. Stambouli and E. Traversa, Renew. Sust. Energ. Rev., 6, 433 (2002).

31. M. Cassir, A. Ringuede, and L. Niinisto, J. Mater. Chem., 20, 8987 (2010).

32. J. H. Shim, C.-C. Chao, H. Huang, and F. B. Prinz, Chem. Mater., 19, 3850 (2007).

33. L. B. Freund and S. Suresh, Thin Film Materials: Stress, Defect Formation and Surface Evolution, Cambridge University Press (2004).

34. P. M. Martin, Handbook of Deposition Technologies for Films and Coatings: Science, Applications and Technology, William Andrew (2009).

35. H. O. Pierson, Handbook of Chemical Vapor Deposition: Principles, Technology and Applications, William Andrew (1999).

36. J. A. Thornton, Ann. Rev. Mater. Sci., 7, 239 (1977).

37. A. C. Jones and M. L. Hitchman, Chemical Vapour Deposition: Precursors, Processes and Applications, Royal Society of Chemistry (2008).

38. S. M. George, Chem. Rev., 110, 111 (2010).

39. C. O. Chui, IEEE Electron Dev. Lett. , 25, 274 (2004).

40. R. K. Nahar, V. Singh, and A. Sharma, J. Mater. Sci. Mater. Electron., 18, 615 (2007).

41. J. Niinisto, K. Kukli, M. Heikkila, M. Ritala, and M. Leskela, Adv. Eng. Mater., 11, 223 (2009).

42. K. Kim and S. Y. Lee, Microelectron. Eng., 84, 1976 (2007).

43. L. Niinisto, M. Nieminen, J. Paivasaari, J. Niinisto, M. Putkonen, and M. Nieminen, Phys. Stat. Sol. (a), 201, 1443 (2004).

44. B. H. Lee, IEEE Trans. Electron Dev., 55, 8 (2008).

45. W. Lehnert, G. Ruhl, and A. Gschwandtner, J. Vac. Sci. Technol. A, 30, 01A152 (2012).

46. H. Kwon, H.-H. Park, B.-H. Kim, and J. S. Ha, J. Electrochem. Soc., 156, G13 (2009).

47. M. Lukosius, C. B. Kaynak, S. Rushworth, and C.Wenger, J. Electrochem. Soc., 158, G119 (2011).

48. Q. Tao, A. Kueltzo, M. Singh, G. Jursich, and C. G. Takoudis, J. Electrochem. Soc., 158, G27 (2011).

49. S. Jeon and H. Hwang, Appl. Phys. Lett., 81, 4856 (2002).

50. T.-M. Pan, C.-L. Chen, W. W. Yeh, and S.-J. Hou, Appl. Phys. Lett., 89, 222912 (2006).

51. J. Paivasaari, J. Niinisto, K. Arstila, K. Kukli, M. Putkonen, and L. Niinisto, Chem. Vap. Deposition, 11, 415 (2005).

52. E. V. Kunitsyna, T. V. Lvova, M. S. Dunaevskii, Y. V. Terentev, A. N. Semenov, V. A. Solovev, B. Y. Meltser, S. V. Ivanov, and Y. P. Yakovlev, Appl. Surf. Sci., 256, 5644 (2010).

53. J. V. Li, S. L. Chuang, E. Aifer, and E. M. Jackson, Appl. Phys. Lett., 90, 223503 (2007).

54. A. Salesse, A. Joullie, P. Calas, J. Nieto, F. Chevrier, Y. Cuminal, G. Ferblantier, and P. Christol, Phys. Stat. Sol. (c), 4, 1508 (2007).

55. A. Gin, Y. Wei, J. Bae, A. Hood, J. Nah, and M. Razeghi, Thin Solid Films, 447, 489 (2003).

56. I. M. Hung, H. P. Wang, W. H. Lai, K. Z. Fung, and M. H. Hon, Electrochimica Acta, 50, 745 (2004).

57. M. Leskela and M. Ritala, Angew. Chem. Int. Ed., 42, 5548 (2003).

58. T. P. Holme, C. Lee, and F. B. Prinz, Solid State Ionics, 179, 1540 (2008).

59. J. W. Elam, N. P. Dasgupta, and F. B. Prinz, Mat. Res. Soc. Bull., 36, 899 (2011).

60. B. Medina-Lott, M. Tasse, C. Brahim, A. Ringuede, L. Niinisto, and M. Cassir, ECS Trans., 35, 601 (2011).

61. C. Bernay, A. Ringuede, P. Colomban, D. Lincot, and M. Cassir, J. Phys. Chem. Sol., 64, 1761 (2003).

62. M. Putkonen, T. Sajavaara, J. Niinisto, L.-S. Johanssonc, and L. Niinisto, J. Mater. Chem., 12, 442 (2002).

63. P.-C. Su, C.-C. Chao, J. H. Shim, R. Fasching, and F. B. Prinz, Nano Lett., 8, 2289 (2008).

64. M. Tsuchiya, B.-K. Lai, and S. Ramanathan, Nature Nanotech., 6, 282 (2011).

65. X. Jiang, H. Huang, F. B. Prinz, and S. F. Bent, Chem. Mater., 20, 3897 (2008).

66. R. Xu, Q. Tao, Y. Yang, and C. G. Takoudis, Appl. Surf. Sci., 258, 8514 (2012).

67. M. J. Hart and A. G. R. Evans, Semicond. Sci. Technol., 3, 421 (1988).

68. RTP-600S Operation and Installation Manual, Modular Process Technology Corp. (2003).

69. http://www.modularpro.com/T600SFM.html.

70. Laboratory Furnaces, Thermo Electron Corp., http://www.thermo.com.cn/Resources/200802/productPDF_31131.pdf.

71. Guide to Using WVASE32, J. A. Woollam Co., Inc. (1996).

72. M-44 Spectroscopic Ellipsometer Hardware Manual, J. A. Woollam Co., Inc. (1999).

73. http://www.jawoollam.com.

74. K. Vdeam, Thin Solid Films, 313-314, 1 (1998).

75. T. A. Carlson, Annu. Rev. Phys. Chem., 26, 211 (1975).

76. C. S. Fadley, J. Electron. Spectrosc. Relat. Phenom., 178-179, 2 (2010).

77. N. H. Turner, Anal. Chem., 58, 153R (1986).

78. Q. Tao, G. M. Jursich, and C. Takoudis, IEEE Trans. Semicond. Manuf., 24, 139 (2011).

79. C. E. Pfluger, Anal. Chem., 42, 317R (1970).

80. D. R. Davies, Annu. Rev. Biochem., 36, 321 (1967).

81. R. Feidenhans'l, Surf. Sci. Rep., 10, 105 (1989).

82. B. Clemens and J. Bain, Mat. Res. Soc. Bull., 17, 46 (1992).

83. J. W. Jeffery, Methods in X-Ray Crystallography, Academic Press (1971).

84. A. Deshpande, R. Inman, G. Jursich, and C. G. Takoudis, J. Appl. Phys., 99, 094102/1 (2006).

85. F. Lijten, J. Klaessens, and G. Kateman, TrAC, Trends Anal. Chem., 5, X (1986).

86. Y. He and Y. Inoue, Polym. Int., 49, 623 (2000).

87. P. Singh, H. C. Andola, M. S. M. Rawat, G. J. N. Pant, and V. K. Purohit, Res. J. Med. Plant, 5, 127 (2011).

88. N. Mandal, S. Chakraborty, R. Ameta, S. Bandyopadhyay, S. Dasgupta, R. Mukhopadhyay, A. S. Deuri, and J. K. Tyre, Rubber World, 235, 36 (2006).

89. K. A. Bakeev, Process Analytical Technology: Spectroscopic Tools and Implementation Strategies for the Chemical and Pharmaceutical Industries, Wiley-Blackwell (2005).

90. W. Reuter and J. E. E. Baglin, J. Vac. Sci. Technol., 18, 282 (1981).

91. T. L. Alford, L. C. Feldman, and J. W. Mayer, Fundamentals of Nanoscale Film Analysis, Springer (2007).

92. B. Heidemann, T. Tappe, B. Schmiedeskamp, and U. Heinzmann, Thin Solid Films, 228, 60 (1993).

93. P. J. Caber, Appl. Opt., 32, 3438 (1993).

94. Y.-Y. Cheng and J. C. Wyant, Appl. Opt., 24, 804 (1985).

95. WYKO Surface Profilers Technical Reference Manual, Veeco Metrology Group (1999).

96. Y.-Y. Cheng and J. C. Wyant, Appl. Opt., 24, 3049 (1985).

97. K. B. Jinesh, Y. Lamy, E. Tios, and W. F. A. Besling, Appl. Phys. Lett., 94, 252906 (2009).

98. J. M. J. Lopes, M. Roeckerath, T. Heeg, U. Littmark, J. Schubert, S. Mantl, Y. Jia, and D. G. Schlom, Microelectron. Eng., 84, 1890 (2007).

99. H. Ono and T. Katsumata, Appl. Phys. Lett., 78, 1832 (2001).

100. K. Kakushima, K. Tsutsui, S.-I. Ohmi, P. Ahmet, V. R. Rao, and H. Iwai, Top. Appl. Phys., 106, 345 (2007).

101. J. Paivasaari, J. Niinisto, P. Myllymaki, C. Dezelah, C. H. Winter, M. Putkonen, M. Nieminen, and L. Niinisto, Top. Appl. Phys., 106, 15 (2007).

102. J. Paivasaari, C. L. Dezelah, D. Back, H. M. El-Kadri, M. J. Heeg, M. Putkonen, L. Niinisto, and C. H. Winter, J. Mater. Chem., 15, 4224 (2005).

103. J. Paivasaari, M. Putkonen, and L. Niinisto, Thin Solid Films, 472, 275 (2005).

104. M. Losurdo, M. M. Giangregorio, G. Bruno, D. Yang, E. A. Irene, A. A. Suvorova, and M. Saunders, Appl. Phys. Lett., 91, 091914 (2007).

105. C. Adelhelm, T. Pickert, M. Balden, M. Rasinski, T. Plocinski, C. Ziebert, F. Koch, and H. Maier, Scripta Mater., 61, 789 (2009).

106. M. P. Singh, T. Shripathi, K. Shalini, and S. A. Shivashankar, Mater. Chem. Phys., 105, 433 (2007).

107. G. Scarel, A. Svane, and M. Fanciulli, Top. Appl. Phys., 106, 1 (2007).

108. G. C. Deepak and N. Bhat, ECS Trans., 19, 175 (2009).

109. V. Mikhelashvili, G. Eisenstein, and F. Edelmann, J. Appl. Phys., 90, 5447 (2001).

110. M. P. Singh, C. S. Thakur, K. Shalini, N. Bhat, and S. A. Shivashankar, Appl. Phys. Lett., 83, 2889 (2003).

111. M. Losurdo, M. M. Giangregorio, P. Capezzuto, G. Bruno, G. Malandrino, I. L. Fragala, L. Armelao, D. Barreca, and E. Tondello, J. Electrochem. Soc., 155, G44 (2008).

112. J. Paivasaari, M. Putkonen, T. Sajavaara, and L. Niinisto, J. Alloys Compd., 374, 124 (2004).

113. J. Niinisto, M. Putkonen, L. Niinisto, K. Kukli, M. Ritala, and M. Leskela, J. Appl. Phys., 95, 84 (2004).

114. J. Niinisto, M. Putkonen, L. Niinisto, K. Arstila, T. Sajavaara, J. Lu, K. Kukli, M. Ritala, and M. Leskela, J. Electrochem. Soc., 153, F39 (2006).

115. P. Majumder, G. Jursich, A. Kueltzo, and C. Takoudis, J. Electrochem. Soc., 155, G152 (2008).

116. M. Nolan and S. D. Elliott, Chem. Mater., 22, 117 (2010).

117. T. V. Trinh and J. P. Chang, Appl. Surf. Sci., 246, 250 (2005).

118. R. A. Nyquist and R. O. Kagel, Handbook of Infrared and Raman Spectra of Inorganic Compounds and Organic Salts. Infrared Spectra of Inorganic Compounds, 4, Academic Press (1997).

119. NIST X-ray Photoelectron Spectroscpoy Database Version 3.2 (2007).

120. L. Armelao, D. Bareca, G. Bottaro, A. Gasparotto, D. Leonarduzzi, C. Maragno, and E. Tondello, Surf. Sci. Spectra, 11, 26 (2004).

121. M. F. Al-Kuhaili and S. M. A. Durrani, Thin Solid Films, 515, 2885 (2007).

122. S. Scalese, S. Mirabella, and A. Terrasi, Appl. Surf. Sci., 220, 231 (2003).

123. S. K. Kim, S. W. Lee, C. S. Hwang, Y.-S. Min, J. Y. Won, and J. Jeong, J. Electrochem. Soc., 153, F69 (2006).

124. X. Song and C. G. Takoudis, J. Electrochem. Soc., 154, G177 (2007).

125. A. V. Shlyakhtina, D. A. Belov, O. K. Karyagina, and L. G. Shcherbakova, J. Alloys Compd., 479, 6 (2009).

126. R. B. v. Dover, Appl. Phys. Lett., 74, 3041 (1999).

127. M. Ritala, M. Leskela, E. Nykanen, P. Soininen, and L. Niinisto, Thin Solid Films, 228, 32 (1993).

128. J. Aarik, A. Aidla, T. Uustare, M. Ritala, and M. Leskela, Appl. Surf. Sci., 161, 385 (2000).

129. P. Majumder, G. Jursich, and C. Takoudis, J. Appl. Phys., 105, 104106 (2009).

130. B. Miao, R. Mahapatra, N. Wright, and A. Horsfall, J. Appl. Phys., 104, 054510 (2008).

131. W. D. Kim, G. W. Hwang, O. S. Kwon, S. K. Kim, M. Cho, D. S. Jeong, S. W. Lee, M. H. Seo, C. S. Hwang, Y.-S. Min, and Y. J. Cho, J. Electrochem. Soc., 152, C552 (2005).

132. F. M. Li, B. C. Bayer, S. Hofmann, J. D. Dutson, S. J. Wakeham, M. J. Thwaites, W. I. Milne, and A. J. Flewitt, Appl. Phys. Lett., 98, 252903 (2011).

133. Q. Tao, G. Jursich, P. Majumder, M. Singh, W. Walkosz, P. Gu, R. Klie, and C. Takoudis, Electrochem. Soid-State Lett., 12, G50 (2009).

134. S. A. Campbell, H.-S. Kim, D. C. Gilmer, B. He, T. Ma, and W. L. Gladfelter, IBM J. Res. Develop., 43, 383 (1999).

135. E. P. Gusev, C. Cabral, M. Copel, C. D'Emic, and M. Gribelyuk, Microelectron. Eng., 69, 145 (2003).

136. M. M. Frank, Y. J. Chabal, M. L. Green, A. Delabie, B. Brijs, G. D. Wilk, M.-Y. Ho, E. B. O. d. Rosa, I. J. R. Baumvol, and F. C. Stedile, Appl. Phys. Lett., 83, 740 (2003).

137. Q. Tao, G. Jursich, and C. Takoudis, Appl. Phys. Lett., 96, 192105 (2010).

138. J. R. Bakke, J. S. King, H. J. Jung, R. Sinclair, and S. F. Bent, Thin Solid Films, 518, 5400 (2010).

139. G. Stuyven, P. D. Visschere, A. Hikavyy, and K. Neyts, J. Cryst. Growth, 234, 690 (2002).

140. J. T. Tanskanen, J. R. Bakke, T. A. Pakkanen, and S. F. Bent, J. Vac. Sci. Technol. A, 29, 031507 (2011).

141. G. Z. Wang, B. Y. Geng, X. M. Huang, Y. W. Wang, G. H. Li, and L. D. Zhang, Appl. Phys. A, 77, 933 (2003).

142. J. Yang, J. Peng, R. Zou, F. Peng, H. Wang, H. Yu, and J. Lee, Nanotechnology, 19, 255603 (2008).

143. S. Jeon, S. Bang, S. Lee, S. Kwon, W. Jeong, H. Jeon, H. J. Chang, and H.-H. Park, J. Korean Phys. Soc., 53, 3287 (2008).

144. S. McDonnell, D. M. Zhernokletov, A. P. Kirk, J. Kim, and R. M. Wallace, Appl. Surf. Sci., 257, 8747 (2011).

145. D. Y. Petrovykh, M. J. Yang, and L. J. Whitman, Surf. Sci., 523, 231 (2003).

146. P. d. Rouffignac, J.-S. Park, and R. G. Gordon, Chem. Mater., 17, 4808 (2005).

147. Y.-H. Wu, C.-C. Lin, Y.-C. Hu, M.-L. Wu, J.-R. Wu, and L.-L. Chen, IEEE Electron Device Lett., 32, 1107 (2011).

148. G. Apostolopoulos, G. Vellianitis, A. Dimoulas, M. Alexe, R. Scholz, M. Fanciulli, D. T. Dekadjevi, and C. Wiemer, Appl. Phys. Lett., 81, 3549 (2002).

149. W. J. Varhue, M. Massimo, J. M. Carrulli, V. Baranauskas, E. Adams, and E. Broitman, J. Vac. Sci. Technol. A, 11, 1870 (1993).

150. M. Putkonen, T. Sajavaara, L.-S. Johansson, and L. Nunisto, Chem. Vap. Deposition, 7, 44 (2001).

151. E. P. Gusev, E. Cartier, M. Copel, M. Gribelyuk, D. A. Buchanan, H. Okorn-Schmidt, C. D. Emic, P. Kozlowski, M. Tuominen, and M. Linnermo, Proc. Electrochem. Soc., 9, 189 (2001).

152. J. Niinisto, M. Putkonen, and L. Niinisto, Chem. Mater., 16, 2953 (2004).

153. Y. Kuroda, H. Hamano, T. Mori, Y. Yoshikawa, and M. Nagao, Langmuir, 16, 6937 (2000).

154. C. K. Lee and H.-H. Park, J. Korean. Phys. Soc., 46, 254 (2005).

155. X. J. Wang, L. D. Zhang, J. P. Zhang, G. He, M. Liu, and L. Q. Zhu, Mater. Lett., 62, 4235 (2008).

156. J. P. P. Huijsmans, F. P. F. v. Berkel, and G. M. Christie, J. Power Sources, 71, 107 (1998).

157. J. Zhu and Z. G. Liu, Mater. Lett., 57, 4297 (2003).

158. J. Niinisto, K. Kukli, M. Kariniemi, M. Ritala, M. Leskela, N. Blasco, A. Pinchart, C. Lachaud, N. Laaroussi, Z. Wang, and C. Dussarrat, J. Mater. Chem., 18, 5243 (2008).

159. Q. Tao, G. Jursich, P. Majumber, M. Singh, W. Walkosz, P. Gu, R. Kelie, and C. G. Takoudis, Electrochem. Soid-State Lett., 12, G50 (2009).

160. R. Xu and C. G. Takoudis, J. Solid State Sci. Technol., 1, N107 (2012).

161. W.-H. Nam and S.-W. Rhee, Chem. Vap. Deposition, 10, 201 (2004).

162. C. Henkel, S. Abermann, O. Bethge, and E. Bertagnolli, Semicond. Sci. Technol., 24, 125013/1 (2009).

163. S. T. Christensen, J. W. Elam, F. A. Rabuffetti, Q. Ma, S. J. Weigand, B. Lee, S. Seifert, P. C. Stair, K. R. Poeppelmeier, M. C. Hersam, and M. J. Bedzyk, Small, 5, 750 (2009).

164. H.-B.-R. Lee and S. F. Bent, Chem. Mater., 24, 279 (2012).

165. G. Liang, H. Cheng, Z. Zhiwei, Z. Wei, W. Dongping, and Z. Shili, J. Semicond., 33, 083003 (2012).

166. F. M. Smits, Bell Syst. Tech. J. , 37, 711 (1958).

167. V. P. Pakharukova, E. M. Moroz, D. A. Zyuzin, V. I. Zaikovskii, F. V. Tuzikov, G. R. Kosmambetova, and P. E. Strizhak, J. Phys. Chem. C, 116, 9762 (2012).

168. T. Aaltonen, M. Ritala, Y.-L. Tung, Y. Chi, K. Arstila, K. Meinander, and M. Leskela, J. Mater. Res., 19, 3353 (2004).

169. J. M. Lee, C. S. Hwang, H.-J. Cho, C.-G. Suk, and H. J. Kim, J. Electrochem. Soc., 145, 1066 (1998).

VITA

Runshen Xu

EDUCATION

Ph.D., Chemical Engineering, University of Illinois, Chicago, Illinois, USA, 2012
B. Tech., Chemical Engineering, Dalian University of Technology, Dalian, China, 2008

PUBLICATIONS

1. R. Xu, S. Selvaraj, N. Azimi, and C. Takoudis, "Growth Characteristics and Properties of Yttrium Oxide Thin Films by ALD from Novel $Y(iPrCp)_3$ Precursor and O_3", ECS Transactions, (accepted / in press)
2. R. Xu and C. Takoudis, "Atomic Layer Deposition and Characterization of Amorphous $Er_xTi_{1-x}O_y$ Dielectric Thin Films", J. Solid State Sci. Technol., 1, N107 (2012)
3. R. Xu, Q. Tao, Y. Yang, and C. Takoudis, "Atomic Layer Deposition and Characterization of Stoichiometric Erbium Oxide Thin Dielectrics on Si(100) using $(CpMe)_3Er$ Precursor and Ozone", Appl. Surf. Sci., 258, 8514 (2012)
4. R. Xu and C. Takoudis, "Chemical Passivation of GaSb-based Surfaces by Atomic Layer Deposited ZnS Using Diethylzinc and Hydrogen Sulfide", J. Vac. Sci. Technol. A, 30, 01A145 (2012)
5. R. Xu, J. Huang, S. Ghosh, and C. Takoudis, "Deposition and Characterization of Atomic Layer Deposited ZnS Thin Films on p-type GaSb(100) Using Diethylzinc Precursor and Hydrogen Sulfide", ECS Transactions, 41,229 (2011)
6. K. Banerjee, J. Wang, S. Ghosh, R. Xu, et.al, "Surface Study of Thioacetamide and Zinc Sulfide Passivated Long Wavelength Infrared Type-II Strained Layer Superlattice", Proc. SPIE, 8012, 801243 (2011)

TO BE SUBMITTED

1. "Nucleation Behavior-Morphology-Resistivity of Atomic Layer Deposited Pt on Atomic Layer Deposited Yttria-Stabilized Zirconia Films"

PRESENTATIONS

1. "Growth Characteristics and Properties of Yttrium Oxide Thin Films by ALD from Novel $Y(iPrCp)_3$ Precursor and O_3", Electrochemical Society (ECS) 222 th Meeting, Energy Session, Honolulu, HI, 2012

2. “Deposition and Characterization of Atomic Layer Deposited ZnS Thin Films on p-type GaSb(100) Using Diethylzinc Precursor and Hydrogen Sulfide”, Electrochemical Society (ECS) 220 th Meeting, Emerging Applications Session, Boston, MA, 2011
3. “Atomic Layer Deposition and Characterization of ErxTi1-xOy Films”, American Institute of Chemical Engineers (AICHE) 2011 Annual Meeting, Minneapolis, MN
4. “Atomic Layer Deposition and Characterization of Erbium Oxide Thin Films On Si(100) Using $(CpMe)_3Er$ Precursor and Ozone”, American Institute of Chemical Engineers (AICHE) 2010 Annual Meeting, Salt Lake City, UT
5. “Structural Characterizations of Atomic Layer Deposited HfO_2, TiO_2 and $Hf_xTi_{1-x}O_2$ Using Tetrakis(diethylamino) precursors and H_2O”, American Institute of Chemical Engineers (AICHE) 2010 Annual Meeting, Salt Lake City, UT

HONORS AND AWARDS

1. ECS 220th Meeting fellowship for the ALD Symposium sponsored by Air Liquide Group, Boston (2011)
2. GSC Travel Awards, University of Illinois at Chicago (2010, 2011)
3. Graduate Student Presenter Award, University of Illinois at Chicago (2010, 2011)
4. Honored by IL Math and Science Academy for mentoring IMSA high school students (2009, 2010)